UNIVERSITÀ
DEGLI STUDI
FIRENZE

DOTTORATO DI RICERCA IN FISICA E ASTRONOMIA

CICLO XXXIV

COORDINATORE Prof. Raffaello D'Alessandro

Imaging of subwavelength light localization in all-dielectric complex nanostructures

Settore Scientifico Disciplinare FIS/03

Dottorando
Dott. Nicoletta Granchi
Nicoletta Granchi
(firma)

Tutore
Prof. Francesca Intonti
Francesca Intonti
(firma)

Coordinatore
Prof. Raffaello D'Alessandro
Raffaello D'Alessandro
(firma)

Anni 2018/2021

Index

Introduction

Photonic devices have become ubiquitous in everyday life, but often go unnoticed. Light sources such as LEDs, Quantum Dots LEDs, and laser diodes have found their way into countless applications where light is created, and are an essential part of widespread optical communication technologies, at the core of the wideband internet. We are at the beginning of a "photonics revolution". In the effort to further progress the high density transistor integration and thus the modern electronic system performances, scientists have by now turned to photons instead of electrons, as information carriers in communication. Photonics represents a growing opportunity for designing and manufacturing devices, systems and integrated circuits for applications in high-speed data communications, advanced sensing, and imaging. However, in spite of the numerous advantages of photons, all optical integrated circuits have yet to be commercially available on large scale due to the difficulties in designing efficient optical components building blocks. Photonic crystals have been one of the main player for a long time in this novel field of physics, because of the versatility and ability to control the propagation of light at the nanoscale that they offer. Since their introduction, a great deal of groundbreaking phenomena concerning light-matter interaction at optical frequencies have been theoretically predicted and experimentally verified. They led to large technological developments, especially innovative optoelectronic and photovoltaic applications. For instance, light manipulation at the nanoscale is achievable through photonic crystals which exhibit finite energy band-gap for light propagation. In particular, two-dimensional photonic crystal cavities fabricated on semiconductor slab are the state of the art devices to strongly localize electromagnetic fields in volumes below a cubic optical wavelength of light, acting as efficient nano-resonators with high Q factors (10^6). However, one important limitation of photonic crystal cavity modes is their low spatial footprint and number density. This led to the developement of the so-called *photonic crystal molecules*, coupling two or more cavities, and *micro-opto electromechanical systems*, exploiting the double-slab technology to increase the number of modes and engineer them. On the other hand, random dielectrics have attracted a lot of interest in the past decades for the fascinating, complex and elusive physics of disordered media, but also for a wealth of interesting applications ranging from sensors to quantum electrodynamics effects. An advantage for optoelectronics and quantum source integration offered by random systems is their high density of photonic modes, which span a large range of spectral resonances and spatial distributions, thus increasing the probability to match randomly distributed emitters. Conversely, the main disadvantage is the lack of deterministic engineering of one or more of the many random photonic modes achieved, the low Q factor

(≈200), and the weak mode steadiness to local perturbation and disorder.

Inspired by photonic structures in nature, and enabled by advances in nanofabrication processes, recent investigations have unveiled how the design of structural correlations down to the subwavelength scale could be exploited to control the scattering, transport and localization of light in matter.

Complex and disordered media is a timely and hot topic in science, let's just mention the fresh Nobel award for Physics this year. Within this scenario, correlated disordered photonics is a fascinating research class of media, which recently received a major boost with an emerging class of optical systems, at the interface between geometry, topology and physics, featuring anomalous suppression of density fluctuations on large scales, that are Hyperuniform Disordered (HuD) materials. The underlying hidden order renders them appealing for several applications. In particular, it has been widely demonstrated that HuD materials can display large, complete photonic band gaps. One of the principal aims of this thesis is to study the first optically active HuD photonic device emitting in the optical range through *Near-field scanning microscopy*, and explore how light localizes at the nanoscale with this advanced technique.

The introduction of hyperuniformity in photonics, led to achieve an alternative comprehension of the photonic band gap concept, revealing that there is a strong correlation between the scattering properties of the individual scatterers and the band gap location of the whole structures. It is worth noticing that, in this context, individual scatterers are none other than dielectric Mie resonators. Therefore, within the framework of a study on light localization in a complex dielectric structure like HuD systems, also a deep understanding of Mie scattering by nanoparticles is a relevant task to be achieved.

To Mie resonators is dedicated another important branch of photonics, whose aim is to exploit all-dielectric nanoscatterers as an alternative located in between photonic crystals and plasmonic nanoparticles, to manipulate and control light. In high-index resonators infact, optical resonances originate from the displacement currents due to the oscillations of bounded electrons; they are therefore not affected by Ohmic damping or heating effects like plasmonic nanoparticles. Compared with their metallic counterparts, Mie resonators feature the unique capability to exhibit both electric and magnetic modes that completely redistribute scattering and emission patterns. Higher order multipolar Mie resonances in particular, seem to be extremely promising for optoelectronics applications; however, the optical studies reported in literature, both in the near-field and the far-field, have been mainly limited on the lower energy terms and do not provide information on more than one optical mode at a time. In this work, we overcome this limitation by presenting a complete *Near-field* and *Dark-field hyperspectral imaging* study of single Mie resonators obtained through solid state dewetting.

The thesis is structured as follows: in Chapter 1 we report the basic principles of *nano-* and *micro-*scale optics; starting from the limit imposed by light diffraction, we provide a description of how it is possible to overcome this limitation by detecting the optical near-field, and treat the transition between the two optical regimes that are at the basis of the techniques employed in this work.

We then move to the theoretical introduction of the two main topics of the thesis: dielectric Mie resonators and Hyperuniform Disordered Photonics. In Chapter 2 we introduce the concept of Mie scattering from nanoparticles, highlighting how these devices can be considered as a fascinating and reliable method to manipulate light at the micro- and nano-scales. Afterwards, we focus on directional scattering properties of Mie resonators and we discuss their interaction with the substrate, in order to explain how sub-wavelength optical resonators can be efficient building blocks of functional materials. We conclude the chapter with an overview on the state of the art of experimental demonstrations in the optical range, both in the far-field and in the near-field, and with a general description of the main fabrication techniques of high-index nanoresonators.

In Chapter 3 it is explained the broad concept of hyperuniformity, and how it is located within the framework of density fluctuations in many particle systems. Thereafter, we describe how HuD systems have recently attracted great attention in photonics. In particular, by sharing features of both periodic and random systems, HuD photonic structures constitute the archetypal of a system in which by controlling the long-range correlations, light transport can be tailored from diffusive transport to an intermediate regime dominated by light localization, due to the presence of a photonic band gap comparable in width to band gaps found in photonic crystals.

In Chapter 4 we explore the methods that have been used to obtained the results of this thesis: we describe the functioning of the Scanning Near-field Optical Microscope (SNOM) and how we implemented Dark-field spectroscopy on the SNOM microscope. Next to the experimental methods, numerical simulations have been fundamental in the comprehension and validation of the results here presented; we therefore describe the basic principles of computational electromagnetics, with a special attention to Finite Difference Time Domain (FDTD) and Finite Element Method (FEM) simulations.

The last two Chapters contain the main results and achievements; in Chapter 5 we address a full optical characterization of dielectric Mie resonators realized through solid state dewetting, both in the near-field and in the far-field. Specifically, we are able to obtain a spatial and spectral mapping of the multi-polar modes of a dielectric island by hyperspectral imaging, obtaining a reasonable agreement between experiment and simulations. We show how the simultaneous detection of several resonant modes allows to clarify the role of substrate and incidence angle of the impinging light, highlighting spectral splitting of the quadrupolar mode and resulting in different spatial features of the field intensity. Then, we focus on how the implementation of Dark-field scanning microscopy, by exploiting the scanning stages of the SNOM setup, can bring interesting detection features. We describe how it allows a complete characterization of the beam steering properties of nanoscatterers by means of a novel way of managing the dark-field technique, achieving hyper spectral imaging through Dark-field scanning microscopy.

In Chapter 6 we described the results obtained on the HuD photonic double membrane structure, where we take advantage of the combination of the HuD special design in slab photonics, the use of embedded quantum dots for feeding the HuD resonances and Near-field hyper spectral imaging with sub-wavelength resolution in the optical range to explore the transition from localization to diffusive transport. We report, both theoretically and experimentally, how photonic HuD systems actually support a variety of resonances ranging from strongly localized modes to extended modes, typical of transport in multiple scattering regime. We then focus on Anderson-like modes that arise at the photonic band gap edges; these modes display very high Q/V, and turn out to be intrinsically reproducible and resilient to fabrication-induced disorder, thereby paving the way for a novel photonic platform for quantum applications. We conclude the Chapter by presenting a near-field imaging of high-Q optical cavities in slab architectures in HuD enviroment.

The last Chapter, where we give the conclusions of the work, is also thought as a way of describing what might come next and how our achievements on subwavelength light localization in all-dielectric complex nanostructures might pave new exciting routes in the field of photonic applications.

Chapter 1

Optics at the nanoscale and microscale

The study of light-matter interaction has demanded, in the last decades, a rapid developement of more and more complex spectroscopy techniques. At the basis of the image formation in microscopy is the interaction of light with the studied object; this interaction results in the generation of both near-field and far-field light components. The far-field light propagates through space in an unconfined manner following the principles of geometric optics. The near-field (or evanescent) light consists in a non-propagating field that exists near the surface of an object at distances of the order of the light wavelength. Until the second half of last century the spatial resolution achievable by every optical microscope, even without any imperfections, was hampered to the diffraction limit. Only the development of new kinds of optical microscopes exploiting the near-field component of light allowed for investigating object and light emitters down to a sub-wavelength scale. Here, we report the basic principles of *nano*- and *micro*-scale optics. Starting from the limit imposed by light diffraction, we provide a description of how it is possible to overcome this limitation by detecting the optical near-field, and treat the transition between the two optical regimes that are at the basis of the techniques employed in this work.

1.1 The diffraction limit

With the advent and developement of the scientific method, both optics fundamental laws and technical achievements quickly enlarged the understanding of natural phenomena, together with the instrument assisted eye perception. To Galileo Galilei is likely attributed the first prototype of an optical microscope (1610). However, only in 1671 it was possible to observe red blood cells and bacteria with a few µm size resolution, thanks to the work of van Leeuwenhoek [1]. Then, it was Abbe at the end of the nineteenth century that clarified that also an ideal microscope without any imperfections in the lenses or misalignments would not be able to overcome the physical resolution *limit* imposed by diffraction [2]. In particular, according

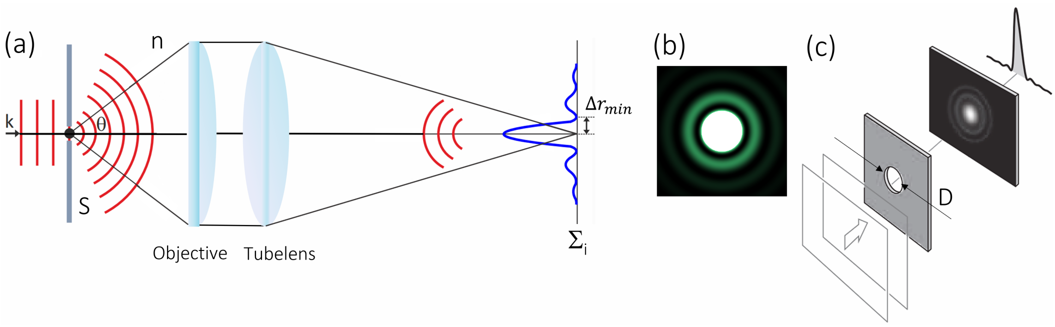

Figure 1.1. **(a)**Schematics concerning the image formation in a conventional microscope system (objective + tubelens) on the plane Σi of a point-like object (S) illuminated by a monochromatic plane wave with wavevector k; θ is the half-angle of the maximum light cone accepted by the objective. Red curves describe the behaviour of radiation field wavefront. The blue curve represents a onedimensional profile cut of the Airy disk in Σi. **(b)** Spatial modulation of the light intensity in the Airy diffraction pattern. **(c)** Sketch of the process of generation of the Airy diffraction pattern by circular aperture on a parallel plane (adapted from [5]).

to Abbe, the minimum radial resolution $\mathbf{\Delta r}$ obtainable in the image plane by an optical system (a sketch is reported in Fig.1.1a) is defined as:

$$[\Delta r]_{min} \approx 0.61 \frac{\lambda}{NA} \tag{1.1}$$

where NA is the numerical aperture of the optical system, that is related to the half angle θ of the maximum light cone accepted by the lens or objective according to the relation $NA = nsin\theta$, with n the refractive index of the medium between the source and the microscope. In the specific case of an optical microscope the resolution can be evaluated through Eq.1.1, and it is defined, following Rayleigh criterion [3, 4], as the shortest distance between two distinguishable points on a specimen that can still be observed as separate objects.

It is possible to understand the basic imaging process by considering the image formation of a point-like source (whose dimensions are $D \ll \lambda$) like the one represented in Fig.1.1a. The incoming light is diffracted by the point-like specimen (S), as always happens when light encounters an obstacle. Then, considering a conventional microscope system, light is collected by the objective and tubelens. The finite object image appears in the conjugate plane Σ_i. Since NA cannot be large enough to collect all the diffracted light ($\theta < \pi/2$), Abbe demonstrated that the image recorded in Σ_i does not exactly correspond to the original object, and it is blurred with a typical intensity pattern, shown in Fig. 1.1b; this pattern is called *Airy disk*[5]. In generic terms, the Airy disk is defined as the diffraction pattern created when illuminating a circular pupil of diameter D, as represented in Fig.1.1c. It consists of a central disk of angular radius $1.22\lambda/D$, surrounded by many alternatively but very faint dark and bright rings. Therefore, in any finite optical system that detects electromagnetic (e.m.) radiation, the image of a point-like light source is not a delta-like function, but it is broadened as an Airy disk, which thus represent the point spread function.

Clearly, any finite specimen can be considered as a collection of point-like sources, whose size is smaller than λ, and therefore the use of standard microscopy to perform imaging of small objects inevitably determines loss of information. Although modern oil or solid immersion objectives can nowadays be fabricated with NA as large as 2.0 in the visible spectral range [6], optical images resolved with a subwavelength resolution ($\Delta r \ll \lambda$) are not allowed by Eq.1.1. For instance, in the telecom window near-infrared spectral range the largest transparent NA is about 1.4, and allows to obtain a spatial resolution of $\Delta r \approx 700nm$.

1.2 Near-field and Far-field theory

Almost a century later the derivation of Maxwell equations (1861), a peculiar optical phenomenon that has put fundamental limits to any image reconstruction was discovered, that is the existence of e.m. evanescent waves in any diffraction process [7]. Evanescent waves are exact solutions of Maxwell waves-equations that do not propagate, but exhibit an exponential decay of the amplitude. Classical wave optics based on Huygens-Fresnel principle [5] has a fundamental deficiency, since it overlooks the role of evanescent waves in diffraction. In fact, the classical solution of diffraction problems are accurate in the radiation zone, but fails to reproduce what happens in close proximity of the light source. In order to analyze the reason why by collecting only propagating radiation with any kind of microscope the image is always blurred, we exploit the angular spectrum decomposition, that is a mathematical noteworthy technique to describe optical fields in homogeneous media. The Fourier based characterization that emerges, allows to estimate the series expansion of an arbitrary field in terms of propagating and evanescent waves with variable amplitudes and directions. Within the angular spectrum representation, the description of the e.m. field radiated by a light source or scattered by an object in an arbitrary $z = const.$ plane is [8]:

$$A(r,t) = \int\int_{-\infty}^{\infty} \hat{\boldsymbol{A}}(k_x,k_y,0) exp(ik_z z + ik_x x + ik_y y - i\omega t) dk_x dk_y \tag{1.2}$$

where $\boldsymbol{A(r)}$ represents either the electric ($\boldsymbol{E}$) or the magnetic ($\boldsymbol{H}$) field and $\hat{\boldsymbol{A}}(k)$ its Fourier transform, while $\omega = 2\pi nc\lambda^{-1}$. Since the wavenumber is $k = 2\pi n\lambda^{-1} = \sqrt{k_x^2 + k_y^2 + k_z^2}$, the e.m. fields described by Eq.1.2 can be classified in two cathegories, according to their different behaviours in two complementary regimes, respectively characterized by a *real* or *imaginary* wavenumber component k_z.

$$k_x^2 + k_y^2 \leq (2\pi n/\lambda)^2 \Rightarrow k_z \in \mathbb{R} \tag{1.3}$$

$$k_x^2 + k_y^2 > (2\pi n/\lambda)^2 \Rightarrow k_z \in \mathbb{C} \tag{1.4}$$

Hence, for a purely dielectric medium with no losses turns out that the factor e^{ik_z} is either an oscillatory (Eq.1.3) or an exponentially decaying (Eq.1.4) function. Therefore, the angular spectrum is a superposition of both plane waves and evanescent waves. Remarkably, it is possible to reconstruct without distortions the field coming from the specimen by exploiting Eq.1.2, only if all the spatial frequencies k_x, k_y are collected. On the other hand, if the imaging system is sufficiently separated from the object, the contribution of the evanescent waves is zero and only the low spatial frequencies, which satisfy Eq.1.3, have to be considered. In other words, the image collected is a low pass filtered representation of the original field. By filtering out the high in-plane spatial frequencies described by Eq.1.4, we loose information about the object smallest details. In principle, if it is performed an experiment in which also the evanescent waves are detected, an infinite bandwidth of spatial frequencies can be achieved. However, this kind of measurement requires the e.m. fields probing in close proximity of the sample, where evanescent are not yet totally suppressed. Therefore, it is clear that the two spatial regimes, which show very different light behaviours, can be distinguish for any imaging purpose:

- Near-field $r \ll \lambda$
- Far-field $r \gg \lambda$

where r is the distance between the specimen and the probe that collect the e.m. fields. The intermediate-field ($r \sim \lambda$) region is the vaguely defined boundary between the two regions in which both near-field and far-field effects are important.
We now describe the two spatial regime in a qualitative way [5]; let's consider an opaque screen Σ (like the one sketched in Fig.1.2a), containing a single small aperture of dimension b, which is being illuminated by plane waves from a very distant point source, S. The plane of observation σ is a screen parallel far from Σ. Under this condition the projected pattern is considerably spread out bearing little or no resemblance to the actual aperture. Thereafter, moving σ farther from Σ essentially changes only the size of the pattern and not its shape. This phenomenon is known as **Fraunhofer** or far-field diffraction. Differently, if the screen σ is approached closer to Σ, the image of the aperture start to become easily recognizable, despite the still prominent fringes. For smaller distances, the image become more and more structured, until an image of the aperture is projected onto the screen, clearly recognizable despite some slight fringing around its periphery (Fig.1.2b). This phenomenon is known as **Fresnel** or near-field diffraction. A succession of diffraction patterns at decreasing distance form a single slit is shown in Fig.1.2b, representing the transition from the far-field regime to the near-field regime. Interestingly, if in the Fraunhofer regime we could sufficiently reduce the wavelength of the incoming radiation, the pattern would revert to the Fresnel case. If λ were decreased even more, so that it approached zero, the fringes would disappear, and the image would take on the limiting shape. As a practical rule-of-thumb, Fraunhofer diffraction will occur at an aperture (or obstacle) of greatest width b when $R > b^2/\lambda$, where R is the smaller of the two distances from S (source position) to Σ and Σ to σ (Fig. 1.2a).
The two optical regimes can be also highlighted with a quantitative approach by studying the emission of a dipole, that is the smallest radiating e.m. unit source, which represents the first approximation of any antenna emission [7]. In the far-field the magnetic and the electric fields are respectively:

$$\boldsymbol{B} = k^2(\boldsymbol{n} \times \boldsymbol{p})\frac{e^{ikr}}{r} \tag{1.5}$$

$$\boldsymbol{E} = \boldsymbol{B} \times \boldsymbol{n} \tag{1.6}$$

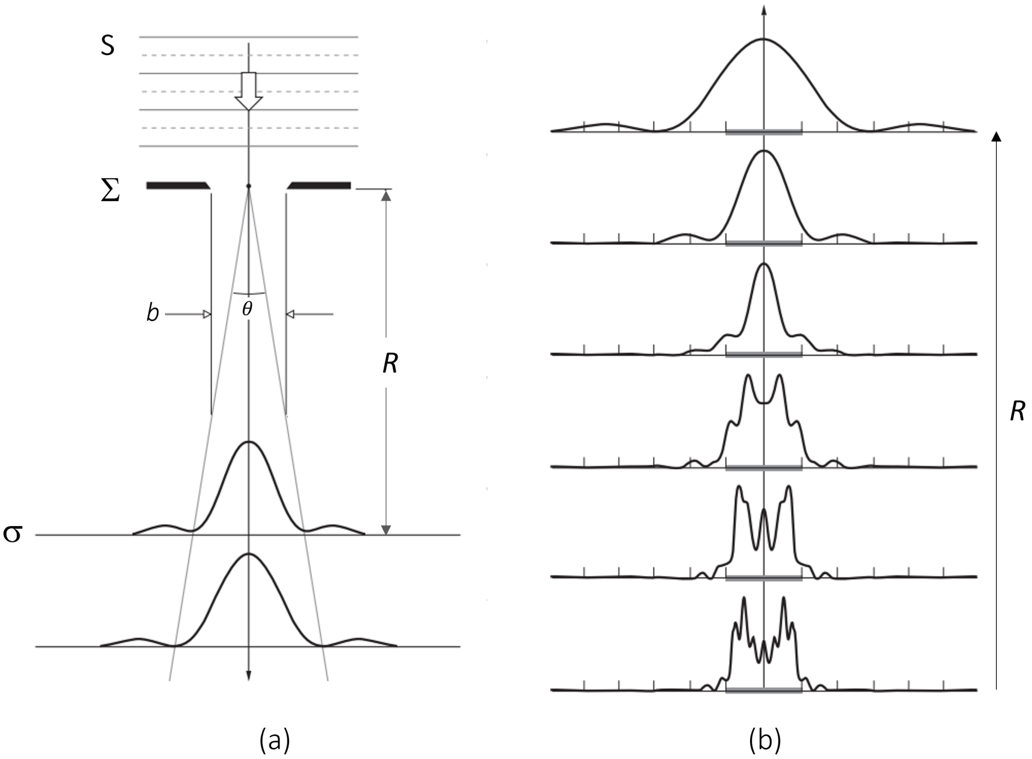

Figure 1.2. **(a)**Diffraction pattern formed in the far-field regime after illuminating with a plane wave a slit of dimension b. Σ and σ are the slit plane and the detection plane, respectively. **(b)** Succession of diffraction patterns at increasing distance form a single slit R (from bottom to top); Fresnel at the bottom (nearby), going toward Fraunhofer at the top (faraway). The gray band corresponds to the width of the slit. Adapted from [5].

where $\boldsymbol{n} = \boldsymbol{r}/r$ is the unit vector of real space and the electric dipole moment is represented by $\boldsymbol{p} = \int \boldsymbol{r}\rho(\boldsymbol{r})d^3r$ with $\rho(\boldsymbol{r})$ representing the charges density. In the far-field region we find propagating spherical waves where both field radiation intensities decrease as the square of distance. As in every propagating light wave, both fields described in Eq.1.5 and Eq.1.6 are strongly connected since each of them is generated by a change of the other. In the near-field ($kr \ll 1$) they become:

$$\boldsymbol{B} = ik(\boldsymbol{n} \times \boldsymbol{p})\frac{1}{r^2} \tag{1.7}$$

$$\boldsymbol{E} = [3(\boldsymbol{n} \cdot \boldsymbol{p}) - \boldsymbol{p}]\frac{1}{r^3} \tag{1.8}$$

Differently from the far-field regime, in the near-field region the electric and magnetic fields can exist independently of each other, and singularly dominate. Moreover, the near-field components depend on the detailed properties of the source, since for instance Eq.1.8 coincides with the electrostatic dipole, and they decay very rapidly as a function of the distance. Consequently, near-field components carry the information needed to determine the spatial distribution of the finite size emitter. Therefore, it is straightforward that every time light is emitted or finds an obstacle and scatters from a sample, there is a loss of information on propagating from the near-field to far-field. Because the near-field light decays exponentially within a distance less than the wavelength of the light, it usually goes undetected. It follows that for traditional optical systems fails the possibility of distinguishing sub-micrometric details of nanostructures (like Photonic Crystal Cavities [9] or photonic disordered systems [10]), that are at the center of research fields like photonics and nano-optics. A technology that allows to overcome this problem and to go beyond the diffraction limit is the Scanning Near Field Optical Microscopy (SNOM), that will be described in Chapter 4. On the other hand, in many practical photonic applications (regarding for example Mie scattering [11, 12] and nano-antennas [13]), one is interested mainly in effects where the distance from the antenna to the observer is very much greater than the largest dimension of the transmitting antenna. Under these conditions, the equations describing the created fields can be simplified, dropping all terms that provide only minor contributions to the final field [7]. These simplified distributions belong to the far-field regime, and usually carry the property that the angular distribution of energy does not change with distance. Such an angular energy distribution is usually termed as an angular pattern. The most indicated and employed optical technique for this cathegory of photonic applications is the Dark-Field Microscopy, that will be treated in Chapter 4.

Chapter 2

Magnetic Light: all-dielectric Mie scattering

Efficient control of visible light at the nanoscale is one of the topics that are at the center of photonics' principal aims; owing to their low dissipative losses, high-permittivity all-dielectric nanoparticles, known as Mie resonators, are emerging as a promising alternative to metallic nanoparticles for a wide range of nanophotonic applications. In the beginnning of this chapter, a brief explanation outlines the main reasons rendering these devices a fascinating and reliable method to manipulate light at the micro- and nano-scales. Then, after a general overview on the different light scattering regimes, we focus on the Mie theory of scattering to explain the physical origin of the so-called *magnetic light*, describing the electromagnetic resonant modes inside all-dielectric nanoparticles. Afterwards, we focus on directional scattering properties of Mie resonators and we discuss their interaction with the substrate, in order to explain how sub-wavelength optical resonators can be efficient building blocks of functional materials. Then, it is reported an overview on the state of the art of experimental demonstrations in the optical range, both in the far-field and in the near-field. Finally, the last section is a general description of the main fabrication techniques of high-index nanoresonators, with special attention to be given to solid-state dewetting, that can be used to fabricate a large plethora of dielectric structures, from single nanoparticles to more complex scenarios like spinodal patterns.

Located in-between photonic crystal cavities and plasmonic nanoparticles, Mie resonators offer an alternative way to enhance light-matter interaction at the nanoscale [14]. While photonic crystals exhibit resonances with high quality factors but relatively small modal volumes ($\sim 1\ \mu\mathrm{m}^3$)[15], plasmonic metal nanoparticles, mainly characterized by smaller quality factors and extremely tiny modal volumes [16], show very great losses in the visible frequency range. Infact, the extraordinary enhancement of an electric field by plasmonic nanoparticles relies on the free electron response; when the frequency of incident light matches that of the free electrons' oscillations inside a sphere, the plasmonic resonance manifests itself, and a strong electric field is produced in the vicinity of the particle. These oscillations however, are accompanied by significant optical loss, arising from both intraband and inter-band transitions, and eventually heat the particle [17]. This is a critical factor that strongly affect their overall performances and limits their scalability. In contrast, optical resonances of high-index nanoparticles (such as Silicon, Germanium or Tellurium [12]) originate from the *displacement currents* due to oscillations of bounded electrons; these currents are free of Ohmic damping, which allows to reduce the nonradiative losses and heating of the optical nanoresonator. Compared with their metallic counterparts, dielectric Mie Resonators whose refractive index is > 2.5 therefore feature the unique capability to exhibit both electric and magnetic modes that completely redistribute scattering and emission patterns. Infact, they support resonances with frequency below or near the bandgap of the constituent material. The distribution of the electromagnetic field of such resonances makes these particles behave like a magnetic dipole (first Mie resonance) and an electric dipole (second Mie resonance)[11]. Besides displaying weak losses in the optical and near-infrared range of frequencies, their scattering properties, resulting from the interference between magnetic and electric modes, can be tuned by modifying the particle shape and refractive index [7]. For all these reasons, and for their compatibility with Si-based nano-fabrication technologies [18], high-index dielectric structures can be used as building blocks with unique optical functionalities for real metadevices and novel structures.

2.1 Mie scattering of dielectric sub-wavelength particles

Ever since Lord Rayleigh clarified why our sky is blue [7], the study of light scattering by nanoparticles has been an important part of optical science. Later, Gustav Mie explained a variation in colours of colloidal solution of gold nanoparticles in terms of their size distribution, thereby opening up the possibility of using resonant nanoscale scatterers to control an optical response. The diffusion of light, also known as scattering, is a phenomenon which consists in the re-emission in many directions (usually non-random) of a beam of light that strikes a set of dispersed particles of variable size present in a system that can be in a solid, liquid or gaseous state. Depending on the size of the dispersed particles and depending on the wavelength of the incident radiation, the angular distribution of the diffused light is different; the intensity of the diffused light is therefore dependent on the diffusion angle. There are different ways of light scattering, but the most important are the *Rayleigh* scattering and the *Mie* scattering (Fig. 2.1). Rayleigh scattering is the elastic scattering of a light wave caused by particles that have small dimensions compared to the wavelength of the wave itself, which occurs when light passes through a turbid medium, especially gases and liquids, but also solids with impurities or inclusions. Since the diffusion is elastic, the scattered radiation has the same frequency (and wavelength) as the incident one. The equations that describe the diffusion are very complex and, especially when this phenomenon is repeated many times, impossible to solve exactly in the general case. A widely used approximate solution is the so-called Rayleigh solution [19] and it explains why the light dispersion is isotropic

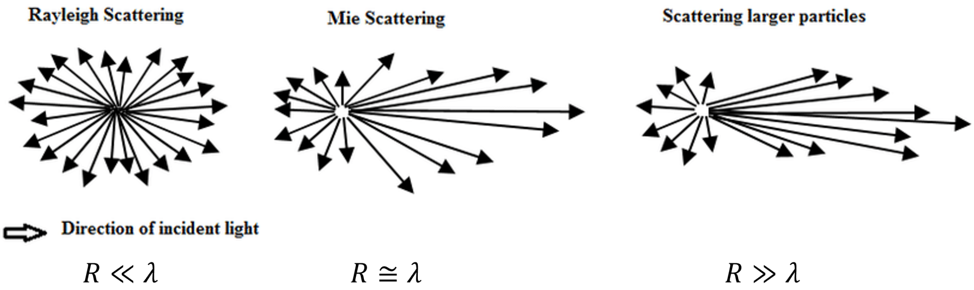

Figure 2.1. Angular distribution of the scattered light for the different types of scattering, respectively Rayleigh, Mie and from larger particles.

(as it can be observed in the left sketch of Fig. 2.1). Infact, the strong dependence of the Rayleigh scattering coefficient from $1/\lambda^4$ is the reason for which radiations with small wavelengths are more effectively diffused. Mie scattering, also known as Lorenz-Mie scattering, is a complete and mathematically rigorous solution to the problem of scattering of an electromagnetic wave on a sphere or cylinder. It is valid theory for scattering centers of all sizes and, in the limit in which these are much smaller than the incident wavelength, the Rayleigh Scattering (which is valid only for point-like scatterer) is obtained.

In order to illustrate the fundamental properties of Mie scattering by nanoparticles, let us consider the case of a spherical particle illuminated by a plane wave, for which there exists an exact analytical solution of Maxwell's equations. A sphere can infact be arguably perceived as an archetype of a scatterer for the extraction of valuable insights regarding the scattering problem by bounded objects, and it is commonly used as a reference for any kind of electromagnetic scattering theory and applications [20]. Mie demonstrated that both metallic and dielectric spherical particles can possess strong scattering resonances [11]. Let's consider a non-absorbing dielectric sphere of radius R and relative index of n under plane wave illumination, and assume linearly polarized light. The field scattered by the sphere can be decomposed into a multipole series, the so-called Mie's expansion of *normal modes*, characterized by the electric and magnetic Mie coefficients a_m and b_m, respectively:

$$a_m = \frac{n\psi_m(nx)\psi'_m(x) - \psi_m(x)\psi'_m(nx)}{n\psi_m(nx)\xi'_m(x) - \xi_m(x)\psi'_m(nx)} \tag{2.1}$$

$$b_m = \frac{\psi_m(nx)\psi'_m(x) - n\psi_m(x)\psi'_m(nx)}{\psi_m(nx)\xi'_m(x) - n\xi_m(x)\psi'_m(nx)} \tag{2.2}$$

where $x = kR$ and k is the free-space wavenumber, and $\psi_m(x)$ and $\xi_m(x)$ are the Riccati-Bessel functions. The primes indicate the derivation with respect to the arguments. In these equations, m is the index of the multipolar terms, like electric or magnetic dipoles etc. Diagrams from Mie's 1908 paper [11], which show the electric field lines corresponding to the transverse components of the first four normal modes ($m = 1...4$) [21], are given in Fig.2.2. Therefore a_1 and b_1 result proportional to the contribution of the electric and magnetic dipoles, a_2 and b_2

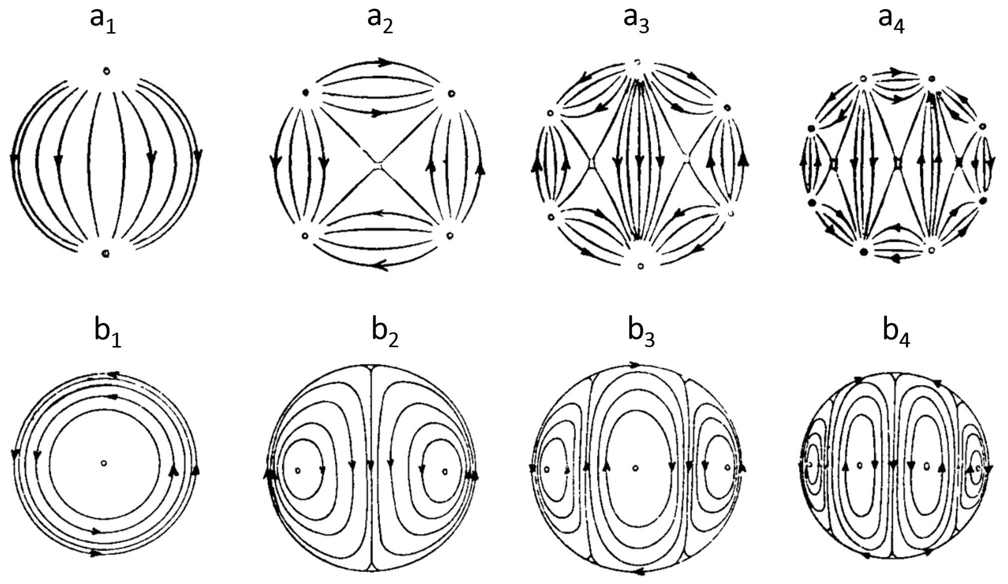

Figure 2.2. Electric field patterns of electric (a_m) and magnetic (b_m) contribution ($m = 1...4$): normal modes (Mie, 1908 [11]).

to the quadrupoles, and so on. In order to define the extinction and absorption cross section [21], we shall find useful to write the Mie coefficients in terms of the scattering phase-shifts α_m and β_m [22]:

$$a_m = \frac{1}{2}(1 - e^{-2i\alpha_m}) = i \sin \alpha_m e^{-i\alpha_m} \tag{2.3}$$

$$b_m = \frac{1}{2}(1 - e^{-2i\beta_m}) = i \sin \beta_m e^{-i\beta_m} \tag{2.4}$$

In absence of absorption, i.e. for real n, the phase angles α_m and β_m are real, then the extinction and scattering cross sections, σ_{ext} and σ_S respectively have the same form:

$$\sigma_S = \sigma_{ext} = \frac{2\pi}{k^2} \sum_{m=1}^{\infty} (2m+1)[\sin^2 \alpha_m + \sin^2 \beta_m] = \sum_{m=1}^{\infty} [\sigma_{E,m} + \sigma_{M,m}] \tag{2.5}$$

where he have differentiate the electric $\sigma_{E,m}$ and magnetic $\sigma_{M,m}$ contribution to the total scattering cross section σ_S. From Eq.2.5 it is possible to demonstrate that lossless and non-magnetic materials have scattering properties that depend on two parameters [23]: the dielectric permittivity ϵ and the size parameter q, which is proportional to the ratio between the nanoparticle radius R and the wavelength of incident light λ, since $q = 2\pi R/\lambda$. It is possible to distinguish metallic from dielectric nanoparticles, at a fixed q, in terms of the sign of ϵ, which is negative for metals and positive for dielectrics. In Fig.2.3(a) [23] it is reported the scattering efficiency (dimensionless ratio of scattering cross section σ_S to geometrical cross section of the particle) versus dielectric permittivity ϵ (lossless particle, $q = 0.5$) for metallic

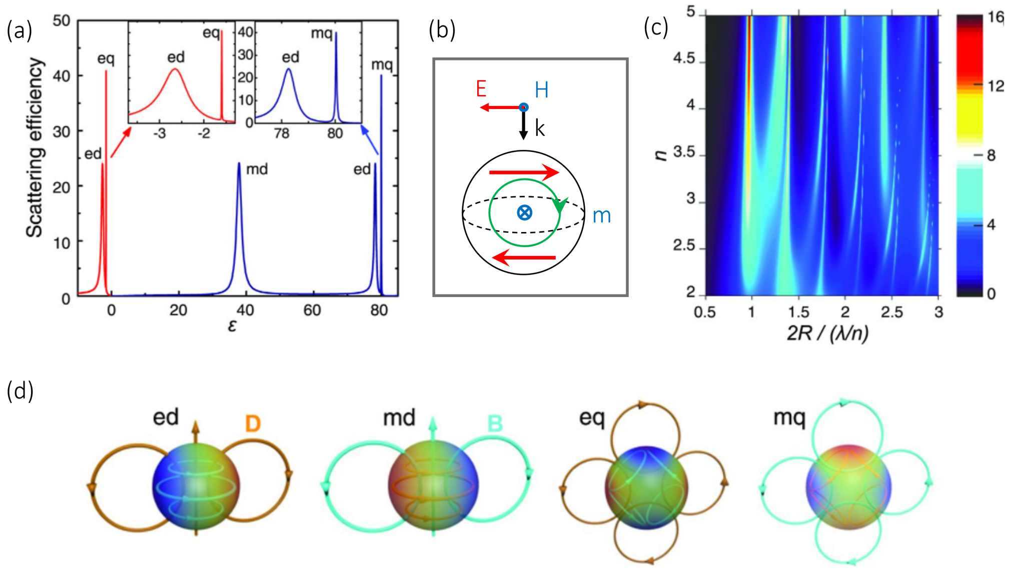

Figure 2.3. **(a)**Scattering efficiency (dimensionless ratio of scattering cross section to geometrical cross section of the particle) versus dielectric permittivity ϵ (lossless particle, $q = 0.5$) for plasmonic ($\epsilon < 0$, red line) and dielectric ($\epsilon > 0$, blue line) materials. Abbreviations for resonances: ed, electric dipole; eq, electric quadrupole; md, magnetic dipole; eq, electric quadrupole. **(b)** Sketch of the driving excitation mechanism of the md mode on a spherical dielectric particle. **(c)** Scattering efficiency of a lossless dielectric particle (color scale at right) as a function of refractive index n and size parameter $q = 2\pi R/\lambda$. **(d)** Illustration of the electric and magnetic field structures for different electric and magnetic resonances supported by a spherical dielectric particle. Figures reprinted from [23].

($\epsilon < 0$) and dielectric ($\epsilon > 0$) materials. From the graph it is possible to see that small metallic spheres ($\epsilon < 0$, $q > 1$) produce only localized surface plasmon resonances of an electric type-dipole, quadrupole, etc., while their magnetic response remains almost negligible because of a vanishing field inside the sphere. Therefore, in order to generate a magnetic response from metallic structures, the particle's geometry should be changed. Differently, for dielectric particles we can observe both electric and magnetic-type responses of comparable strengths. Moreover, in the small particle limit and large particle permittivity ($n \gg 1$), the scattering cross section σ_S presents characteristic sharp resonance peaks, and the values of the size parameter q define the resonance spectral positions. The ability to excite dipolar magnetic resonances in dielectric particles, as well as the driving mechanism, has been described recently [24]. The in-plane magnetic dipole is driven by the incoming electric field of light that couples to displacement current loops, vertically oriented in the particle (Fig.2.3b). The displacement current loop (green) induces a magnetic dipole moment (blue), oriented perpendicular to the incident electric field polarization (red). If a significant retardation of the driving field throughout the particle is satisfied, then the electric field undergoes a significant phase shift capable of matching the opposing electric field orientation in the top and bottom part of the particle. This configuration is required to obtain efficient driving of the displacement current loop, and formally, it occurs when the wavelength inside the particle becomes comparable to the particle's diameter $2R \approx \lambda/n$, as confirmed by Fig.2.3(c), where the scattering efficiency of a lossless dielectric particle is reported as a function of refractive index n and size parameter. The field structure of the four major resonant modes in high-index dielectric particles, i.e. magnetic dipole, electric dipole, magnetic quadrupole and electric quadrupole is shown in Fig.2.3(d). Following Mie theory, the maximum achievable scattering efficiency for a specific multipolar excitation of a subwavelength particle depends only on the resonance frequency, whether if it is a dielectric or metallic material. Therefore it is possible that many plasmonic effects observed for the scattering of light by metallic nanoparticles can be also realized with high-index dielectric nanoparticles. The direction to be followed can be found in the interpretation of Fig.2.3(c), where the scaling of different resonances with respect to the refractive index is shown. For $n > 2$, all main multipoles are well defined, and their spectral positions correspond to a fixed ratio of the wavelength inside the particle, λ/n, to its diameter, $2R$; moreover, increasing n, the scattering efficiency of all multipoles also increases. Notably, provided the high refractive index, different and more complex geometries of dielectric nanoparticles can be chosen to achieve strong, optically induced magnetic dipolar resonances. By changing the geometrical parameters of the particles, the spectral positions of both electric and magnetic dipole resonances can be tuned independently, interchanging or overlapping spectrally at a single frequency for simple geometries [25]. This features provide important opportunities for designing a variety of all-dielectric nanostructures with desirable spectral positions of the resonances.

2.1.1 Directional scattering

In 1983 M.Kerker *et al.* [13] studied the scattering of a magnetic sphere with magnetic permeability $\mu \neq 1$. One of the significant findings of this study was the observation that, when the electric permittivity satisfy the condition $\epsilon = \mu$, the backscattering by the magnetic sphere can be totally eliminated. This effect can be attributed to the fact that under this condition the two sets of the Mie scattering coefficients (Eq.2.3-2.4) coincide for every expansion order. Given the correspondance between the Mie coefficients and electromagnetic multipoles [21], a direct conclusion obtainable from Kerker's work is that a particle supporting overlapped in-phase electric and magnetic multipoles of the same order and magnitude would not scatter backwards. The simplest case of such a configuration is represented by the so-called Huygens's source, employed for antenna engineering [26]. Unfortunately, Kerker's discovery had gradually slip into oblivion, as there exist almost no materials that are naturally magnetic, expecially in the spectral regimes of higher frequencies. With the advent of high-index dielectric particles [20, 23, 27], the situation has dramatically change, thanks to the possible exploitation of nonmagnetic single particles to control scattering not only at the originally discussed forward and backward directions, but also along all other possible scattering angles. Infact, it is worth noticing that the direction of the scattered light totally depends from the direction of the impinging light, being the orientation of the induced dipole moments inside the particle determined by the electric and magnetic incident fields (as shown in Fig.2.3b). This phenomenon is known in the field of *meta-optics* as "First Kerker condition", and it was experimentally verified at the optical frequencies for nanoparticles composed of silicon [28] and gallium arsenide [29]. Analogously, a minimum scattered field in the forward direction is predicted by the "Second Kerker condition" and a zero-forward scattering is reached if some degree of absorbption is present in the scatterer. As the resonances are dispersive, different conditions for forward- and backward-scattered light can be fullfilled at different wavelengths for the same nanoparticle. Therefore, nanoparticles with both electric and magnetic response show different colors depending on the direction from which they are observed [28]. Unidirectional scattering arising from constructive and destructive interference between electric and magnetic dipolar modes in nano-antennas allows to design a variety of metasurfaces [30, 31, 32].

As pointed out before, high-index dielectric particles provides efficient tools for tuning the optically-induced magnetism, and magnetic dipole modes can be made comparable or even stronger than electric dipole modes ([27]) in some spectral regimes, in terms of scattered power. Recent sudies revealed that simple particles (not only dielectric but also metallic or hybrid) can provide a full family of electromagnetic multipoles beyond dipoles, such as electric quadrupole and magnetic quadrupole modes, which renders tremendous opportunities for the observation of different types of the generalized Kerker effects relying on the interfaces between multipoles of different nature (electric or magnetic) and orders [33]. Infact, not only electric dipole and magnetic dipole modes can be overlap in order to suppress backward scattering, but also multipoles of opposite parities (multipoles of same nature but different orders, or multipoles of the same order but different natures). Moreover, still by overlapping higher order multipoles, it is possible to enhance the directionality of the forward scattering.

Within this whole framwork, full of potentialities for directional scattering applications such as resonant coupling with light emitters [34], optical characterization is of fundamental importance, as we will discuss at the end of Section 2.2. However, before covering this topic, it is mandatory to draw a few lines regarding another aspect that is strictly related to the applicability of Mie resonators.

2.1.2 Mie resonators in presence of a substrate

If one of the most important characteristics of dielectric resonators is the angular radiation pattern, as specific eigenmodes are often characterized by distinct radiation profiles, the design of angular or spectrally sensitive photodetectors, and solar cell geometries with optimized light trapping requires a full comprehension of the interaction with the underlying substrate. Next to the possibility of tuning the optical resonances by playing with the particle's size and diameter, the presence of a (high-index) substrate dramatically alters the resonant properties, as well as the interplay between the different eigenmodes. Notably, the presence of a substrate is a main topic when considering dielectric Mie-type optical resonators, since most of practical applications require particles placed on a surface (e.g. absorption in photodiodes [35], solar cells [36, 37], etc.). For resonators that are strongly coupled to a high-index substrate, a large fraction of the scattered light is emitted into the substrate due to the enhanced *Local Density Of States* (LDOS) [38]. Previous studies

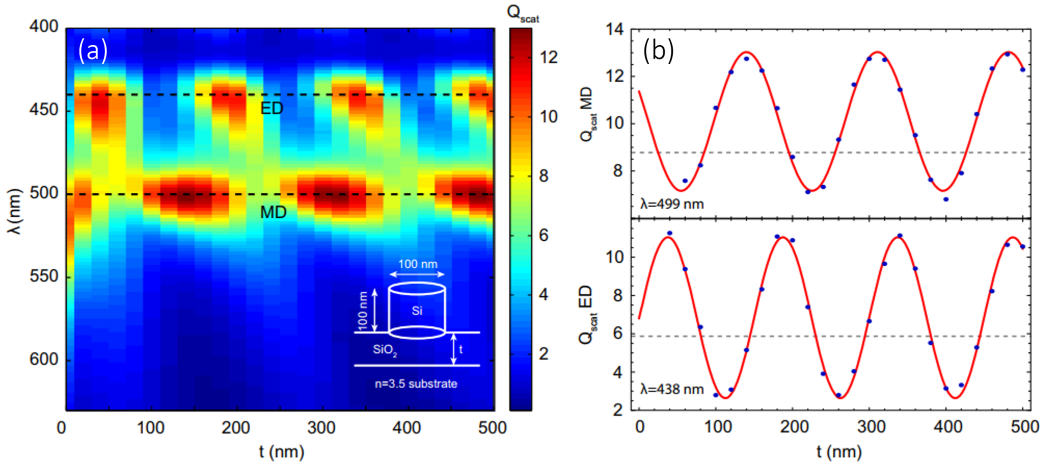

Figure 2.4. **(a)** Q_{scat} as a function of wavelength and oxide thickness t, for a $d = 100$ nm and $h = 100$ nm Si cylinder, positioned on top of an oxide layer with thickness t, on top of a semi-infinite substrate with $n_{sub} = 3.5$. The inset shows the geometry. The horizontal black dashed lines indicate crosscuts at resonance wavelengths: $\lambda = 438$ nm (electric dipole, ED) and $\lambda = 499$ nm (magnetic dipole, MD). **(b)** Top and bottom panels: blue dots represent the cross sections from (a), red lines show the fits from the interference model. The free-space wavelengths found from the fit are shown on the bottom left of the figures. The grey dashed lines show the peak value of Q_{scat} for the same particle on a semi-infinite SiO_2 substrate (limit of $t \to \infty$). Reprinted from [24].

showed that electric and magnetic dipoles resonances exhibit different behaviours in presence of a substrate; the distribution of the radiation pattern of horizontal electric and magnetic dipoles above a high-permittivity substrate reveals that while the magnetic dipole radiates mostly into free space, the electric dipole radiates mostly into the substrate [23]. Other studies [39] have shown that the electric polarizability of a dielectric nanosphere is modified in the presence of the substrate, resulting in a red shift of the electric dipole resonance with respect to Mie's prediction, a phenomenon which is known as "surface dressing effect". Interestingly, it has been recently demonstrated that by tuning the substrate geometry, the electric dipole and magnetic dipole resonances can be selectively enhanced or suppressed [24]. In the work by van de Groep *et al.*, it is reported a systematic study by means of numerical simulations on the resonant properties of high index dielectric particles in the visible spectral range for different particle geometries and dielectric environments. It is demonstrated that it is possible to design any resonator geometry such that the particle is resonant at the desired wavelength. Furthermore the tuning of diameter and height separately allow to obtain either two spectrally separated electric/magnetic dipole (ED/MD) resonances (using a small diameter, large height), or spectrally overlapping resonances (large diameter, small height). For specific applications, such as light trapping geometries in photodiodes and solar cells, it may be useful to have the possibility of selecting one of the two modes to dominate the response of the resonator; the ED or the MD mode. In van de Groep's study it is shown that this can be done using a multi-layer substrate. The particle studied is a Si cylinder with diameter $d = 100$ nm and height $h = 100$ nm, positioned on a SiO_2

layer with thickness t, which is on top of a $n_{sub} = 3.5$ substrate (Si). The thickness of the SiO_2 layer is varied from 0 nm to 500 nm in steps of 20 nm, and for each t the scattering efficiency, Q_{scat}, the scattering cross section normalized to geometrical cross section, is calculated. The results are reported in Fig.2.4, where Q_{scat} is shown as a function of t and λ. One very broad peak is observed for $t = 0$ nm, and this is due to the fact that the resonator is strongly coupled to the substrate and the ED and MD mode broaden and overlap. As t increases the Q_{scat} of the ED and MD mode are subsequently suppressed and enhanced. The horizontal dashed black lines indicate crosscuts near the resonance wavelength for the ED mode ($\lambda = 438$ nm) and the MD mode ($\lambda = 499$ nm), that correspond to the blue dots respectively in the top and bottom panel of Fig. 2.4b. It is possible to observe that the ED and MD modes, appearing at different wavelengths, have different oscillation periods, such that any combination of MD/ED amplitude within the oscillation can be chosen: for example, at $t \sim 400$ nm both modes are in phase while at $t \sim 60$ nm they are out of phase. The physical reason causing this behaviour is the constructive and destructive interference of the incident light reflected from the SiO_2 layer, that generate strong variations in the driving field of the resonator, as follows from a simple interference model. Red lines in Fig.2.4b show the fits from the interference model. This effect allows for both suppression and enhancement of one of the modes: the grey dashed lines in the two panels of Fig.2.4b highlight the peak value of Q_{scat} of the same particle on a semi-infinite substrate ($t \rightarrow \infty$) with index $n_{sub} = 1.5$ (SiO_2), and it is clear that the amplitude of Q_{scat} can be both lower and higher than these values. The modes are never fully suppressed since the amplitudes of the incoming light and the light scattered from the Fabry-Perot cavity do not completely cancel each other.

This phenomenon has opened the roads to exploiting the photonic modulation of the dielectric thick layers to extract more defined structural colours from dielectric Mie resonators [40]. The coupling between Mie resonances of a dielectric nanoparticle and the light interfering in the underlying SiO_2 substrate is a fundamental concept at the basis of one of this work's results, and will be covered in Chapter 5.

2.2 Experimental demonstrations at optical frequecies: state of the art

As discussed in section 2.1, the scattering properties of lossless and non-magnetic materials depend only on two parameters: the refractive index n and the size parameter q. This is clearly shown in Fig.2.3c, where the scattering efficiency is reported as a function of these two parameters. In this map it is deducible that, at a fixed size parameter, the scattering efficiency increases while increasing the refractive index of the nanoparticle, and the resonances become sharper and brighter. This is the main reason for which the first experimental demonstrations of Mie scattering in dielectric materials where performed on extremely high refractive index particles, therefore exhibiting optical resonances at the mid-infrared [41] and gigahertz frequency [42]. In particular, experimental observation of both electric and magnetic resonances in dielectric particles at the mid-infrared was reported in the work by Shuller *et al.* for silicon carbide microrods. Later, dielectric and semiconductor microrods and nanorods were observed to exhibit scattering resonances in the visible and near-IR spectral range [43, 44, 45, 46]. Although Silicon is not a completely loss-free material, its absorption in the visible spectrum is much lower than that of metals, making it a good material for the study of Mie resonances. An experimental demonstration of electric and magnetic dipole resonances at visible wavelength was first reported for spherical Si nanoparticles by Evlyukhin [47] and Kuznetzov [27]. In these works they show how Silicon spheres, whose diameters span over hundreds of nanometers, can support tunable resonances which are related to the 2^n-pole terms of the scattered magnetic field predicted by Mie theory. In the work by Kuznetzov, scattering spectra from Si nanoparticles of various size are collected by means of reflected light dark-field optical microscopy [48], using the white light of an halogen lamp as illuminating source. Dark-field spectroscopy is the most indicated for the study of Mie resonators' scattering properties, and a detailed explanation of this technique is given in Chapter 4, as it is of fundamental importance for the comprehension of this thesis' results. The spectra obtained in [27] are then correlated to the dimensions of the spheres and compared with the corresponding theoretical predictions from Mie theory. Thanks to the analytical Mie solution for the scattered field, the observed spectra can be split into separate contributions of different multipole modes, from which a clear picture of the field distribution inside the particle is deducible. In Fig.2.5 a portion of the complex analyisis made by the group of Kuznetzov on is reported, including both dark-field spectroscopy results and theoretical predictions. According to the study, that is performed on different particles of different sizes, the first strongest resonance of these nanoparticles appearing at higher wavelengths corresponds to the magnetic dipole (MD) response. The electric field inside the particle at this resonance wavelength has a ring shape, while the magnetic field oscillates in the particle center, as it can be observed in the inset of Fig.2.5a(*iii*). Moreover, the magnetic dipole resonance is the only peak observed for the smallest nanoparticles (Fig.2.5a). The visible differences between experimental and theoretical spectra are ascribed to the presence of Silica substrate, which is not taken into account in the simple Mie theory. Infact, as pointed out in the previous paragraph, electric and magnetic dipoles exhibit different behaviours in presence of a substrate. Increasing the nanoparticle size (Fig.2.5b-c), the electric dipole resonance also appears in the blue part of the spectra, while the magnetic dipole shifts to the red. For relatively small particles, the observed colour is mostly defined by the strongest resonance peak, and changes from blue to green yellow and red when the magnetic resonance wavelength shifts from 480 nm to 700 nm (Fig.2.5a-d). Therefore, concluding that the beautiful colours observed at the dark-field microscope correspond to the magnetic dipole scattering of the Silicon nanoparticles, Kuznetsov *et al.* coined the term "magnetic light".

Much of the recent research on Mie resonators has been focused on the optical properties of high-permittivity all-dielectric nanoparticles, with experiments reporting almost far-field measurements. As explained in Section 2.1.1, many works have explored the scattering anisotropy of nano-resonators; however, experimental determination of emission directionality of individual nanoobject has encountered many difficulties due to the inability of angular analysis in conventional optical microscope and very limited information about the multipolar character of higher order optical modes have been provided with standard far-field measurements. Only recently,

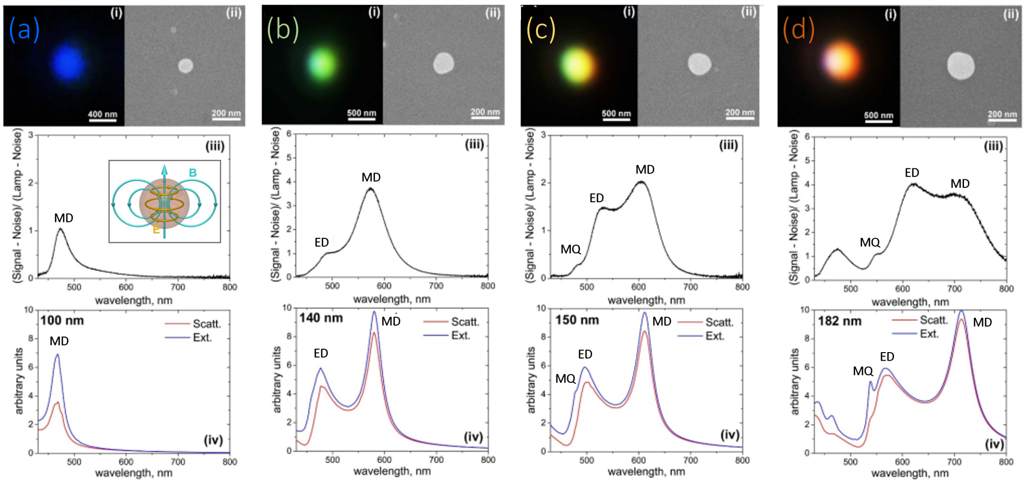

Figure 2.5. **(a)** to **(d)** correspond to nanoparticles of 100nm, 140 nm, 150 nm and 182 nm diameters respectively. The inset in (a) is a schematic representation of electric and magnetic field distribution insideand a high-refractive index dielectric nanoparticle at magnetic resonance wavelength. Close-view dark-field microscope (*i*) and SEM (*ii*) images of the single nanoparticles. (*iii*) Experimental dark-field scattering spectra of the nanoparticles. (*iv*) Theoretical scattering and extinction spectra calculated by Mie theory for spherical silicon nanoparticles of different sizes in free space. Corresponding nanoparticle sizes are defined from the SEM images (*ii*) and noted in each figure. Reprinted from [27].

the Mie scattering from the electric and magnetic dipoles of a single scattering nanosphere has been selectively angle-, polarization- and wavelength- resolved by means of Fourier Plane Spectroscopy [49]. Still, a complete and detailed imaging investigation on far-field properties of higher-order multipolar modes is still lacking. These modes could also allow for targeted near-field coupling to higher-order optical transitions of molecules or doped nanocrystals, or even for coherent nanoparticle-mediated interactions with multiple nanoemitters [50]. So far, the only near-field studies reported in literature on all-dielectric Mie resonators have been performed by means of apertureless (scattering type) near-field scanning optical microscopy [51] and Cathodoluminescence imaging spectroscopy [52], and they are either limited to the collection of the signal in a small area, or do not provide information on more than one optical mode at a time, expecially higher-order multipolar terms.

2.3 Fabrication Techniques: an overview

Whenever an experimental implementation of a specific all-dielectric nanostructure is desired, two crucial factors have to be considered: the choice of a high-index material, and the fabrication method. The degree to which various effects can be enhanced relies on the dielectric response of the chosen material as well as the fabrication accuracy. Moreover, since in the context of nanophotonics applications the main required aims are nanoparticles supporting magnetic and electronic resonances in the visible and near-IR region, nanoparticles' size and shape are the first requirement when a fabrication method is chosen. However, this is not the only aim: also the repeatability and throughput of fabrication methods, precise control of nanoparticle geometry, simplicity of the fabrication procedure and manipulation of nanoparticle arrangement in space play a fundamental role when considering the efficiency of a fabrication technique. In this Section it is presented an overview of the most important methods of fabrication of Mie-resonant high-index nanoparticles that have been developed in the last decades. In Fig.2.6a, some of these techniques are summarized in terms of five representative parameters: repeatability, productivity, resolution, positioning control, and method complexity. A special attention will be dedicated to the *Solid State Dewetting* fabrication method, that has been used to realize the Mie resonators samples analyzed in this work (See Chapter 4 - Samples).

Lithography

The most straightforward methods for fabrication of nanostructures involve lithography, since it provides high repeatability and flexibility to fabricate nanostructures of complicated shapes. The conventional lithographic methods have been successfully applied for the fabrication of single nanoparticles of different shapes. The geometries of these structures can be varied to control the resonant wavelength and relative spectral spacing and composition of the modes. For example, combining Electron Beam Lithography (EBL) and Reactive Ion Etching (RIE), silicon nanoresonators consting of hollow nanocylinders can be made [53], as shown in Fig.2.6b. Also other high-index dielectric materials have been used for lithographic methods, like amorphous alloy with C and O (via electronbeam-induced deposition) [54]. Lithographic micro/nanofabrication processing techniques have been proven to be effective also in terms of large-scale nanostructure array fabrication. This is a matter of great importance for the creation of high-index metasurfaces. In the central panel of Fig.2.6b it is shown an example of Silicon Nanoparticles array obtained by means of RIE through a mask [55]. Recently, also *soft nanoimprint lithography* as been employed for the realization of large-surface arrays of titania-based resonators [56] (bottom panel of Fig.2.6b).

Chemical methods

Chemical methods are promising in terms of higher throughput, felixibility and relative simplicity in synthesis of materials, and compatibility with other methods of solid material synthesis. One of the most widespread methods is chemichal vapor deposition technique, from which spherical silicon nanoparticles can arise [57]. Alternatively, aerosol generation on silicon can be used to obtain spherical nanoparticles [58] (Fig.2.6c). Finally, Alkaline chemical etching combined with electronic lithography is another possible way of fabricating crystalline silicon Mie resonators [59].

Solid state dewetting: Spontaneous and Laser assisted

Dewetting is a ubiquitous phenomenon in nature; many different thin films of organic and inorganic substances (such as liquids, polymers, metals, and semicon-

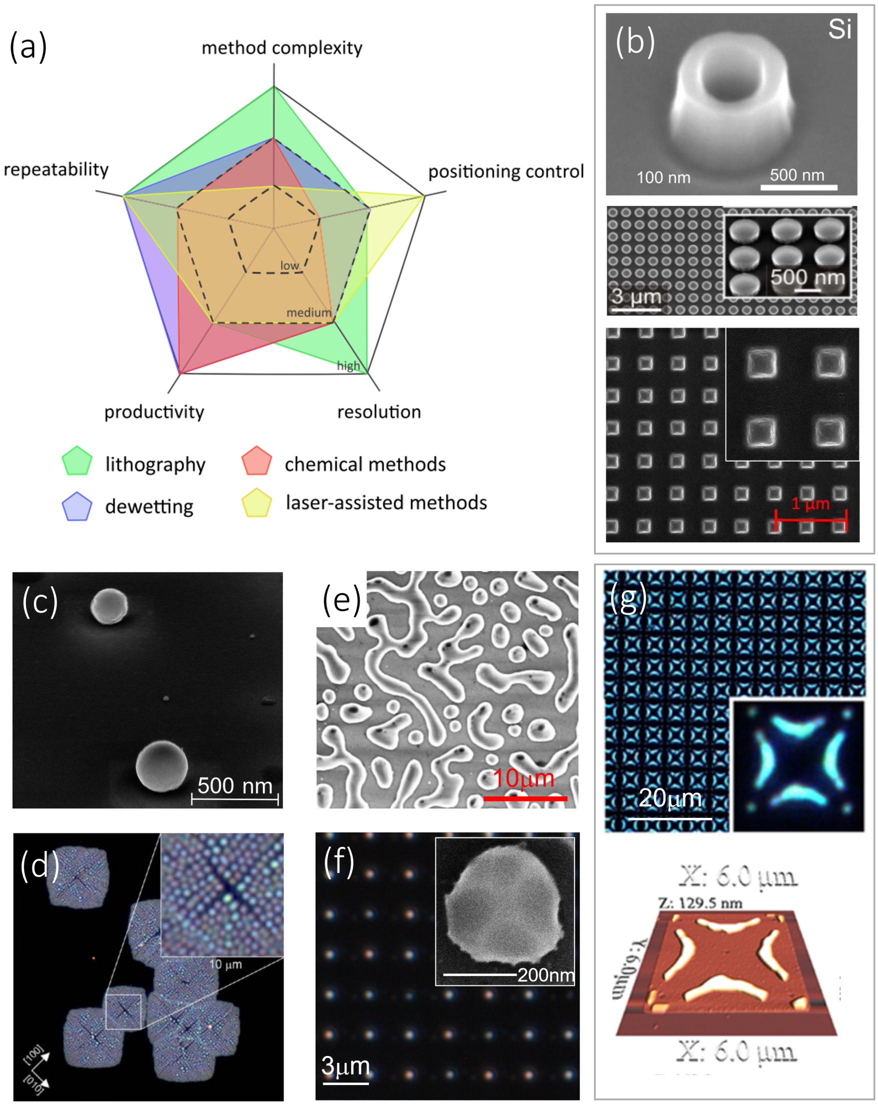

Figure 2.6. **(a)** Schematic comparison of fabrication techniques of high-index nanostructures. Reprinted from [14]. **(b)** Scanning electron microscopy (SEM) images of nano-resonators realized by lithographic methods, from a single hollow Si cylinder (top inset, reprinted from [53]) to ordered arrays of disks (middle inset, reprinted from [54]) and pillars (bottom inset), reprinted from [56]. **(c)** SEM image of two TiO_2 spheres obtained through chemical methods, reprinted from [58]. **(d)** Dark-field optical image of silicon nanoparticles obtained by thin film dewetting. Reprinted from [18]. **(e)** SEM image of a spinodal solid-state dewetted of a thin SiGe layer, reprinted from [41]. **(f)** Array of several hundreds of Si nanoparticles fabricated by assisted dewetting and visualized with dark-field microscopy. The insert shows a SEM image of a single Si nanoparticle in this array (scale bar, 200 nm). **(g)** Optical dark-field microscopy image of controlled dewetted of Si on SiO_2. The upper panel displays the full patterned area while the bottom right inset displays an enlarged view of a single dewetted patch. On the lower part, atomic force microscopy image of the same patch. Reprinted from [18].

ductors) share this shape instability driven by surface tension and mass transport. Dewetting of a thin film is another process that can be applied for fabrication of high-index nanoparticles on large scale. This process implies agglomeration of nanoparticles during heating of a thin film, due to minimalization of total energy of the thin film surfaces, including a film-substrate interface. The film thickness has a direct influence on the dewetting process (the lower the thickness, the higher the driving force for dewetting). Therefore, dewetting can be carried out at temperatures lower than the melting threshold of the thin film material [60, 61]. Silicon nanoparticles with different size and shape are obtained from dewetting of thin crystalline [87] or amorphous [88] silicon films. Silicon monocrystalline resonators assemble togheter to form complex disordered structures (Fig.2.6d). Nanoparticles size and location control can be achieved only by using additional lithographic methods. In spite of this fact, dewetting allows for very high productivity of Mie-like resonators and can be applied to several materials. By changing dewetting parameters, as for instance the substrate temperature during the growth process, different assemblies can be achieved, such as needle-like Te crystallites [62]. Thermal dewetting has been explored also for generating two-component SiGe nanoparticles, and this technique allows modification of the size distribution and the shape of the dewetted particles [63]. In other words, dewetting consitutes a simple and highly productive method for the fabrication of high-index nanoparticles. Spontenous solid state dewetting has recently revealed fascinating complex dielectric scenarios; in the work by Salvalaglio *et al.* [41] it has been shown that monocrystalline semiconductor-based structures, in particular SiGe layers deposited on silicon-on-insulator substrates, can undergo spinodal solid-state dewetting (Fig.2.6e), featuring correlated disorder with an effective Hyperuniform character. The concept of Hyperuniformity will be covered in Chapter 3 and 7. On the other hand, controllable arrangement of size and shape of the particles on the sample is still a problem for this method and can be reached only through addition methods, as for instance lithography (electronic or optical, [64, 65]) and laser-assisted methods. In Fig.2.6f is reported a dark-field image of an array of SiGe islands obtained via dewetting assisted by electron beam lithography, and the inset shows the SEM image of a single monocrystalline island, where the nice facets can be observed [18]. By employing laser radiation, it is possible to pattern thin films of high index materials to control dewetting into nanoscale structures. This can provide routes to controlled self-organization to obtain desiderable patterns formed by solid-state dewetting and a number of studies have demonstrated how surfaces can be intentionally patterned to produce complex architectures on dewetted films (Fig. 2.6g) [65].

Chapter 3

Hyperuniform Disordered Systems

The optics of correlated disordered media is a fascinating research topic emerging at the interface between the physics of waves in complex media and nanophotonics. Inspired by photonic structures in nature, and enabled by advances in nanofabrication processes, recent investigations have unveiled how the design of structural correlations down to the subwavelength scale could be exploited to control the scattering, transport and localization of light in matter. From optical transparency, to superdiffusive light transport to photonic band gaps, the optics of correlated disordered media challenges our physical intuition and offers new perspectives for applications. Hyperuniform Disordered materials are an emerging class of systems featuring anomalous suppression of density fluctuations on large scales, and the underlying hidden order renders them appealing for several applications, such as light management and topologically protected electronic states. In particular, it has been recently demonstrated that Hyperuniform disordered materials can display large, complete photonic band gaps. A study of the light behavior in such systems therefore premises to be fascinating. The purpose of this chapter is to introduce the concept of Hyperuniformity and to describe the features that elevate this class of materials as an ideal synthesis between ordered and disordered photonic systems.

3.1 Light localization in disordered photonic systems

Light propagation through a dielectric medium is determined by the spatial distribution of the material; photons scatter at local variations of the refractive index. For a periodically organized system, interference dominates light tranport and is responsable for optical phenomena in opal gems and photonic crystals [66], that nowadays are the most widespread and versatile devices conceived to mold the flow of light at the nanoscale. However, even in the limit of highly disordered dielectric structures light propagation can still be prevented, and strong mode localization be achieved through the mechanism of Anderson localization [67, 68]. In random media, trans-

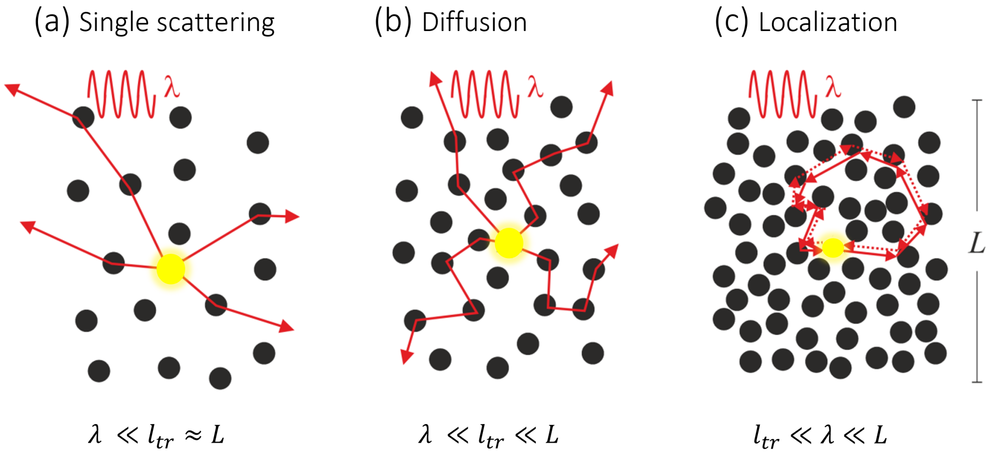

Figure 3.1. Schematics of the three main light behavior regimes in a disordered structure made off randomly placed dielectric spheres for increasing scatterers density. λ is the wavelength of light, the yellow spot is the light source and red arrows describe the light random-walk trajectories. **(a)** Single scattering regime takes place if the scattering mean free path is of the order of the sample size. **(b)** Diffusive regime is found when multiple scattering and the condition $l_{tr} \ll L$ occur. **(c)** Light localization can take place if $l_{tr} \leq \lambda$ occur. Two trajectories propagating in opposite directions along a closed loop exhibit constructive interference and maximize the probability of light to be localized along the loop.

port becomes diffusive through successive scattering events, and light localization occurs as a consequence of coherent constructive/destructive interference in multiple scattering. The physical mechanism behind localization was introduced by Anderson in quantum electron transport [67], in a study that was later on adapted also to sound waves, microwaves, ultracold atoms and light. Of course, given the advantage that no inter-particle interaction is present for photons at moderate intensity, photonic systems are more suitable for studying Anderson localization [69]. Disordered photonic systems are materials in which the refractive index varies randomly in space. In these systems, different light behavior mesoscopic regimes can be found as a function of the light wavelength (λ), the sample size (L) and the photon scattering mean free path (l_{tr}, that quantifies the average distance travelled by the wave-particle between successive scattering events measuring the amount of scattering). Fig.3.1 displays a schematics of the three main light behavior regimes in a random structure made of randomly placed dielectric spheres, classified according to the magnitude of l_{tr} with respect to L and λ. Neglecting absorption, the *single scattering* regime (Fig. 3.1a) describes the case where the photon has a high probability to perform up to one scattering event before leaving the sample exhibiting $l_{tr} \approx L$. In general, the magnitude of the refractive index mismatch determines how strong the scattering will be. Also, the ratio between λ and the size of the scatterer gives the angular dependence of the scattering as well as the scattering cross section in Mie's theory [11]; as we have seen in Section 2.1, if the scatterer size is much smaller than λ, the photon will be scattered nearly isotropically (Rayleigh scattering), while if the size of the scatterer is comparable to λ the photon will be scattered mainly in the forward direction (Mie scattering). When a disordered sample is illuminated by a coherent light source, the outgoing scattered light projected into a screen gives rise to a bright-dark intensity patter, which is called laser speckle pattern. In another scale limit, for $\lambda \ll l_{tr} \ll L$, the photon may scatter many times before exiting the disordered sample. This is known as *diffusive* regime (Fig.3.1b), in which diffused photons undergo multiple scattering events quickly loosing the initial coherence before exiting the sample in a totally randomized direction. The phase of the scattered waves after each scattering event is random, and thus one can model light propagation as a random-walk which leads to a multiple scattering process. However, some interference effects can survive the multiple scattering, as shown by the two closed loop interference trajectories in Fig.3.1c; as the scatterers density increases, and the condition $l_{tr} < \lambda$ holds, a transition from diffusion to localization driven by multiple elastic scattering interference occurs for light. In this case, interference effects are so strong that light transport comes to a halt and the waves become trapped and localized in randomly distributed modes inside the sample. This phenomenon is called Anderson localization regime, in which light behaves as being trapped in an optical nanoresonator. Therefore, disordered structures can sustain optical modes localized at the nanoscale, displaying high spatial and spectral density footprints [70]. Localized modes in random systems however, so far have been proven to exhibit relatively low quality factors (≈ 200 experimentally detected [10, 70]). Lately, a new and promising candidate displaying both the advantages of periodic and random systems is emerging in the field of photonics: hyperuniform disordered media.

3.2 What is Hyperuniformity?

The quantitative characterization of density fluctuations in many-particle systems is a fundamental and practical problem of great interest in the physical, materials, mathematical and biological sciences. Density fluctuations contain crucial thermodynamic and structural information about many-particle systems [71, 72], and their quantification has been used to reveal the fractal nature of structures within living cells [73]. They play a crucial role in charge transfer in DNA [74], or in the dynamics in glass formation [75]. The measurement of galaxy density fluctuations is a powerful way to quantify and study the large-scale structure of the Universe [76]. The unusually large suppression of density fluctuations at long wavelengths (large length scale) is at the center of the concept of hyperuniformity, whose broad importance for condensed matter physics and materials science was brought to the fore only about a decade ago. The study by Torquato *et al.* [77] focused on fundamental theoretical aspects, including how hyperuniformity provides a unified means to classify and structurally characterize crystals, quasicrystals and special disordered point configurations.

A hyperuniform many-particle system in d-dimensional Euclidean space $\mathbb{R}^d$ is one in which normalized density fluctuations are complitely suppressed at very large length scales. One of the important characteristics of point patterns is how the number of points contained in a given volume fluctuate with various disorder realizations; this quantity is related to the notion of spatial uniformity. A hyperuniform

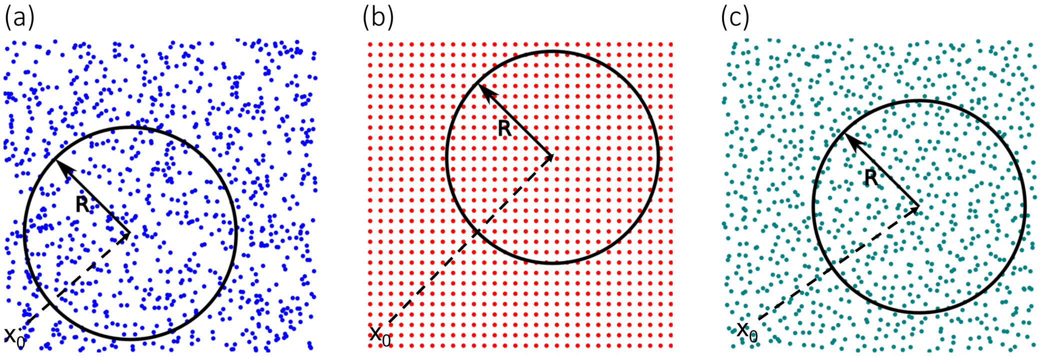

Figure 3.2. Schematics indicating an observation window, in this case a circular window in two dimensions, and its centroid x_0 for a disordered non-hyperuniform **(a)**, periodic **(b)**, and disordered hyperuniform **(c)** point configurations. In each of the three examples, the density of points within a window of radius R will fluctuate as the window position varies. Reprinted from [78].

system is one in which the number variance $\sigma_N^2 \equiv \langle N(R)^2\rangle - \langle N(R)\rangle^2$ of particles within a spherical observation window of radius R grows more slowly than the window volume in the large-R limit, i.e. slower thant R^d. Typical disordered systems, such as liquids and structural glasses, have the standard asymptotic volume scaling $\sigma_N^2(R) \sim R^d$ and hence, are not hyperuniform (see Fig.3.2a). Periodic point configurations (such as the one shown in Fig.3.2b) are an obvious class of hyperuniform systems, since the number fluctuations are concentrated near the window boundary and hence have a the surface-area scaling like $\sigma_N^2(R) \sim R^{d-1}$. Less trivially, many perfect quasicrystals possess the same surface-area scaling as perfect crystals. Surprisingly, disordered hyperuniform patterns, like the one represented in Fig.3.2c have the same asymptotic number-variance scaling behaviors as crystals. This concept become clear by looking at Fig. 3.3a, that shows the number variance (scaled by R^3) as a function of R for four different point configurations in three dimensions at unit density [78]: two disordered Non-hyperuniform systems, the Poisson (uncorrelated) point process (black curve) and a low density equilibrium hard-sphere fluid (green curve), and two different hyperuniform systems, one ordered (red curve) and the other disordered (blue curve). For the first point process (Poisson), the scaled variance is constant for all R, while the variance for a hard-sphere fluid decreases as R increases, but quickly plateaus to a constan asymptotically. Differently, for a hyperuniform system, given the definition of hyperuniformity, the scaled variance tends to decrease a R increases, apart from small-scale variations, and complitely vanishes in the large-R asymptotic limit. Hyperuniform Disordered (HuD) materials are exotic ideal states of matter that lie between a crystal and a liquid: they are like perfect crystals in the sense that they suppress large-scale density fluctuations, a special type of long-range order and yet, they are like liquids or glasses, since they are statistically isotropic with no Bragg peaks, and hence lack any conventional long-range order. These unusual attributes appear to endow such materials with novel physical properties. HuD systems can have a hidden order not apparent on large scales. The right panel of Fig. 3.3b shows a typical scattering pattern of a

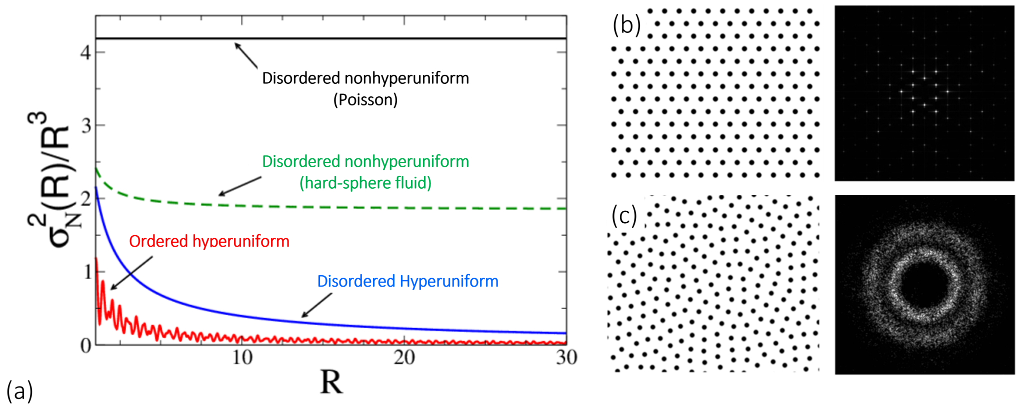

Figure 3.3. **(a)** Number variance $\sigma_N^2(R)$ scaled by R^3 versus R for four different many-particle systems in three dimensions at unity density: disordered nonhyperuniform Poisson uncorrelated (black curve), disordered nonhyperuniform hard-sphere fluid (green curve), disordered hyperuniform (blue curve) and ordered hyperuniform (simple cubic lattice) (red curve) point configurations. Reprinted from [78]. **(b)** Left panel: triangular lattice. Right panel: correspondent Fourier spectrum configuration. **(c)** Left panel: Stealthy hyperuniform point pattern. Right panel: correspondent Fourier spectrum configuration. Reprinted from [79].

crystal (whose point pattern is reported in the left panel), while Fig.3.3c shows the scattering pattern of disordered isotropic hyperuniform system (represented in the left panel). In the latter it is possible to observe a circular region around the origin where there is no scattering, an extraordinary pattern for an amorphous material. Figures 3.3b and c leads us to an alternative definition of hyperuniformity, that is a direct consequence of the number-variance scaling behavior [79]; a hyperuniform point configuration is one in which the structure factor $S(\boldsymbol{k})$ tends to zero as the wavenumber $k \equiv |\boldsymbol{k}|$ tends to zero, i.e.

$$\lim_{|\boldsymbol{k}|\to 0} S(\boldsymbol{k}) = 0, \tag{3.1}$$

implying that single scattering of incident radiation at infinite wavelengths is completely suppressed. Crystalline and quasicrystalline point patterns trivially satisfy this property. In the case of crystalline structures, the structure factor consists of a periodically ordered pattern of Bragg peaks (Fig.3.3b), and its symmetry is inherited from the original point pattern (with an upper bound of six-fold symmetry in two dimensions). Quasicrystalline point patterns are aperiodic point patterns, whose Fourier spectrum consists of a dense set of k-space peaks (obeying the hyperuniformity constraint of $S(\boldsymbol{k}) \to 0$, when $|\boldsymbol{k}| \to 0$) without any upper limit in their rotational symmetry (n-fold symmetric quasicrystalline point patterns, with n an arbitrarily large integer, are possible). The point pattern represented in Fig.3.3c comes from a further constrain in disorder, and is called *stealthy* hyperuniform. Stealthy point processes are those in which the structure factor is exactly zero for a subset of wavevectors, meaning that they completely suppress single scattering for these wave vectors [80]; for extension, *stealthy hyperuniform* patterns are a subclass of hyperuniform systems in which $S(\boldsymbol{k})$ is zero for a range of wave vectors around the origin [81]:

$$S(\boldsymbol{k}) = 0 \text{ for } 0 \leq \boldsymbol{k} \leq K \tag{3.2}$$

where K is some positive number. Interestingly, perfect crystals actually are stealthy hyperuniform patterns. For these reasons, among the many fields of application that hyperuniformity has been crossing in the past decades, photonics is one of the most promising.

3.3 Hyperuniform disordered photonics

Photonic bandgaps (PBGs) are one of the most striking manifestations of structural parameters on optical transport. A photonic gap, similarly to electronic gaps in semiconductors, correspond to a spectral window in which no propagating modes can exist. The PBG concept is known in optics since the early works on (one-dimensional) thin-film optical stacks [82], emerging as a consequence of the periodic modulation of the refractive index on the wavelength scale. The idea was generalized to two and three-dimensional periodic structures [83, 84] in the late 1980s, and has been at the heart of research in optics and photonics for about two decades. The interest in photonic gaps comes from the possibility to engineer defect states with high quality factors and wavelength-scale confinement, providing the opportunity to control spontaneous light emission and light propagation for applications in all-optical integrated circuits [66]. It is widely believed, in the photonics community, that the opening of photonic gaps requires the refractive index variation to be periodic in space, or in other words, the structure to exhibit long-range periodic correlation. However, several studies have been made on the impact of structural imperfections on optical properties, and they revealed that certain gaps could persist even in absence of periodicity [85], thanks to local (Mie or short-range correlated) resonances [86, 87]. Later reports on photonic gaps in 3D disordered structures exhibiting short-range correlations [88], along with the introduction of hyperuniformity as a requirement in photonic gaps in 2D systems [89], greatly stimulated the community to unveil the relation between local morphology and structures and the opening of spectrally wide gaps [90].

The concept of hyperuniformity in photonics has first been introduced in a numerical study by Florescu *et al.* [89]. In this paper, Florescu *et al.* demonstrated that it is possible to design 2D, isotropic, translationally disordered photonic materials of arbitrary size with large, complete PBGs. Although obtaining complete PBGs in dielectric materials without long-range order is counterintuitive, it was explained in the large dielectric constant ratio limit by a combination of hyperuniformity, uniform local topology, and short-range geometric order. Important efforts have been put since then on the fabrication of hyperuniform disordered systems, which could be achieved so far by lithography in 2D [91], and 3D [92], block copolymer assembly [93], emulsion routes [94], and spinodal state dewetting [41] (as explained in Section 2.3). These pioneering experiments on photonic hyperuniform disordered systems have explored IR light diffraction in 3D dielectric structures [92], microwave bandgaps formation [91], polarization filtering [95], random cascade lasers [96], along with visible light scattering experiments from HuD plasmonic gold surfaces [97].

Moreover, theoretical proposals have been put forward for surface enhanced Raman scattering [98], transparency design [99], high-Q optical cavities [100] and low-loss waveguides [101], and microwave photonic circuits [91]. Still, a quantitative experimental demonstration of the variety in light transport regimes possibly hosted by HuD systems, from Anderson-like localization to diffusive multiple scattering (as we will see in Section 3.3.2) is still missing in the optical range [102]. One of the aims of this thesis is to provide the first near-field optical characterization of HuD photonic structures in the near-IR (Chapter 6), and in the next section we provide a description of the protocol adopted in [89] to create large, complete PBGs in HuD dielectric structures like the ones experimentally studied.

3.3.1 Photonic bandgap in HuD systems

In order to design hyperuniform disordered materials with large, complete PBGs in 2D, Florescu *et al.* employ a tessellation protocol based on a developed collective coordinate approach [103]. The protocol allows to generate a “relaxed” dual lattice, a connected network structure whose vertices are trihedrally coordinated. It begins with the selection of a point pattern generated by any means with the rotational symmetry and translational order desired for the final photonic material. If the goal were to have a band gap only for TM polarization (electric field oscillating along the azimuthal direction), replacing each point of the pattern with a circular cylinder and varying the radius of the cylinders until the structure exhibits a maximum TM bandgap, would be enough. But since the goal is to achieve a complete PBG (both for TM and TE polarizations), the best results are obtained with a planar, continuous trivalent network [104] (as in the case of the triangular lattice), which can be obtained from the point pattern in the following steps (Fig.3.4a):

- The chosen point pattern (light blue dots) is partioned by using a Delaunay triangulation (thin lines);

- The centroids of the neighboring triangles (black dots) of a given point are connected (red lines), generating cells around each point, as shown in the left top of Fig.3.4a, where a yellow point is sorrounded by five cells corresponding to five (green) Delaunay triangles.

Once the tessellation of cells is done, the cell edges are decorated with walls (red lines in Fig.3.4a) of dielectric material of uniform width w. Then the width of the walls is varied until the maximal TE bandgap is obtained. A final step consists in overlapping the TM and TE bandgaps by decorating the vertices of the trivalent network of cell walls with circular cylinders of radius r (black holes in 3.4a). Then, for any set of dielectric materials, the maximum complete PBG is achieved by varying the only two free parameters, r and w. For the optimization of these two degrees of freedom, the photonic mode properties must be computed as parameters are varied. For this, due to computational cost, a supercell approximation method is used, along with the conventional plane expansion method [66, 105]. A disordered pattern within a box of side length L (with periodic boundary conditions) where L is much greater than the averaged interparticle spacing is generated in the limit of large L. Interestingly, the PBG for disordered heterostructures obtained with

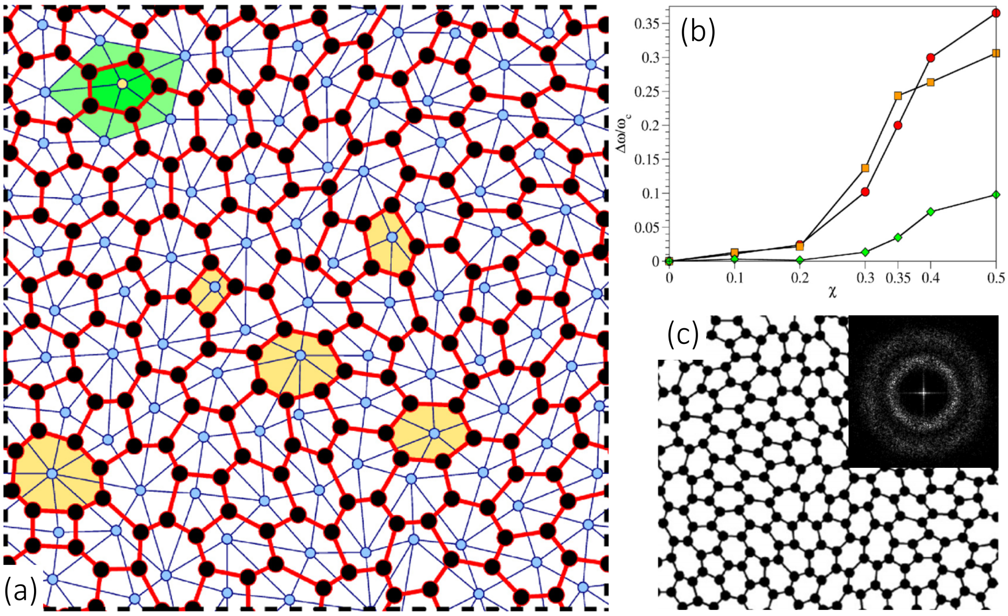

Figure 3.4. **(a)** Protocol for mapping point patterns into tessellations for photonic structure design. **(b)** Trend of TM (red circles), TE (organge squares), and complete (green diamonds) photonic band gaps with respect to χ. **(c)** Design of stealthy hyperuniform pattern of $\chi = 0.5$ obtained with the tessellation protocol. The inset shows the structure factor $S(\boldsymbol{k})$, precisely zero within a certain range of $k < K$. Reprinted from [89].

the protocol turns out to be equivalent to the one in periodic systems, since the spectral location of the TM gap is for example determined by the resonant frequencies of the scattering centers, and always occurs between band N and $N+1$ (with N the number of points per unit cell). This behavior underscores the relevance of the individual scattering center properties on the band gap opening. Moreover, it is important to notice that it can be interpreted in terms of an effective folding of the band structure, conceived as a result of scattering on a collection of N similar (but not necessarily identical) scattering units distributed hyperuniformly in space. The optimal results for the BGP in terms of spectral width and stability are obtained by considering the *stealthy* subclass of hyperuniform point patterns (whose definition we have given in the previous section, Eq.3.2). In particular, here and in the experimental demonstrations obtained in this thesis, are considered stealthy point patterns with a structure factor $S(\boldsymbol{k})$ that is isotropic, continuous and precisely equal to zero for a finite range of wavenumbers $k < K$ for some positive K. Stealthy hyperuniform patterns are parameterized by χ, known as "stealthiness parameter", and defined as the fraction of wavenumbers $\boldsymbol{k}$ within the Brillouin zone that are set to zero; as χ increases, the degree of hyperuniformity increases (the number variance tends to decrease more). Of course, when χ reaches a critical value ($\chi \approx 0.77$ for 2D systems) the pattern encounters long-range translational order. As expectable, the largest PBGs in hyperuniform patterns occur in the limit of large dielectric contrast; the band structure computations here reported assume that the photonic materials are composed of silicon and air. In Fig. 3.4b it is shown how TM (red circles), TE (organge squares), and complete (green diamonds) photonic band gaps evolve by increasing χ, i.e. the degree of hyperuniformity. From this graph it is clear that significant band gap begins to open for the stealthy hyperuniform designs for sufficiently large $\chi \approx 0.35$ (but well below K), at a value that in reciprocal space corresponds to the emergence of a range of "forbidden" scattering, $S(\boldsymbol{k}) = 0$, surrounded by a circular shell just beyond $|\boldsymbol{k}| = K$ with increased scattering. This behavior is represent by Fig.3.4c, where it is reported the design of a stealthy hyperuniform pattern with $\chi = 0.5$, and the structure factor $S(k)$ (in the inset), precisely zero within the inner disk. Summing up, complete photonic band gaps can occur in disordered systems that exhibit a combination of hyperuniformity, uniform local topology, and short-range geometric order. We resume the main reasonings at the basis of this trivalent combination.

1. Photonic crystals are hyperuniform.

2. Hyperuniform stealthy patterns with $\chi < 0.35$ (Fig.3.4b) do not produce sizable, complete PBGs, whereas those with $\chi > 0.35$ do. In particular, the main difference between the two sets depend on the local enviroment: the degree of short-range geometric order, the variance in the near-neighbor distribution of link lengths, and the distance between centers of neighboring links [89]. Therefore, both hyperuniformity and short-range geometric order are required to obtain substantial PBGs.

3. Band gaps arise in the limit of large dielectric constant ratio; in this limit, and for the optimal link widths and cylinder radii, the interaction with electromagnetic waves is in the Mie scattering limit (see Chapter 2.1). At frequencies near the Mie resonances (which coincide with the PBG lower band edge frequencies [87]), the scattering of TM (TE) electromagnetic waves in a heterostructure composed by parallel cylinders (walls in the azimuthal direction) is similar to the scattering of electrons by atomic orbitals in cases where the tight binding approximation can be reliably applied [86]. However, to obtain a complete PBG, some compromise must be found to enable it for all directions $\boldsymbol{k}$. For this purpose, uniform local topology is advantageous, and in 2D is found in the trivalent network (corresponding to the random tetrahedrally coordinated networks used as models for amorphous silicon and germanium in 3D [106]), a uniform topology which is automatically imposed by the protocol.

3.3.2 Light localization in HuD systems

Just like light propagation in photonic crystals can be understood in analogy of the electrons motion inside semiconductor crystals, the comparison to electronic band gaps is also useful in characterizing the states inside HuD photonic systems [66]. For a perfectly ordered crystal (or photonic crystal), the electronic (photonic) states at the band edge are propagating such that the electrons (electromagnetic fields) sample many sites. If modest disorder is introduced, localized states begin to fill in the gap so that the states just below and just above are localized. Although formally the disordered heterostructures do not have equivalent propagating states, an analogous phenomenon occurs. In particular, just like states of the upper and

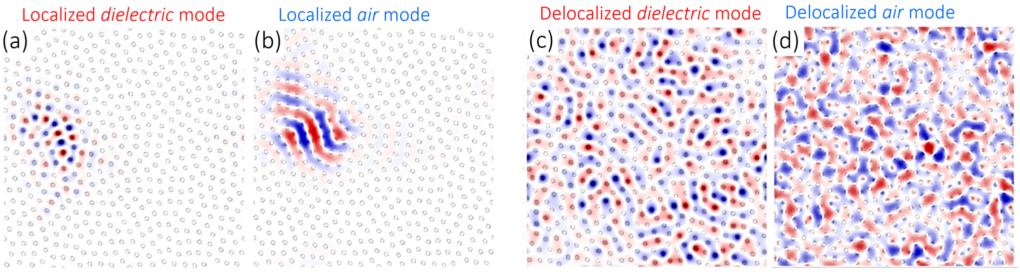

Figure 3.5. Electromagnetic field distributions in hyperuniform disordered structures. The structure consists of dielectric cylinders (radius $r/a = 0.189$, where $a = L/\sqrt{N}$ and dielectric constant $\epsilon = 11.56$) in air arranged according to a stealthy hyperuniform distribution with $\chi = 0.5$. Electric field of localized modes of the lower band edge **(a)** and upper band edge **(b)**, labeled as *dielectric* or *air* modes in analogy with photonic crystals syntax. Electric field of delocalized modes of the lower band edge **(c)** and upper band edge **(d)**. Reprinted from [89].

lower band edge in photonic crystals, known as *air* or *dielectric* states, defect states occur at the edges of HuD bandgap. These Anderson-like localized modes occur naturally at the PBG edges and are predicted to spread over a few cells of HuD network structures, and they can be easily distinguishable as above (below) the PBG according to their electric field distribution being concentrated in air (dielectric). The physical reason is that below the bandgap, TE modes concentrate the magnetic field inside the air fraction (electric field concentrated in the dielectric material) as to reduce the electromagnetic energy functional [91]. Above the gap, due to the requirement that solutions to the Maxwell-eigenproblem are orthogonal, the magnetic field is pushed into the dielectric material as nodes form in the air fraction; this is a well understood paradigm in periodic structures [66] that can be observed also in HuD systems. An example of dielectric (air) localized mode of the lower (upper) band edge is shown in Fig.3.5a (b), where the calculated (via plane expansion method [66, 105]) electric field distribution in a 2D HuD structure for TM polarized radiation is reported [89]. The structure consists of dielectric cylinders (radius $r/a = 0.189$, where $a = L/\sqrt{N}$ and dielectric constant $\epsilon = 11.56$) in air arranged according to a stealthy hyperuniform distribution with $\chi = 0.5$. Interestingly, from the field profiles the method of wave transport can also be inferred. As modes depart from the gap, they begin to display an extended profile that suggests *diffusive* propagation (3.1 b, Section 3.1); this can be observed in Fig.3.5c and d, where the electric field of delocalized modes from the lower (upper) band are reported respectively. Further depart from the PBG in terms of frequency, leads to a *ballistic* propagation regime. A clarification must be made regarding the type of localization encountered in HuD structure; similarly to other conventional disordered structures, unperturbed HuD systems display defect modes. In Fig.3.5a-b we have introduced localized modes that occur naturally at the photonic band gap edge, extending over five to ten cells, and we referred to them as "Anderson-like". However, how proper is the "Anderson-like" label for localized modes at the PBG edges? Imagine a periodic structure which is sequentially disordered. As disorder is introduced, modes start to populate the PBG; now consider that one increases the disorder from very small amount to very large. There will be two types of localized modes in the gap, and some of them will be located deeper/est in the gap. These modes are clearly localized, in fact they display the tightest localization, and they are promoted into the gap due to peculiar topology [100], and therefore they are called "*topological defects*" (the four-fold and eight-fold yellow cells in Fig.3.4a can clearify what local topology means in this context). In some sense, these are improper Anderson-localised modes because they require disorder in order to exist and they will vanish as the disorder is increased - hence they are also *accidental.* Infact, they represent a very specific configuration, and increasing disorder will mean washing it out by similar configurations existing nearby. An example of topological (or accidental) mode will be give in Chapter 6. The second types of localized modes are the ones with lower localization length placed to the left (frequency domain) of the accidental modes discussed above. These modes, like the ones of Fig.3.5a-b, are called genuine Anderson localized modes by Florescu *et al.* since their localization length decreases as disorder is increased. These modes are still in the neighborhood of the band edge but again have a somewhat larger localization length. An experimental analysis of the different light transport regimes in a HuD photonic structure, realized by means of near-field hyperspectral imaging, will be described in Chapter 6.

A final consideration should be done regarding the photonic band gap in HuD systems. As clearly deducible from Fig.3.5, the formation of the TM band gap is closely related to the formation of electromagnetic resonances localized within the dielectric cylinders, and there is a strong correlation between the scattering properties of the individual scatterers and the band gap location. In particular, the largest TM gap occurs when the frequency of the first Mie resonance of the cylinders coincides with the lower edge of the PBG, as theoretically proven in the work by Rockstudhl *et al* [87]. In this thesis, the correlation between single-cylinder properties and bandgap formation in photonic structures (quasicrystals and random) is analyzed; it is shown explicitly that gaps are associated with Mie resonances, as they open whenever the scattered field is out of phase with the incident field, and no propagation channel exists for light. Therefore, within the framework of a study on light localization in complex structures like HuD photonic systems, also a deep understanding of Mie scattering by nanoparticles is an relevant task to be achieved. This conceptual link is at the basics of this thesis, and will be further developed in the next Chapters.

Chapter 4

Experimental methods

In this Chapter we address the methods that have been used to obtained the results presented in this thesis. In particular, the first two sections are relative to two optical experimental setups, highlighting their main potentialities and principles of operation: in Section 4.1 the *Scanning Near-field Optical Microscope* (SNOM) is presented, and after a brief overview on the different configurations in which it can be exploited, and on the fabrication process of the probes, the complete mechanism at the basis of the Hyperspectral Imaging technique is described. In Section 4.2 we move to the description of how *Dark-field spectroscopy* was implemented on the SNOM microscope. Suitable for non-optically active samples like scatterers, this technique is presented along with the different geometries in which it can be exploited. If on one hand near-field and dark-field optical characterization of complex nanostructures provide an efficient mean of comprehension of light localization, numerical simulations are a powerful tool to complete the investigation protocol and to approach aspects that are not accessible with experiments. In particular, in the last Section (4.3) we focus on Finite Difference Time Domain (FDTD) and Finite Element Method (FEM) simulations, that have been used in this work to interpret the results that will be presented in the next chapters. These numerical tools, two of the most important and versatile methods that belong to the emerging field of *Computational Electromagnetics*, are complementary, and of fundamental importance for the comprehension and characterization of light confinement in dielectric nanostructures.

4.1 Near-field scanning optical microscopy

As we have seen in Chapter 1, characterization of light emitting nanostructures, in order to get access to the information contained in evanescent waves (Section 1.2), requires procedures in which the e.m. fields are probed in close proximity of the sample, i.e. where evanescent are not yet totally suppressed, and cannot be achieved through traditional microscopy. At the beginning of the last century, Synge and Bethe [107, 108] suggested to work with apertures characterized by dimensions smaller than the light wavelength in order to take advantage of the high spatial resolution of the evanescent waves. In direct vicinity of the aperture, the spatial resolution of an optical system is defined by the dimension of the pinhole rather than by diffraction, and can thus be reduced below the diffraction limit by sufficiently decreasing the size of this aperture. However, only at the end of the last century (in 1984), after the invention of the scanning tunneling microscope [109], nanometer-scale position technology was actually available, and an optical microscope similar to Synge proposal was realized [110, 111, 112], namely the *Near-field Scanning Optical Microscope* (SNOM). The key innovation was the fabrication of a sub-wavelength optical aperture at the apex of a sharply pointed transparent probe tip that was coated with metal. In addition, a feedback loop was implemented for mantaining the tip at a constant distance (of only a few nanometers) from the sample during the scanning [35], in analogy with other raster-scanning techniques as *Atomic Force Microscopy* (AFM). This integrated microscopes work in close proximity with the sample surface, thus strongly interacting with optical near-field and evanescent waves. The principle of SNOM imaging operation relies on the point-by-point investigation by raster-scanning the local probe over the sample surface and recording at every position the corresponding optical signature. The local probe acts as an optical antenna, converting localized e.m. fields into radiation, and vice versa. Therefore, SNOM detection gives ultra-sensitive optical measurement beyond the diffraction limit and provides light behaviour at the nanoscale, together with the topographical capability of the AFM imaging. Although the morphological performance is not as good as in cantilever based AFM, SNOM proved to be the state of the art technique for investigating nanostrucures such as quantum wells, quantum dots, nano-resonators or for single molecules since it combines the excellent spectroscopic and temporal selectivity of classical optical microscopy with the sub-wavelength spatial resolution [113, 114, 115]. SNOM technique was systematically advanced and extended over the years to various configurations, that are resumed in Figure 4.1. Aperture probes 4.1 (a-c) can be used in the near-field in three configurations: the first is the *illumination/collection* geometry, where both the excitation and collected signal occur through the probe, as displayed in Fig.4.1a. This scheme is the best suited for improving the spatial resolution since it provide an almost background free illumination. The probe can also be used only in *collection* configuration (Fig.4.1b), in which far-field light illuminates the sample in reflection or transmission (or it is coupled inside it), and the near-field is collected by the tip. Collection configurations as (a) and (b) are suited for employing aperture or dielectric probes, that allow the conversion of evanescent waves with high spatial frequencies to e.m. fields propagating through the optical fiber and finally measured by conventional far-field detector. In Fig.4.1c is sketched the *illumination* configuration, the case in which the aperture probe illuminates a small area of the sample surface, and the resulting signal from the interaction with the sample is then collected in the far-field both in transmission or in reflection. In Fig.4.1d SNOM setup is based on sharply pointed apertureless tip (a-SNOM) that locally enhances light scattering. Both illumination and collection are in the far-field, therefore a-SNOM requires a sophisticated method for filtering out the huge background.

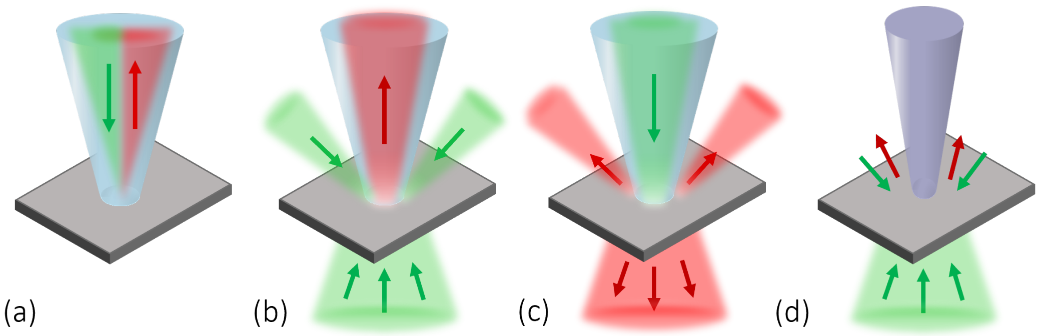

Figure 4.1. Schematics of the six more widespread SNOM configurations, divided into four principles of operation. **(a)** *Illumination/collection* geometry, in which both the near-field illumination (green) and collection (red) occur through the tip. **(b)** *Collection* mode, in which far-field light illuminate the sample in reflection or transmission, and the near-field is collected by the tip. **(c)** *Illumination* mode, where the incoming light illuminates the sample in the near-field by means of an aperture probe and the reflected or transmitted light is detected in far-field. **(d)** Scattering mode, where apertureless probe enhances the scattering in the near-field, whose information are analyzed by far-field detection.

4.1.1 Probe fabrication

The fundamental element of a SNOM setup is the near-field probe, as it defines the spatial resolution, the amount of detected signal and the induced perturbation on a given sample. Many different near-field probe designs have been conceived and tested in the last decades, and they can be grouped in four categories: (*i*) dielectric, i.e. transparent, probes that are also called uncoated tips [116], (*ii*) metal coated aperture probes [117, 118, 119], (*iii*) pointed probes (used in a-SNOM setup) [120], (*iv*) probes functionalized by placing a nano emitter [121] or a plasmonic nanoantenna at the tip apex [122, 123, 124]. The experimental results presented in this thesis were obtained with dielectric tips, and in this section it is summarized the fabrication process employed to realize them.

A well established method for fabricating smooth dielectric tapered probes is the *tube etching* method [116, 125]. We exploit this recipe to produce by ourselves the dielectric probes employed in the SNOM experiments. Glass tip formation occurs inside a cylindrical cavity formed by the polymer coating of an optical glass-core fiber which is not stripped away prior to etching in aqueous 48% hydrofluoric acid. The two basic steps of the etching mechanism are reported in Fig.4.2a and b. In the first one the acid largely corrodes the lateral side of the fiber core with respect to the central part since at the rim of the glass cylinder HF supply occurs out of a larger volume as compared to the central region. As soon as the the preliminary taper is formed, step convection driven by concentrations gradients that are influenced by the etching process itself and the gravitational removal of the reaction products delivers HF to the upper cone region. After about 90 minutes of tube-etching the fiber is rinsed with ethanol and successively the jacket is removed without damaging the cone. During the etching procedure the solution is covered by an organic overlayer (isooctane) to protect the fiber against acid vapor. Moreover,

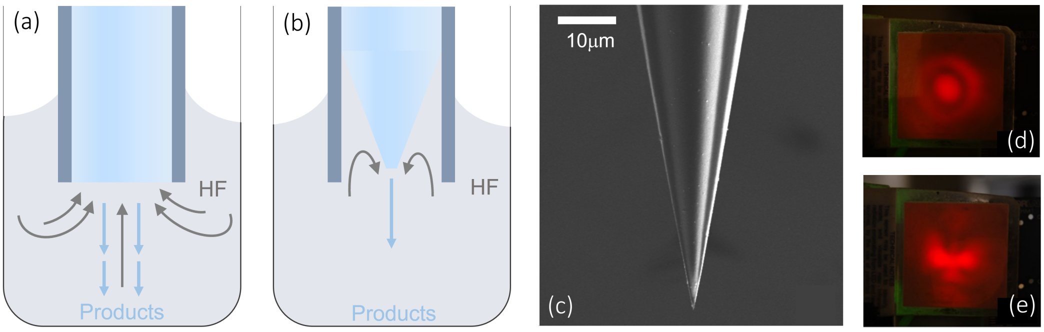

Figure 4.2. Dielectric tapered fiber etching process in aqueous hydrofluoric acid. **(a)** First etching step: diffusive motion of the HF solution. **(b)** Second etching step: convective motion of the HF solution. **(c)** SEM image of a properly etched dielectric fiber, where the lateral walls are characterized by a relatively smooth surface. **(d)** Emission from a SNOM tip well fabricated; the Airy Disk pattern is present on the screen. **(e)** Emission from a failed SNOM tip.

since the whole etching process takes places inside a hollow cylinder formed by the protective jacket, it is less sensitive to environmental influences such as vibrations or temperature drifts. The procedure gives tapered probes with large cone angles (about 25°) and small apex (less than 100 nm size), resulting in a strong decrease of the loss region with respect to pulled probes [126]. Dielectric tips with reproducible shapes and optical performance are fabricated in a high yield, as the one reported in the SEM image of Fig.4.2c. Since glass is almost totally transparent in the visible and near-infrared spectral range, these tapered dielectric probes show a high throughput (more than 50%) thus being suited for the high-contrast *illumination-collection* geometry. Once that probe is fabricated, we test its optical performance: after coupling the tip with a laser (emitting at 633nm or 1300nm depending if the fiber is suited for the visible or the near-infrared range), we check the presence of the Airy Disk diffraction pattern on a screen (as shown in Fig.4.2d); this assures that the etching process has determine the correct and complete circular shape of the tip apex. If not, an irregular diffraction pattern will appear, as displayed in Fig.4.2e. At this point, the probe with a clear Airy disk is glued on a piezoelectric mount that will allow the connection with electronic setup, as explained in the next section.

4.1.2 SNOM experimental setup

In the previous pages we stated that the main condition to be satisfied in order to achieve a sub-wavelength imaging below the diffraction limit is that the probe has to be placed at a distance from the source (i.e. the sample) which falls in the near-field spatial regime of detection. In this section it is reported an explanation of the feedback mechanism employed to achieve the near-field regime during a SNOM experiment, and then it is given a description of the experimental set up used for the measurements reported in this thesis.

Once the fabrication process described in Section 4.1.1 is completed, the optical

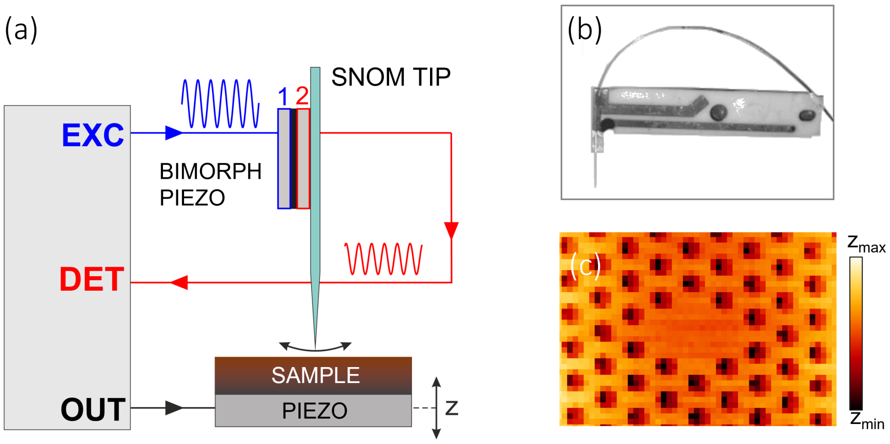

Figure 4.3. **(a)** Sketch of the SNOM tip glued to the bimorph piezoelectric controller and of the feedback mechanism as it approaches the sample. The excitation piezo is highlighted in blue (1) and the reading piezo in red (2). **(b)** Image of the optical fiber that ends with a SNOM tip. **(c)** Typical topographic map of a photonic crystal cavity acquired during a SNOM scan. The scalebar is relative to the minimum (z_{min}) and maximum (z_{max}) z position of the tip.

fiber that ends with a sharp tip is glued on an insulating module equipped with a piezoelectric bimorph, as shown in Fig.4.3a and b, following the scheme developed in [127]. The bimorph is made of two plates of piezoelectric material (with opposite polarization vectors) highlighted in blue (1, called *exctiation* piezo) and red (2, called *detection* piezo); if a voltage is applied to the bimorph electrodes, one of the plates will extend and the other one will be compressed, resulting in a bend of the whole element. In order to control the probe-sample distance the excitation piezoelectric (blue), induces a small lateral tip oscillation at the system own resonant mechanical frequency (about 60 KHz), parallel to the sample surface, if a sinusoidal voltage at the proper frequency is applied; at the same time the detection piezoelectric (red) measures the effective tip oscillation signal with amplitude and phase. As the probe approaches the surface, due to probe-sample interacting shear forces that are effective only at few nanometers distances, the detected amplitude decreases and the relative phase between the excitation and detection signals changes. Then, an electronic feedback drives the sample stage scanning piezo along z in order to keep constant this phase difference, thus ensuring a constant probe-sample distance throughout the whole scan. Clearly, by reporting the analogical signal that controls the z piezo as a function of the tip position, it is possible to map the surface topography resembling the AFM detection, as the electric signal is translated into a spatial information. Furthermore, the near-field detection condition is satisfied since by a proper calibration of the measured phase difference we can fix the tip-sample distance in a range between 5 nm and 20 nm, which corresponds to the near-field regime for visible or infrared laser light. An example of a typical topography acquired during a SNOM measurement on a photonic crystal cavity is reported in Fig.4.3c.

We now address the description of the whole SNOM experimental setup, whose schematic representation can be found in Fig.4.4. The whole mechanism is based on a room-temperature commercial scanning near-field optical microscope (*Twin-SNOM* by *Omicron*) assembled on an optical *Zeiss* microscope conveniently modified to house the tip holder together with the scanning stages. The standard optical microscope is exploited for correctly positioning the probe on the position of the sample surface to be investigated, but it also gives the possibility to measure light behaviour in the far-field region as a confocal microscope. The sample is mounted on piezoelectric stages (P-500 by *Physik Instrumente*) that enable a nominal spatial accuracy in the directions x, y and z (where the xy plane is parallel to the sample surface) equal to (1; 1; 0.1) nm in the range (100; 100; 10) µm. The scanning speed is kept sufficiently low to prevent artefacts caused by the limited photo detector acquisition time. In this thesis two SNOM configurations were used:

- The *illumination/collection* geometry, sketched in Fig.4.1a, was used in the near-infrared optical range, to analyze near-field PL emission of optically active samples (like the ones described in Chapter 6). Many laser sources are available in the visible and the near-infrared spectral range; in this case, a solid state laser emitting at 785 nm was used for the excitation. In the excitation path, collimated laser light passes through a dichroic mirror (D) that selectively transmits visible light (up to 1.0 µm) with high efficiency (up to 90%) and reflects near-infrared light with the same amount of efficiency, before being coupled into the near-field probe. The laser power emission is possibly adjusted by neutral density filters and the optical fiber used is a single mode fiber operating at 1300 nm. The sample near-field signal PL (in red color in Fig.4.4a) is collected by the same probe, reflected by the dichroic hot mirror, dispersed by a spectrometer (with a 10 cm focal length L) and finally detected by a liquid nitrogen-cooled InGaAs array detector (by *Princeton Instruments*, equipped with an array of 1024 photodiodes). Inside the spectrometer three diffraction gratings are available, respectively one with 600 lines/mm (with 1.0 µm blaze), and two with 150 lines/mm (with 1200 nm and 500 nm blaze). The spectral dispersion for the three grating, in the different spectral range in which they have been used, is: 0.11 nm/px and 0.52 nm/px (in the near-infrared).

- The *collection* geometry is better suited for measurements of non-optically active samples like Mie resonators (like the ones analyzed in Chapter 5), that under tilted illumination from a pulsed Supercontinuum laser source ($SC-Laser$ by *Leukos-STM*), can scatter light that will be collected by the SNOM tip (as sketched in Fig.4.4b). Infact, to detect all the possible scattering resonaces of these sample, broadband sources like lamps or supercontinuum lasers are recommended; the flat emission spectrum of the $SC - Laser$ is reported in the inset of Fig.4.4b. The setup previously described (Fig.4.4a) is completely interchangeable in the visible spectral range, and the principle of usage stays basically the same, apart from some functional substitutions; firstly, all the optics (mirrors, lenses) are achromatic, in order to avoid chromatic aberrations effects that can be detrimental for spectrally broad excitation/collection in the visible. The element D (Fig.4.4a) is substituted by a beam-splitter

(a) ILLUMINATION/COLLECTION CONFIGURATION

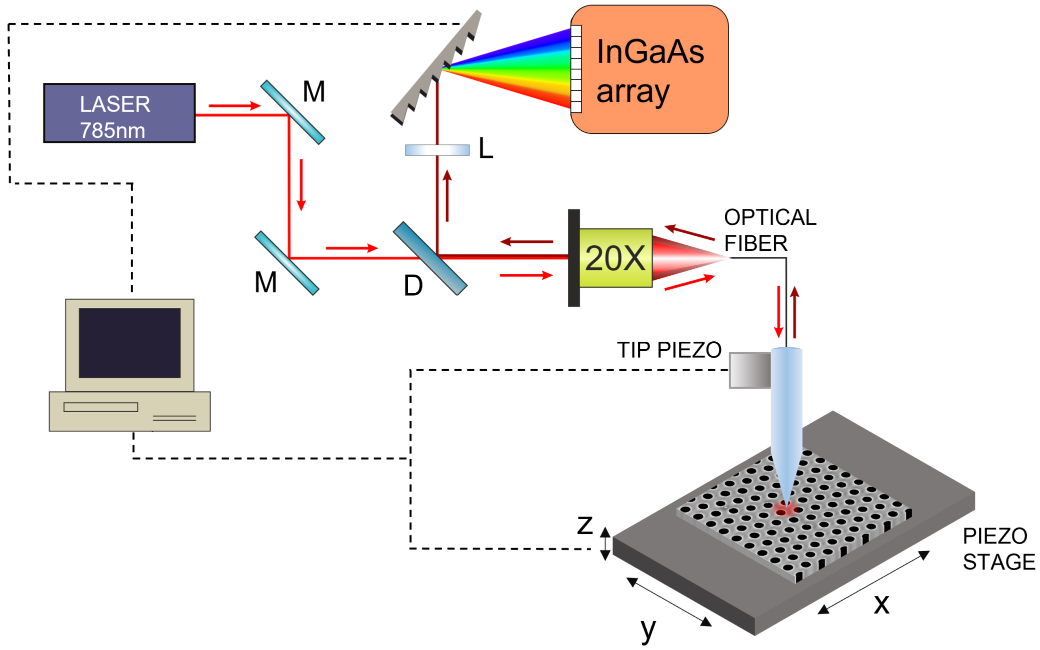

(b) COLLECTION CONFIGURATION

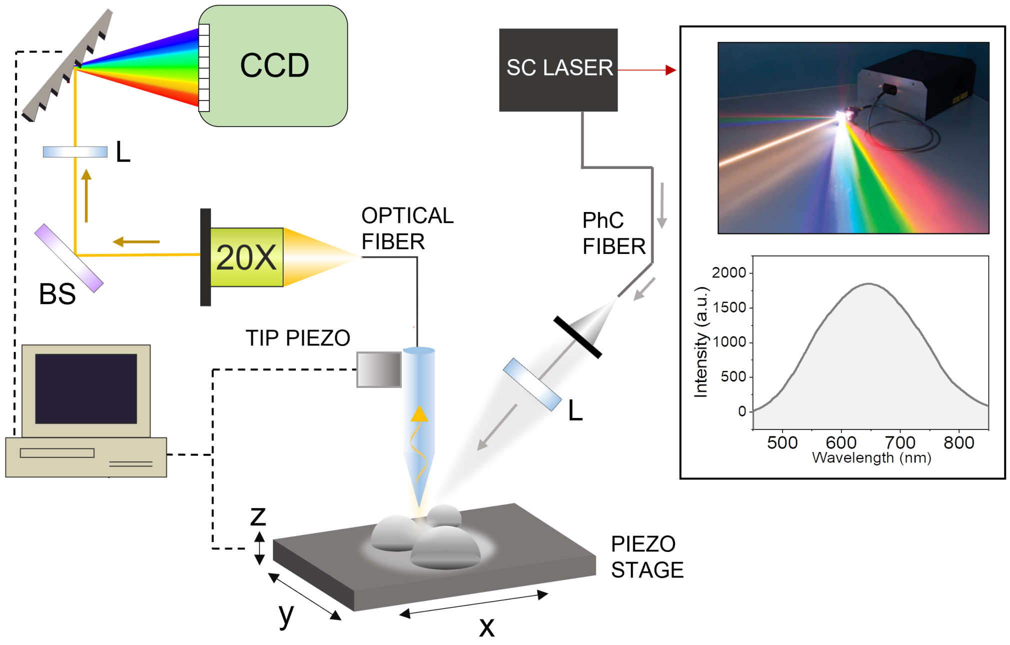

Figure 4.4. **(a)** Sketch of the illumination/collection SNOM setup arranged to detect photoluminescence signal. The excitation occurs through a diode laser emitting at 785 nm. The *M* label indicates mirrors, and *D* is a dichroic mirror (used for infrared detection) or a beam splitter *BS* (used for visible detection). The piezoelectric bimorph and scanning system are both driven by the same electronic central unit. **(b)** Collection configuration: the sample is illuminated laterally by a far-field Supercontinuum laser source tilted by the desired angle. The inset displays a picture of the laser and the emission spectrum.

> that will reflect the collected scattered light to the detector, and the optical fiber (of the near-field probe) that collects the scattered signal, is required to operate at 633nm. Finally, the InGaAs array is replaced by a liquid nitrogen-cooled CCD camera (by *Princeton Instruments*, equipped with 1340 x 400 pixels); the used diffraction grating is chosen as suitable for visible detection, hence it is the one with 150 lines/mm equipped with a 500 nm blaze, and the spectral dispersion becomes 0.42 nm/px.

The whole setup provides versatile ways of performing SNOM scannings on the samples under study; during a SNOM measurement, thanks to the presence of the piezoelectric stages, it is possible to scan large areas of the structures and simultaneously acquire optical information as well as morphological information on the sample surface (as shown in Fig.4.3c). Infact, while the sample is scanned, the SNOM computer sends at every step a trigger signal to the detector, that is forced to acquire the spectrum collected by the tip in an integration time opportunely chosen; of course, in order to synchronize the trigger with the detector, the velocity of the scan must be set up conveniently. Therefore, since at every tip position a spectrum is acquired, with a single scan it is possible to perform *hyperspectral Imaging*, a technique whose potentialities will be explored in the next chapters.

4.2 Dark-field spectroscopy

As explained in Section 2.2, one of the most reliable techniques that allow to characterize the far-field scattering features of Mie resonators is the Dark-Field microscopy, that directly detects scattering from a sample by rejecting the excitation light. As a result, the field around the specimen (i.e. where there is no specimen to scatter the illumination beam), is generally dark. This is in contrast with the most common usage of microscopes, that is the Bright-field configuration, in which the entire field of view is lighted (as sketched in Fig. 4.5a). Lord Faraday, in the late mid 1850s, was the first to scientifically examine the color of small gold particles, and he gained some impressive insight. A good 30 years later, Richard Zsigmondy also extensively studied the properties of nanoparticles [128], and was awarded the Nobel Prize in Chemistry in 1925 partly for his work on this topic. He developed ultra microscopy, which is called dark-field microscopy today. Lacking the possibilities to analyze the spectra as well as the shape and size of single particles through electron microscopy caused many of their experiments to be only of a qualitative nature. Dark-field microscopy was partly replaced by fluorescence microscopy but in recent years regained importance due to the growing interest in nano structures. There are several geometrical configurations thanks to which dark-field microscopy can be achieved, and in Fig.4.5b, c and d are resumed three of them. In the first one (Fig.4.5b), the sample is lighted from below the stage through transmission, and the incoming light beams (yellow arrows) impinges the sample with an angle θ that is greater than the numerical aperture NA of the objective, that in this way collect only the scattered light from the sample (blue arrow, pink cone). The second configuration is reported in Fig.4.5c, and implies the use of a (reflection or transmission) commercial dark-field objective; in this case, the incoming light passes through an opaque circular stop, and it the propagates through an external cylindrical shell sorround-

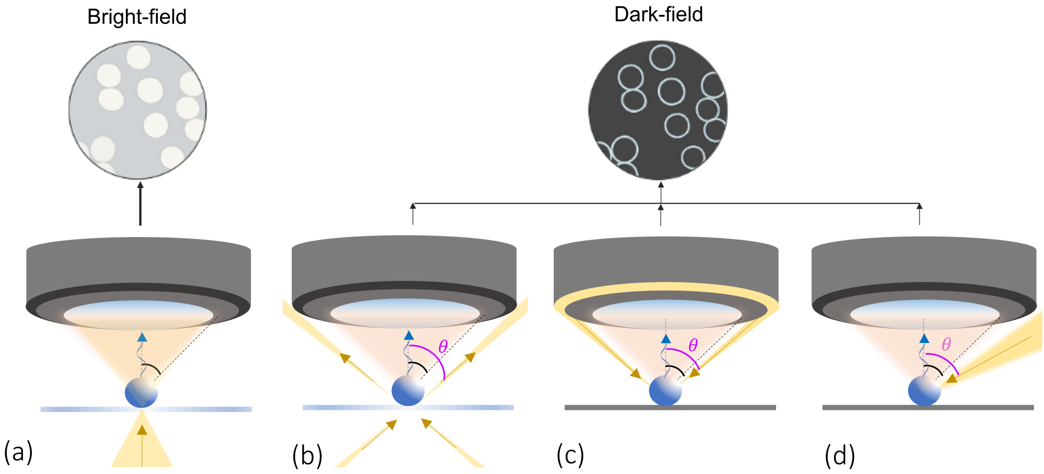

Figure 4.5. **(a)** Sketch of the bright-field configuration, in which the transmitted illumination (from the bottom) angular pattern is within the NA of the objective, hence it is detected along with the scattered signal. **(b)** Functioning of the first type of dark-field microscopy, through transmission; the illumination angle is greater than the objective NA. **(c)** Dark-field microscopy realized with the exploitation of a commercial assembled dark-field objective. **(d)** Dark-field microscopy achieved through lateral illumination, at an angle θ greater than the NA of a conventional microscope.

ing the objective lenses. This system therefore creates a cone of illumination of angular aperture θ greater than NA. Finally, dark-field microscopy can be realized in backscattering configuration with a conventional objective, as shown in Fig.4.5d, provided that the illuminating incidence of the source is at an angle greater with respect to NA. As explained in the previous section, the SNOM used in this work is assembled on a conventional optical microscope; during the development of this thesis, dark-field spectroscopy, in the configuration described in Fig.4.5d, was implemented in the set up. The final arrangement is shown in Fig.4.6; the custom-built branch of illumination is based on the $SC - Laser$ (see previous section for details), that after exiting from the photonic crystal fiber (PhC) and collimator, is focused on the sample with an achromatic lens L of 6 cm focal length, and can be tilted by the desired angle θ with respect to the axis perpendicular to the sample holder. The illumination spot is of the order of 10µm. The scattered light is collected by the objective, that is a 50X *Super Long Working Distance Plan* (SLMN Plan, *Olympus*) objective with a tubelens of 18 cm and numerical aperture $NA = 0.45$. Therefore, in order to achieve the dark-field regime, the illumination angle θ must be bigger than 27°. The scattered light, once collected by the objective, is then focalized on a multimode optical fiber of 10µm core with an achromatic lens of 6 cm focal length. The combination of the objective with the lens, determines the whole system to perform with an effective magnification of 17X (1/3 of 50X), and this leads to a collection spot of roughly ≈ 1 µm (considering white light). It is worth noticing that the collection fiber of 10 µm core acts as a spatial filter. At the other end of the fiber the scattered signal is extracted with a reflective collimator (RC) and then focalized with an achromatic lens of 10 cm focal length on the slit of a spectrometer (equipped with the 150 lines/mm grating with 500 nm blaze, chosen for its better

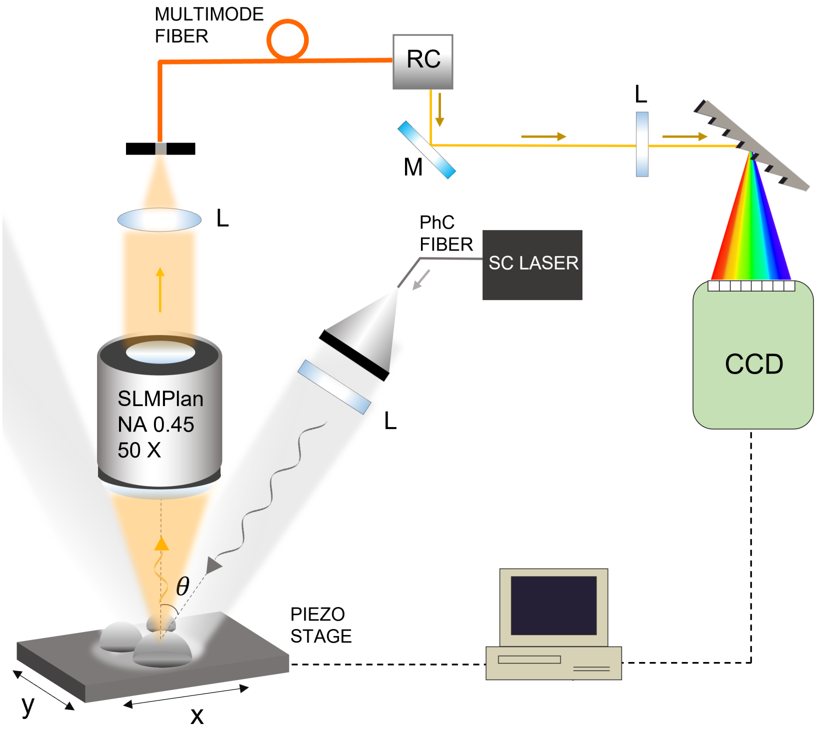

Figure 4.6. Sketch of the dark-field spectroscopy setup implemented on the SNOM conventional microscope. The dark-field condition is achieved by illuminating laterally at a tilted angle θ (with respect to the axis perpendicular to the sample) that is bigger than the numerical aperture of the objective.

performance in the visible range), where it is dispersed and finally detected by the CCD detector. Interestingly, thanks to the presence of the piezoelectric movements inside the sample holder, this setup also allow to perform optical scans thanks to which we can reconstruct dark-field hyperspectral maps; this new technique, in combination with the configuration of Fig.4.4b, was used to study the resonances of dielectric Mie resonators, and the obtained results will be presented in Chapter 5.

4.3 Computational Electromagnetics

Accurate analytic evaluation of the e.m. LDOS in complex photonic structures is a very difficult task; for this reason many numerical techniques have been developed in the last decades in order to provide useful tools not only to model nanostructures and compute approximated Maxwell's equations, but also to facilitate the interpretation of experimental data, or to approach aspects that are not accessible experimentally. *Computational Electromagnetics* has evolved in many forms and is the process of modeling the interaction of electromagnetic fields with physical objects and the environment. Several real-world electromagnetic problems like electromagnetic scattering, electromagnetic radiation, modeling of waveguides etc., are not analytically calculable, for the multitude of irregular geometries found in actual devices. Computational numerical techniques can overcome the inability to derive closed form solutions of Maxwell's equations under various constitutive relations of media, and boundary conditions. In this Section we present the two methods that have been used in order to obtain the results presented in this thesis (Chapter 5, 6 and 7.).

4.3.1 Finite Difference Time Domain

Finite Difference Time Domain (FDTD) method is used for modeling full-vector e.m. waves evolution in arbitrary structures by finding approximate solutions to the associated time-dependent Maxwell's equations over time in any specific positions [129]. FDTD algorithms involve both the discretization of the wave equations, by using second-order central-difference approximations to the space and time partial derivatives of the fields, and the meshing of the dielectric environment by a dense discrete rectangular grid. Each cell of the grid is characterized by its own electric permittivity and by the electric and magnetic field six components defined both in the center and at the edges of the unit-cell faces (Fig.4.7a). The temporal evolution of the fields is governed by the third and fourth Maxwell's Equations, that involve spatial and temporal derivatives:

$$\nabla \times \boldsymbol{E} = -\mu \frac{\partial \boldsymbol{H}}{\partial t} \qquad \nabla \times \boldsymbol{H} = \epsilon \frac{\partial \boldsymbol{E}}{\partial t} \tag{4.1}$$

Thanks to the temporal discretization these equations can be replaced with a system of finite difference algebraic equations through a *leapfrog* algorithm: the electric and magnetic field components are not solved in the same instant, but at a distance of a half temporal step. This makes the leapfrog algorithm a second order method: the difference between the exact solution and the approximated one grows with the square of the time sampling interval. A sketch of the logical passages of the algorithm can be found in Fig.4.7b. In every grid cell of the simulation, $\boldsymbol{E}$ ($\boldsymbol{H}$) components are updated according to the value they had at the previous temporal step and to the spatial variation of $\boldsymbol{H}$ ($\boldsymbol{E}$). Therefore, the updated electric field in time is dependent on the stored electric field and on the spatial variation of the magnetic field. The process is iterated for every field component, for the user defined number of temporal steps, until the desired transient or steady-state e.m. field is fully evolved. FDTD algorithms finally involve a Fourier-transform of the calculated time-varying fields to obtain the system spectral response: the electric and magnetic field spatial distributions at a given wavelength are therefore easily achieved, thus giving a direct estimation of both the electric and magnetic LDOS of the investigated structure. Typically, in any FDTD calculation extraordinary care must be taken in designing dielectric environment, light sources properties (dipoles, plane waves or Gaussian beams with defined polarization, wavelength, bandwidth, intensity and position. Infact, commercial softwares like *Lumerical* (used for the FDTD simulations presented in this thesis), offer a great versatility not only in the geometry of the studied structure, but also of the source itself, allowing a better comparison between the theoretical model and the more complex experimental enviroment. Analogously, attention must be payed in defining the actual "detectors",

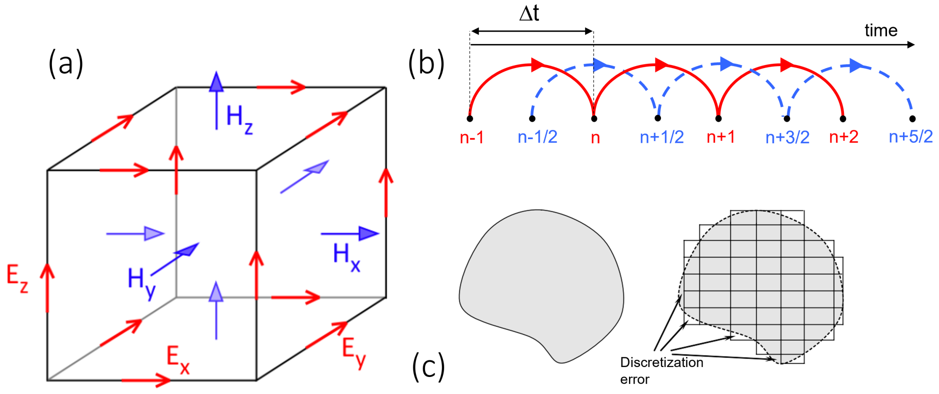

Figure 4.7. **(a)**Representation of the unit-cell mesh used for FDTD calculations and positions where the local electric and magnetic field components are typically evaluated. **(b)** Sketch of the time integration using a second-order finite-difference leapfrog integrator. **(c)** Irregular 2D domain (on the left), discretized with a rectangular mesh (on the right). Reprinted from [130]

which represent the positions whose fields are stored permanently in the calculator memory as a function of time. Since it is a time-domain method, FDTD solutions can simultaneously cover a wide frequency range. Moreover, the direct benefit in representing the field vectors in every cell, is to achieve LDOS distributions with a high spatial resolution, defined by the dimensions of the single cell, whose lower limit is given by the maximum memory that can be allocated in the calculator. On the other hand, the spectral resolution is bounded to the number of time-steps for which the fields evolve, hence it is limited both by the calculator memory and by the overall calculation time. Moreover, another limitation comes when the simulation of irregular shapes is requested; the use of the rectangle or parallelepiped as a basic finite element to discretize an irregular domain is certainly the simplest but not the most suitable choice, because an assembly of rectangles cannot accurately represent the arbitrary geometrical shape of the domain, and inevitably determine a discretization error (as represented in the sketch of Fig.4.7c).

4.3.2 Finite Element Method

A computational method that allows to overcome the limit of rectangular meshes, and therefore to model more complex structure, is the Finite Element Method (FEM). It is used to find approximate solutions of partial differential equations and integral equations. The solution approach is based either on eliminating the time derivatives completely (steady state problems), or rendering the partial differential equations into an equivalent ordinary differential equation, which is then solved using standard techniques such as finite difference. In other words, the FEM technique allows to solve boundary-value problems governed by differential equations (like Maxwell's equations) and a set of boundary conditions, just like in electromagnetic problems. The main idea behind the method is the representation of the

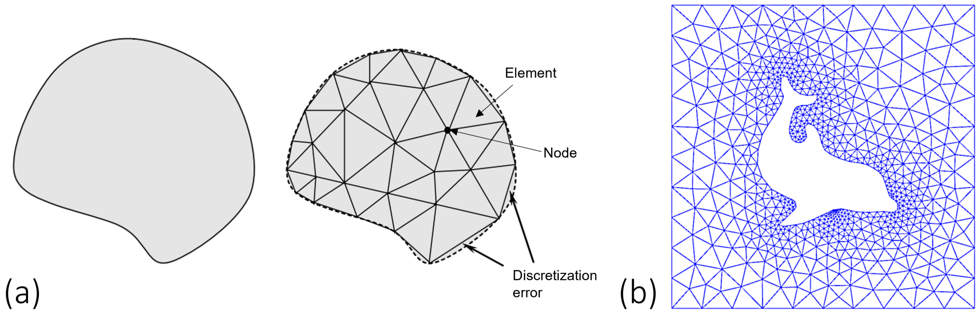

Figure 4.8. **(a)**Irregular 2D domain discretized with triangular elements. Reprinted from [130]. **(b)** Domain for flow around a dolphin showing a two-dimensional domain with a non-trivial geometry.

domain with smaller subdomains called the *finite elements*. These elements, i.e. the meshes, are typically triangular (in 2D) or tetrahedral (in 3D), and will approximate the structure inside the simulation domain with a minor discretization error with respect to rectangular meshes, as shown in Fig.4.8a. The points that connect the meshes are called *nodes*; the distribution of a *primary unknown quantity* (for example length, time, force, mass, temperature...) inside an element is interpolated based on the values at the nodes or the edges of the discretized domain. The interpolation or shape functions must be a complete set of polynomials. The accuracy of the solution depends, among other factors, on the order of these polynomials, which may be linear, quadratic, or higher order. The solution is obtained after solving a system of linear equations. To form such a linear system of equations, the governing differential equation and associated boundary conditions must first be converted to an integro-differential formulation either by minimizing a functional or using a weightedresidual method such as the Galerkin approach. This integro-differential formulation is applied to a single element and with the use of proper weight and interpolation functions the respective element equations are obtained. Finally, the assembly of all elements results in a global matrix system that represents the entire domain of the boundary-value problem. FEM method can be applied to many fields of physics, as it provides an easy way of dealing with complex geometries (Fig.4.8b); regarding the specific case of an electromagnetic problem, Maxwell's equations are turned into the *inhomogeneous scalar wave equation* form (*homogeneous* in the case of source-free problems), that are basically partial differential equations and therefore can be solved with the finite element procedure, imposing the tangential boundary conditions for the electric field [130]. One of the most sparking advantages of FEM methods for solving electromagnetic problems comes with operations at complex frequencies. Optical resonators, widely used in modern photonics, display a spectral response and temporal dynamics that are fundamentally driven by their natural resonances, the so-called quasinormal modes (QNMs), with complex frequencies. For optical resonators made of dispersive materials, the QNM computation requires solving a nonlinear eigenvalue problem. It was recently developed, in the work by Lalanne *et al* [131, 132] a formalism that leads to accurate QNM solvers for computing and normalizing the QNMs of micro- and nanoresonators made of highly dispersive materials. In simpler words, through FEM methods, by using the appropriate formalism, modes of resonators are computed by solving a standard linear eigenvalue problem derived in complex space from Maxwell's equations. Thus, a number of modes (the number is input by the user) is computed with a single computation without preconditioning. In this thesis, FEM simulations were performed with the commercial software *Comsol* in order to solve the eigenvalue problem of hyperuniform disordered photonic slabs, as will be explained in Chapter 6.

4.3.3 Boundary conditions

One of the most common and limiting aspects of numerical simulations, both FDTD and FEM, is that Maxwell's equations must be solved in a domain with finite dimensions. The simulation domain therefore must be terminated appropriately, in order to avoid artefacts in the final results, like for example reflection from the artificial borders. In many cases it is necessary to apply special boundary conditions, that determine the absorption of the radiation propagating towards the domain edges. However, the reflection of the e.m. radiation happens whenever translational invariance is broken; therefore, placing a generic absorbing medium at the borders of the simulation domain might imply the presence of artefact reflected radiation in the system. The solution for this issue was proposed by Berenger in 1994 [133], that showed how it is possible to build up a particular absorbing medium able to not generate reflection at its interface, no matter the wavelength or incidence angle of the radiation: the *Perfectly Matching Layer* (PML). The details on the functioning of PMLs is beyond the scope of this thesis; briefly, it is based on the fact that the radiative solutions of a wave equation (decomposable into $\phi(y,z)e^{ik_x x-\omega t}$, propagating in the x direction) are analytical functions of the position, and therefore can be extended continuously in the complex plane. In this sense, to place a PML of width w at a position $x = x_0$ means to add a non-zero imaginary part to the coordinate x. Therefore one obtains an evanescent wave for $x > x_0$ without modifying the solution in $x < x_0$ (Fig.4.9a); that is why the PML layer acts as absorber without generating reflection. The wave amplitude decreases exponentially for $x_0 < x < x_0+\mathrm{w}$, therefore the reflection at the PML terminal interface, further attenuated during the backward path of the radiation (towards x_0), can be neglected. Other types of boundary conditions exist, and they can be exploited in some cases in order to optimize the calculation process (reducing the computational time). For example, in systems that display symmetry properties like reflection invariance with respect to one or more planes, electromagnetic distributions have a defined parity; therefore it is possible to simulate a reduced region by imposing boundary conditions that take into account the symmetry of the problem. They are implemented by forcing the appropriate electromagnetic field components to zero. By forcing the simulation domain to terminate with a layer that is a *Perfect Magnetic Conductor* (PMC), or a *Perfect Electric Conductor* (PEC), respectively even or odd solutions with respect to the symmetry plane are obtainable. In the first (second) case, the tangential components of the magnetic (electric) field are deleted, as sketched in Fig.4.9b. Let's see how the imposition of these conditions allows to visualize modes

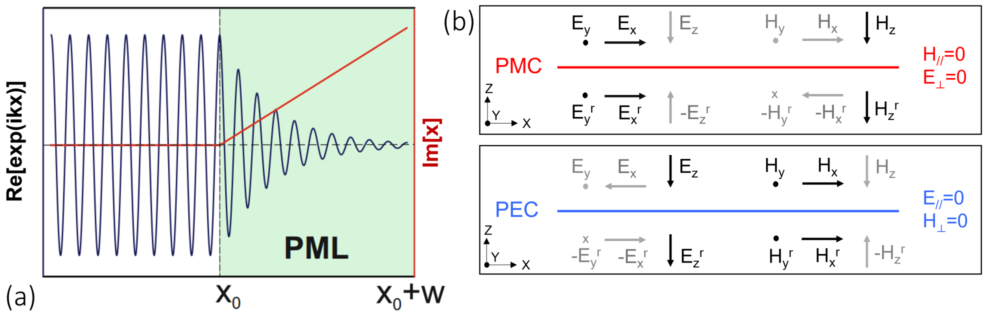

Figure 4.9. **(a)** Illustration of the functioning of a Perfectly Matching Layer of width w: for $x < x_0+w$ the coordinate x acquire a an imaginary component that determines the decay in amplitude of the incident signal, without generating reflections in the simulation domain $x < x_0$. Reprinted from [134]. **(b)** Fields components in presence of a PMC (red) and PEC (blue) condition: PMC (PEC) condition preserve the field components that are even (odd) with respect to the plane $z = 0$. The deleted components are labelled in grey.

with defined parity. Let's suppose for example that the simulation domain is terminated with a $z = 0$ plane, and that PMC conditions are imposed on it. Then we have $H_x(x, y, 0) = H_y(x, y, 0) = 0$ and hence $E_z(x, y, 0) = 0$. The components that are not under boundaries are exactly the ones that display unchanged sign for a reflection with respect to $z = 0$. On the other hand, a generic photonic mode, in order to be odd must satisfy the conditions $E_x = E_y = H_z$ in every point of the plane $z = 0$. Therefore, to impose a PMC condition means to require every component of the electromagnetic field to be zero on a surface of the considered system, i.e. the only accectable solution is the null one. By imposing PMC conditions, and rejecting the trivial solution, the only modes that are allowed are the even modes for reflection with respect to $z = 0$. Analogously, the same reasoning leads to the results that PEC conditions determine odd solutions.

Chapter 5

Sub-wavelength Hyperspectral Imaging of dielectric Mie resonators

All-dielectric, sub-micrometric particles have been successfully exploited for light management in a plethora of applications at visible and near-infrared frequency. In recent studies the Mie scattering of light has emerged also as a crucial phenomenon at the base of bandgap formation in complex photonic structures: before focusing on this novel aspect of photonics, to which Chapter 6 will be dedicated, we address a full optical characterization of dielectric Mie resonators realized through solid state dewetting, both in the near-field and in the far-field. Much of the recent research on Mie resonators has been achieved with experiments reporting mainly far-field measurements, and the investigation of the intricacies of the Mie resonances at the sub-wavelength scale has been hampered by the limitation of near-field methods, focusing only on low order multipolar terms. After providing a brief description of the samples studied in this Chapter in Section 5.1, we address spatial and spectral mapping of multi-polar modes of a dielectric island by Near-field hyper-spectral imaging corroborated with FDTD simulations (Section 5.2). The simultaneous detection of several resonant modes allows to clarify the role of substrate and incidence angle of the impinging light, highlighting spectral splitting of the quadrupolar mode and resulting in different spatial features of the field intensity. Then, in Section 5.3, we show how the implementation of Dark-field scanning microscopy by exploiting the scanning stages of the SNOM setup can bring interesting detection features. We describe how it allows a complete characterization of the beam steering properties of nanoscatterers by means of a novel way of managing the dark-field technique, achieving hyper spectral imaging by means of Dark-field scanning microscopy.

5.1 Studied samples

The investigated samples consist in monocrystalline Si-based islands fabricated via assisted solid state dewetting, and were realized by the teams of the Aix Marseille Universitè (France) and Institute of Photonic and Nanotecnology (Italy). As we have seen in Section 2.3, the strength of this fabrication technique relies on a fast process that does not depend on the size of the sample, but only on the dewetting speed. However, in order to produce organized patterns it must be assisted by Photolithography or Electron Beam Lithography (EBL) followed by Plasma Ion Etching. In Fig.5.1a are shown the main three steps through which the samples were fabricated. The followed protocol is based on the instability of ultrathin Si-based films (Si or SiGe 20%, typically less than 30 nm thick) on a SiO_2/Si substrate when annealed at high temperatures (750-880 °C) in a high-vacuum chamber (10^{-8}–10^{-10} Torr). The multilayer structure (Si-based film, SiO_2 substrate of thickness t, and Si bulk) (step (1) of Fig.5.1a), is patterned with lithographic methods using the proper resist masks (step (2) of Fig.5.1a). Details on this step of the procedure can be found respectively in [40] for Photolithography and [64] for EBL.

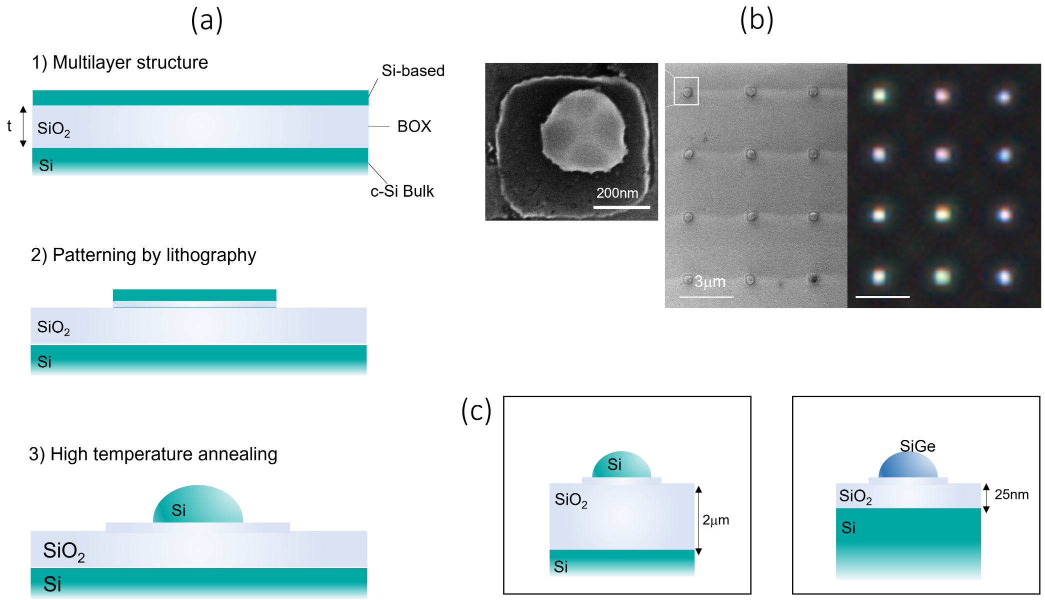

Figure 5.1. **(a)** Scheme of the main fabrication steps. 1) Multilayer starting structure: thin monocrystalline Si-based layer (less than 30 nm) on a silicon oxide (buried oxide, BOX) SiO_2 layer of thickness t, placed on a Si bulk. 2) Patterning process through lithography (EBL or Optical). 3) High temperature annealing in ultra-high vacuum. **(b)** SEM image top view of an ordered pattern of dewetted island, next to the dark-field microscope image; in the left inset, a zoom of a single island is displayed. **(c)** Sketches of the two samples analyzed in this work; a Si island sitting on a 2 μm thick SiO_2 layer on the left, and SiGe 20% (Ge at 20%) island on a 25nm SiO_2 layer on the right.

Then, the samples are transferred in the high vacuum of the molecular beam epitaxy chamber for the annealing and dewetting processes (step (3) of Fig.5.1a). The annealing process is carried out in two stages: the first one is an in-situ cleaning where the temperature is risen at about 650 °C for 30 minutes in order to remove

any residual native oxide from the surface of the sample.
The second annealing step induces the solid-state dewetting of the thin Si-based layer when the temperature is increased at about 750 °C for 30 minutes. The sample finally evolve toward truncated pyramidal nanocrystals. In Fig.5.1b is shown the SEM image top view of an ordered pattern of dewetted island, next to the dark-field microscope image, in which different structural colors can be observed. In the left inset, a zoom of a single island is displayed, where the surface facets are clearly visible; infact, once the islands are formed, the isolated nanocrystals exhibit a faceted shape with the onset of the low-energy facets: (111), (113) and (001) [40]. In this thesis, two samples of Si-based dewetted island were analyzed, as shown in Fig.5.1c, that differ for the composition of the top Si-based layer and the SiO_2 thickness. The left inset display Si island sitting on a 2 µm thick SiO_2 layer, while the right inset shows a SiGe 20% (Ge at 20%) island on a 25nm SiO_2 layer. The results obtained on these two samples, that were fabricated with solid state dewetting assisted respectively by Photolithography and EBL, will be discussed respectively in Section 5.2 and 5.3.

5.2 Near-field Hyperspectral Imaging of Resonant Mie Modes in a Dielectric Island

As explained in Chapter 2, Mie resonators have emerged in the last decade as promising building blocks for optoelectronic devices, since they provide the possibility to efficiently redirect and concentrate light with low absorption losses [23]. In Section 2.1 it was shown that the optical modes in high-index dielectric nanoparticles originate from the excitation of optically induced displacement currents, and can be both magnetic and electric in nature. The combination of these two kinds of resonant modes and the exploitation of higher order multipolar modes offer opportunities for directional and polarization controlled emission from nanoemitters [34, 135, 136, 137, 138]. Moreover, in the field of light-matter interaction, high refractive index dielectric nanoparticles have recently been considered as a possible alternative to metallic nanoparticles for generating localized optical resonances down to nanoscale. In fact, the concentration of light in subwavelength hot spots represents an essential element for surface enhanced fluorescence [139] and for manipulating the generation of nonclassical light by quantum emitters [140]. For these purposes, a complete knowledge of the electric and magnetic nature of the modes, their spectral features and their spatial distribution is mandatory. Finite Difference Time Domain (FDTD) numerical calculations represent a powerful tool to systematically study the resonant properties of high-index dielectric particles [24, 36, 141, ?]. On the other hand, the direct experimental characterization of these peculiarities has almost exclusively dealt with far-field measurements [27, 47], that do not provide access to the spatial distribution of light modes. Sub-wavelength, spatial resolution imaging has been realized in the past by cathodoluminescence imaging spectroscopy [52] or apertureless (scattering type) near-field scanning optical microscopy [51, 142, 143]. However, these methods are either limited to the collection of the signal in dielectric regions, i.e. only in the small area covered by the sub-wavelength sized Mie resonators [52], or do not provide information on more than one optical mode at a time (typically Mie multipolar terms of lower order), owing to the use of a laser at a fixed frequency [51], thus disregarding also essential aspects of the compresence of spectral and spatial features of the investigated structures, and losing information on higher order multipolar resonances. Here, we present via *Near-field hyperspectral imaging* (HSI), a detailed sub-wavelength optical characterization of the multipolar resonances formed in a monocrystalline silicon island, providing simultaneously spectral and spatial information on several resonances in a single measurement. Experimental results are explained and validated by FDTD simulations. Exploiting the etalon effect springing from the thick SiO_2 layer between the antenna and the bulk Si substrate underneath, we detect the splitting of one resonance into sharper peaks, unrevealing the difference and intimate features of their near-field details. We thus achieve a complete understanding of the effect of the substrate on the resonant modes, filling a gap in a research field that so far has considered the presence of the substrate mostly as a strong limitation of the Mie resonators properties. We also show that intensity and spatial light localization in the near-field, strongly depend on the illumination angle, clarifying the crucial role of the excitation configuration that can be exploited as a spatial tuning tool to engineer the coupling between nanoantennas and emitters, by controlling the absorption of the emitter itself.

5.2.1 Experiment

The samples investigated in this work are the ones sketched in Fig.5.1d, and consist in monocrystalline Si-based islands fabricated via low-resolution optical lithography and plasma etching followed by solid state dewetting [61, 18, 65, 40]. A 2 µm thick layer of SiO_2 separates the islands from an underlying bulk Si substrate. In Fig.5.2a we report a top view Scanning Electron Microscopy (SEM) image of the sample showing an ordered array of several dewetted islands. Islands with different diameters can be fabricated, but here we focus on a single example of scatterer of small diameter ($d \approx 330$ nm), like the one shown in Fig.5.2b.The SNOM was used in *collection* configuration (see Section 4.1.2) in order to detect the near-field scattered emission of the single island under a tilted illumination configuration (as shown in the sketch of Fig.5.2c). The spatially-resolved optical maps were recorded by scanning the probe dielectric tip over the sample at a fixed distance (few tens of nm). The illumination source, tilted of an angle $\theta = 30°$ with respect to the perpendicular axis of the scatterer, is a Super-continuum laser, whose scattering spectrum, collected with the cooled Si-based CCD camera used in the experiment, is reported in Fig.5.2d. The complete setup is described in Section 4.1.2, and represented in the second panel of Fig.4.4. As explained before, at every tip position, the entire spectrum of the sample is collected with a spectral resolution of 0.42 nm. The whole technique allows to perform HSI by collecting a full near-field spectrum at every tip position of the spatial map.

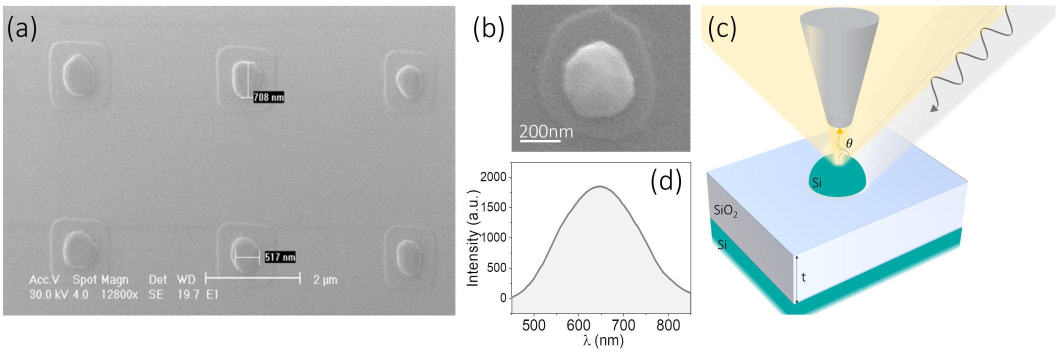

Figure 5.2. **(a)** SEM image of an ordered array of Si dewetted islands obtained via low-resolution Photolithography. **(b)** SEM image of a single island of diameter $d \approx 330$ nm. **(c)** Sketch of the experimental set up: the tilted illumination (of an angle θ with respect to the axis perpendicular to the sample) from the Supercontinuum is scattered by the island. The yellow cone is a representation of the angular pattern of scattering. The scattered light is collected by the near-field tip at a distance of $\approx$ 10 nm. **(d)** Emission spectrum of the Supercontinuum illumination source detected by the Si-based CCD camera.

5.2.2 Theoretical simulations: modes evolution with substrate and angle of illumination

We study the modification on the scattering spectra of a single Si-based scatterer as a function of the thickness t of the SiO_2 substrate and of the illumination angle θ by means of FDTD simulations (whose principle of functioning is described in Section 4.3.1) with the commercial software Lumerical. We consider a hemispherical Si island of diameter $d = 330$ nm (Fig.5.3a), illuminated by a Total Field Scattered Field (TFSF) source, which launches a broad-band (λ = 400-1200 nm) plane wave from the top, and filters out all the light that has not been scattered. The simulated source is polarized along the x axis, and can be tilted by an angle θ with respect to the z axis. Power transmission monitors are positioned around the TFSF source in order to obtain the total scattering cross section, and two field monitors intersect the particle (along the xz and yz plane) to monitor the local field intensity. An additional monitor is placed on top of the island in the xy plane at a distance of 10 nm from the apex in order to simulate the near-field spatial profile of the electric field intensity. Perfectly Matching Layers (PMLs) are used to prevent unphysical scattering from the simulation boundaries and to mimic semi-infinite substrates (see Section 4.9). Optical constants for Si and SiO_2 are taken from Palik [144]. Fig.5.3b reports the total scattering cross sections of the Si hemisphere, illuminated under normal incidence, for different values of the substrate thickness t. In particular, it is possible to follow the evolution of the modes from the case of the island in air (yellow spectrum), to the configuration with the maximal SiO_2 thickness of 2 µm (blue spectrum). The latter is the actual value of t in the experimentally investigated sample. The scattering cross sections for three selected values of t (i.e. t = 25 nm, 500 nm and 1300 nm), are reported in Fig.5.3b, in orange, magenta and purple, respectively. The identification of these modes (electric hexapole EH, magnetic

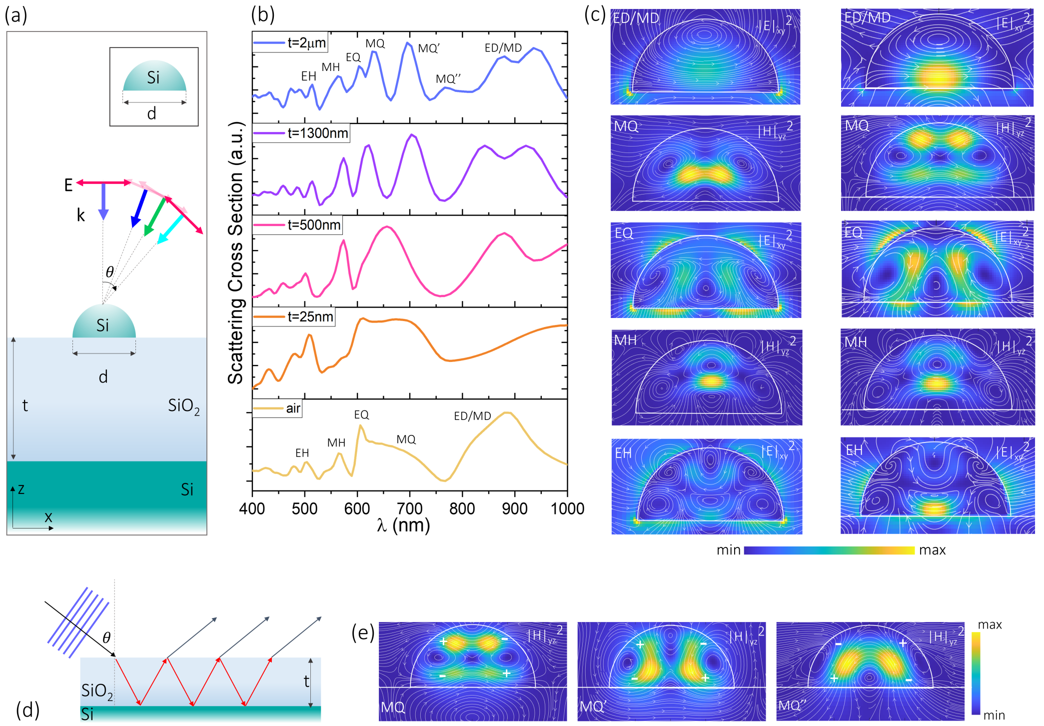

Figure 5.3. **(a)** Sketch of the model used in the FDTD simulations; a Si hemisphere of diameter d atop a SiO_2 layer of thickness t, and a bulk Si substrate. The scatterer is illuminated by an x polarized TFSF source that can be tilted by an angle θ with respect to the z axis. Inset: bare case of the island in air. **(b)** Scattering cross sections at θ=0° (from bottom to top) for increasing values of t, $t = 0$ nm (island in air), $t = 25$ nm, 500 nm and 1300 nm. **(c)** *Left column*: vertical crosscuts of the electromagnetic field intensity and current loops (represented by white arrows) of the multipolar resonances of the hemisphere in air. The maps, acquired at the wavelengths of the yellow spectrum, from top to bottom in order of increasing energy are: ED/MD ($\lambda = 800$ nm), MQ ($\lambda = 660$ nm), EQ ($\lambda = 605$ nm), MH ($\lambda = 570$ nm) and EH ($\lambda = 504$ nm). *Right column*: analogue maps of the hemisphere on a SiO_2 layer with $t = 2$ μm. The maps, acquired at the wavelengths of the blue spectrum, from top to bottom are: ED/MD ($\lambda = 770$ nm), MQ ($\lambda = 628$ nm), EQ ($\lambda = 603$ nm), MH ($\lambda = 563$ nm) and EH ($\lambda = 514$ nm). **(d)** Sketch of the etalon effect: light impinges the SiO_2 substrate and experience effects of constructive and destructive interference, whose results are redirected towards the upper plane by refraction at the interface SiO_2/air. **(e)** Crosscuts of $|H_{yz}|^2$ and current loops of the triple magnetic quadrupole resonances in the case of SiO_2 layer t=2 μm thick. Respectively MQ, MQ' and MQ" at $\lambda = 628$ nm, 695 nm and 766 nm. The poles are labeled with + and − signs. MQ" poles are of inverted signs with respect to MQ and MQ'.

hexapole MH, electric quadrupole EQ, magnetic quadrupole MQ and electric and magnetic dipole ED/MD) is based on their field intensity profile inside the particle and the corresponding current loops (left column of Fig.5.3c). First, electric and magnetic field intensity inside the hemisphere suspended in air allow to identify the multipolar resonances, from the fundamental to higher-energy ones. In the near-field, the electric (magnetic) field profiles in the xz (yz) plane for electric (magnetic) resonances show bright lobes inside, related to the poles generated by current loops (white arrows in Fig.5.3c). Effects of symmetry breaking with respect to the ideal case of a sphere in air (in which ED and MD are easily distinguishable) must be considered [145, 146] and are beyond the scope of this paper. We therefore refer to the broad band centered around 900 nm as ED/MD. We also identify the main higher-order resonances as MQ, EQ, MH and EH, of which we report the vertical crosscuts of E or H respectively at $\lambda = 660$ nm, 605 nm, 570 nm and 504 nm. The same reasoning was adapted to assign the resonances of the particle sitting atop a SiO_2 substrate while t increases. As explained in Section 2.1.2, it was recently shown ([24, 40]) that by increasing t, constructive and destructive interference of the incident light reflected from the SiO_2/Si-bulk interface arises, resulting into strong variations in the driving field of the resonator. A schematic sketch of the interference effect that arises in the substrate, called etalon effect, is represented in Fig.5.3d. The Mie scattering efficiently out-couples the light interfering in the etalon and re-directs light at smaller angles with respect to the incident beam. From this combination structural colors spring, covering the full visible spectrum with resonances with a high intensity contrast between maxima and minima. However, a detailed identification of the actual physical origin of these sharp peaks has never been attempted so far. While increasing t, we can follow the evolution of the vertical profiles of the electric (magnetic) field intensity along the xz (yz) plane of the main electric (magnetic) resonances in the scatterer (right column of Fig.5.3c for the main resonances of the blue spectrum on top of Fig.5.3b, corresponding to the nominal SiO_2 thickness $t = 2$µm). Specifically, the maps of ED/MD, MQ, EQ, MH and EH correspond to $\lambda = 770$ nm, 628 nm, 603 nm, 563 nm and 514 nm, respectively. The original broad band corresponding to MQ in the yellow spectrum (scatterer in air) splits into three sharp peaks, all identifiable as magnetic quadrupole resonances from the analyzed current loops, to which we refer as MQ, MQ' and MQ". This is clear by looking at Fig.5.3e, where the vertical crosscuts of the magnetic field intensity and current loops of the triplet $\lambda = 628$ nm, 695 nm and 766 nm are shown: the three insets display analogue features, like the presence of the four poles in the current loop, labelled with $+$ and $-$ signs, corresponding to current flowing respectively out and in the scatterer [24], and can therefore be identified as resonances of magnetic quadrupole nature, MQ, MQ' and MQ". The coupling between the scatterer and the interference arising from the SiO_2 layer, combined with the analysis of crosscuts of the electric/magnetic field for every peak, therefore allows to identify the modes and obtain information about the multipole characteristics of the island spectrum without any needs of multipolar decomposition [51].

An analogue method of identification is used in order to monitor the changes in the scattering properties of the island with respect to the angle of illumination (Fig.5.4a). We compute the FDTD scattering cross sections of a Si hemisphere for $t = 2$ µm layer of SiO_2 and Si bulk for different angles of illumination θ: the spectra

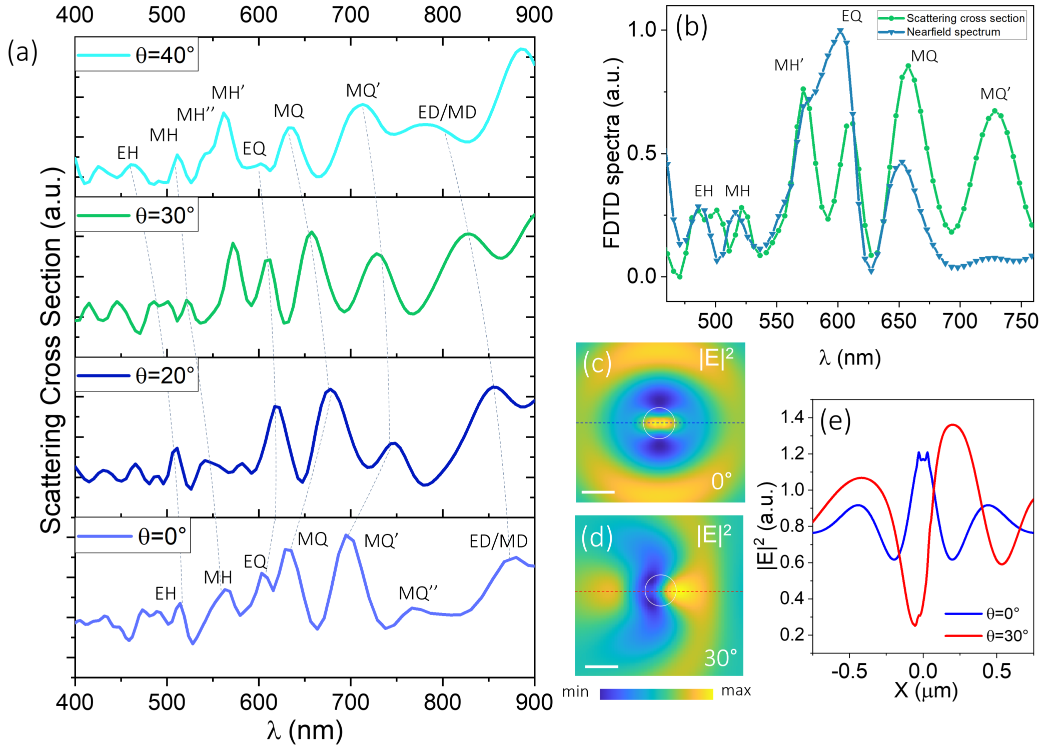

Figure 5.4. **(a)** FDTD scattering cross sections for different angles of illumination, from bottom to top: $\theta = 0°$ in blue, $\theta = 20°$ in dark blue, $\theta = 30°$ in green and $\theta = 40°$ in cyan. **(b)** FDTD scattering cross section in green and FDTD near-field spectrum, in dark green, acquired on the center of a field monitor at a distance of 10nm from the hemisphere surface for $\theta = 30°$. The peaks are labelled according to the identification of the multipolar resonances under tilted illumination EH, MH, MH', EQ, MQ and MQ'. **(c)**, **(d)**: Near-field FDTD spatial distribution of the electric field intensity of MQ for $\theta = 0°$ and $\theta = 30°$. The white scale bar corresponds to 200nm. **(e)** Horizontal cuts of the near-field $|E|^2$ along the dashed blue (red) dashed lines displayed in **(c)** and **(d)**.

are displayed in blue for $\theta = 0°$, in dark blue for $\theta = 20°$, in green for $\theta = 30°$ and in cyan for $\theta = 40°$. The peaks arising from the coupling of the Mie modes with the etalon are sensible to the angle of illumination this is different with respect to the scattering cross section of the island on a thin substrate (Fig.5.5a), that results practically unchanged for different θ, as shown in Fig.5.5b. Differently, in the case of thick SiO_2 layer, the broad MH and MQ peaks split due to interference with the etaloning resonances, in which the angle of incidence plays a fundamental role. Specifically, for $\theta = 30°$, a second MH appears around λ =576 nm (that we call MH'), and one of the three MQs is suppressed, leaving only MQ and MQ' at λ =657 nm and λ =725 nm. We now focus on the scattering in near-field; in Fig.5.4b we report in dark green the FDTD near-field spectrum acquired at the center of the island for $\theta = 30°$, and the calculated scattering cross section for the same angle of illumination. The two spectra display almost the same resonances but with different relative weights of the peaks; in the near-field, the peaks MH' and EQ broaden and as a consequence they tend to overlap. Provided the high sensitivity of the Mie

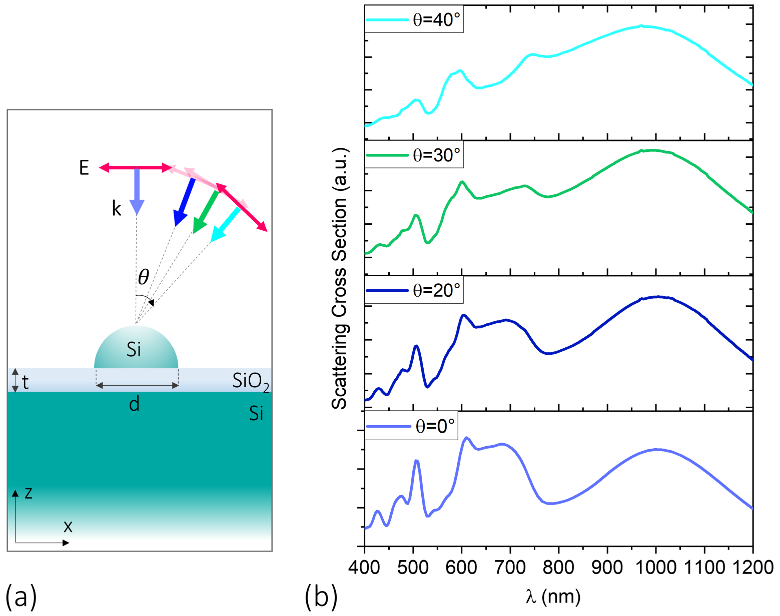

Figure 5.5. **(a)** Sketch of the model used in the FDTD simulations; a Si hemisphere of diameter d=330nm is positioned atop a SiO$_2$ layer of thickness t =25 nm, and a Si-bulk substrate. The scatterer is illuminated by an x polarized TFSF source that can be tilted by an angle theta with respect to the z axis. **(b)** FDTD scattering cross sections for different angles of illumination, from bottom to top: $\theta = 0°$ in yellow, $\theta = 20°$ in light green, $\theta = 30°$ in dark green and $\theta = 40°$ in blue.

resonances to large values of t, we analyze the near-field spatial profile of the electric field intensity, achieving a full comprehension of the scatterer's responses in such a specific configuration. The near-field distributions of the resonances are strongly affected by the illumination direction. In Fig.5.4c and d are shown the near-field FDTD maps of the electric field intensity of the MQ' mode generated under normal incidence (0°) and tilted incidence (30°), respectively. In the latter case, the electric field intensity is not symmetrically distributed around the scatterer, and we clearly observe that the hotspot changes its shape and spatially shifts to the right. The shift is of about 250 nm, as highlighted by Fig.5.4e, where the horizontal cross cuts through the center of the maps are compared (respectively in blue and red). These cross cuts show that also the maximum electric field intensity is influenced by the illumination angle. Fig.5.4c-e show that by changing the illumination angle by 30° on the left half of the Si-island the signal intensity drops from bright to dark, while in the region around the right border of the island we observe a net increase of the electric field intensity.

5.2.3 Near-field Hyperspectral Imaging Experiment

In the following, we provide a detailed near-field HSI analysis of the higher order multipolar modes in a single all-dielectric nanoparticle. Generally, in a SNOM experiment, before addressing high-resolution scans on the desired structure (in this case a single island in a collective ordered pattern), a broad investigative measurement is performed. In this specific case it is important to show this technical part of the experiment because it is essential for understanding the normalization of the signal. In Fig.5.6a we report a 10 µm × 6 µm SNOM scan (with 100 nm/px spatial step) obtained by collecting in the near-field the scattered spectrum of an array of islands under the illumination of a super-continuum source tilted by 30°. The

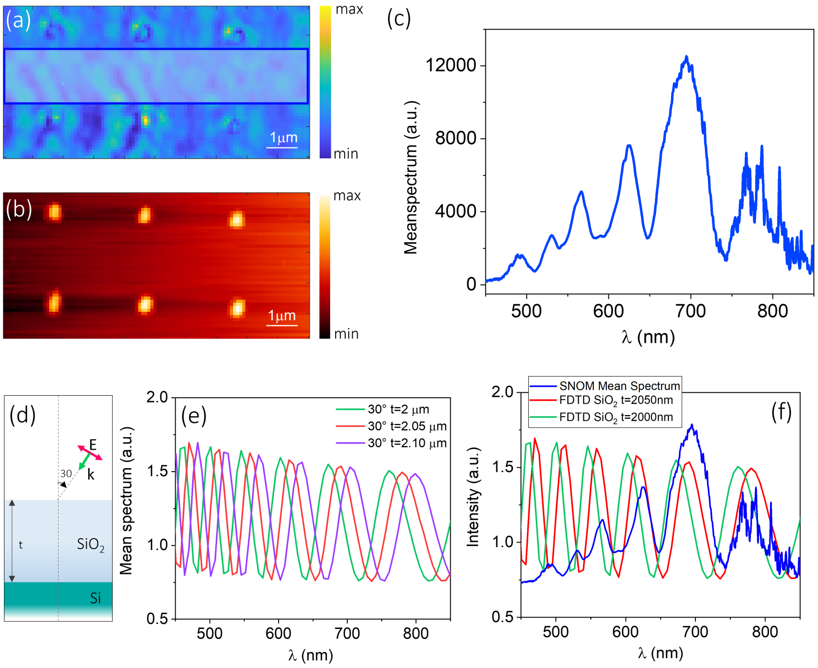

Figure 5.6. **(a)** SNOM optical map filtered around a broad wavelength range (400 nm-900 nm), acquired on a 10µm × 6µm region with 100 nm spatial step. **(b)** SNOM topography acquired simultaneously during the scan, in which six ordered dewetted island are visible. The scalebar is relative to the height of the sample. **(c)** Spectrum obtained by mediating in the blue rectangular area (represented in **(a)**); the area was chosen by excluding the islands, so that the mean spectrum can be considered as the background signal used to normalize the spectra of the islands. **(d)** Sketch of the multilayer structure without island, i.e. the slab illuminated by a wave tilted by 30°. **(e)** FDTD Near-field spectra for different values of SiO_2 thickness t, $t = 2$ µm (nominal), $t = 2.05$ µm and $t = 2.1$ µm. **(f)** SNOM normalization spectrum (in blue) with the FDTD near-field spectra for the case of $t = 2$ µm (nominal, in green) and $t = 2.05$ µm (in red).

topography simultaneously acquired during the scan is reported in Fig.5.6b, where six islands are clearly visible. As it can be observed in the optical map, a strong signal is present in the area between islands; the mean spectrum, averaged over the blue area (carefully chosen far from the islands) sketched on the map of Fig.5.6a, is reported in Fig.5.6c. Several peaks due to the etalon effect can be observed, and infact we attribute this signal to the interference arising from the etalon after illumination. In order to clarify the role of the etalon phenomenon in the discrepancy between experimental and theoretical data later on presented, we performed FDTD simulations on the $t = 2$ µm SiO_2 slab (without nanoantenna on top) on Si bulk (sketch in Fig.5.6d); in 5.6e we report the trend of the FDTD near-field spectrum of the multilayer structure for three values of t. As expected, from this graph we see how the spectral position of the etalon peaks are strongly affected by variations of t (roughly a 15 nm shift for a variation Δt =50 nm). This is important, because in the fabricated samples there might be some residual Si and intermixing of Si with the underlying SiO_2 resulting from the high temperature annealing [147] producing a strong scattering from the areas nearby the island; this Si interdiffusion in the SiO_2 layer can be schematized with an effective slightly thicker SiO_2 substrate with respect to the nominal value of $t = 2$µm, that can affect the etalon peaks position, as proven by the FDTD simulations of Fig.5.6e. Therefore, slight deviations from the nominal t and the actual fabricated SiO_2 layer can also explain spectral shifts between theory and experiment. This can be seen in Fig.5.6f, where we compare the SNOM normalization spectrum (in blue) with the FDTD near-field spectra for the case of $t = 2$ µm (nominal, in green) and $t = 2.05$ µm (in red), for which an even better agreement is achieved. However, the fairly good match between the blue (SNOM) and green (nominal FDTD $t = 2$ µm) spectra is a further confirmation of what is stated in the paper by van de Groep *et al* [24], where it is theoretically shown that constructive and destructive interference of the incident light reflected from the SiO_2 layer, result in strong variations in the driving field in the resonator. For these reasons, the mean spectrum evaluated over the blue rectangular area, corresponding to the etalon effect, is here used as the normalization spectrum, i.e. the recorded near-field spectrum on the single island is divided by the mean spectrum reported in Fig.5.6c. The used normalization technique does not comprehend a preliminary subtraction of the etalon spectrum (before further dividing the resulting signal by it) because of the spatial homogeneity of the periodic signal that exists also without the island. We now move to the final analysis, selecting inside the dewetted pattern an island with diameter $d \approx 330$ nm. Fig.5.7 summarizes the results of a 1.6 µm × 1.2 µm SNOM scan on a Si dewetted island of diameter $d = 330$ nm, under the illumination of a super-continuum source tilted by 30°. The scan step is 50 nm/pixel, and the sub-wavelength spatial resolution of about 200 nm is related with the dimensions of the tip. The normalized near-field spectrum (in purple) collected at the apex of the island is reported in Fig.5.7a, together with the FDTD near-field spectrum acquired at the center of the near-field monitor (in dark green). Theoretical and experimental spectra are in good agreement, allowing to identify, in order of decreasing energy, the main high-order multipolar resonances that result from the resonant modes of the antenna with the etalon effect, from EH to MQ'. In agreement with the previous assessment of scattering cross-section and near-field spectrum for $\theta = 30°$ shown in FDTD simulations where the two peaks MH' and EQ spectrally overlap (Fig.5.4b), the experimental SNOM near-field spectrum at those wavelengths displays a single peak, dominated by the contribution of the EQ resonance (Fig.5.7a). Exploiting our HSI technique, we provide the experimental near-field spatial profiles represented in the maps of Fig.5.7b, that are obtained by plotting the intensity integrated around the main peaks in the purple spectrum of Fig.5.7a ($\lambda = 490$ nm (EH), $\lambda = 530$ nm (MH), $\lambda = 570$ nm (EQ), $\lambda = 645$ nm (MQ) and $\lambda = 735$ nm (MQ')).

During a SNOM scan, scattering spectra and morphology of the sample are simultaneously acquired. Thus, we can overlap optical and morphological maps (the island is highlighted by white circles in Fig.5.7b) and directly compare them with simu-

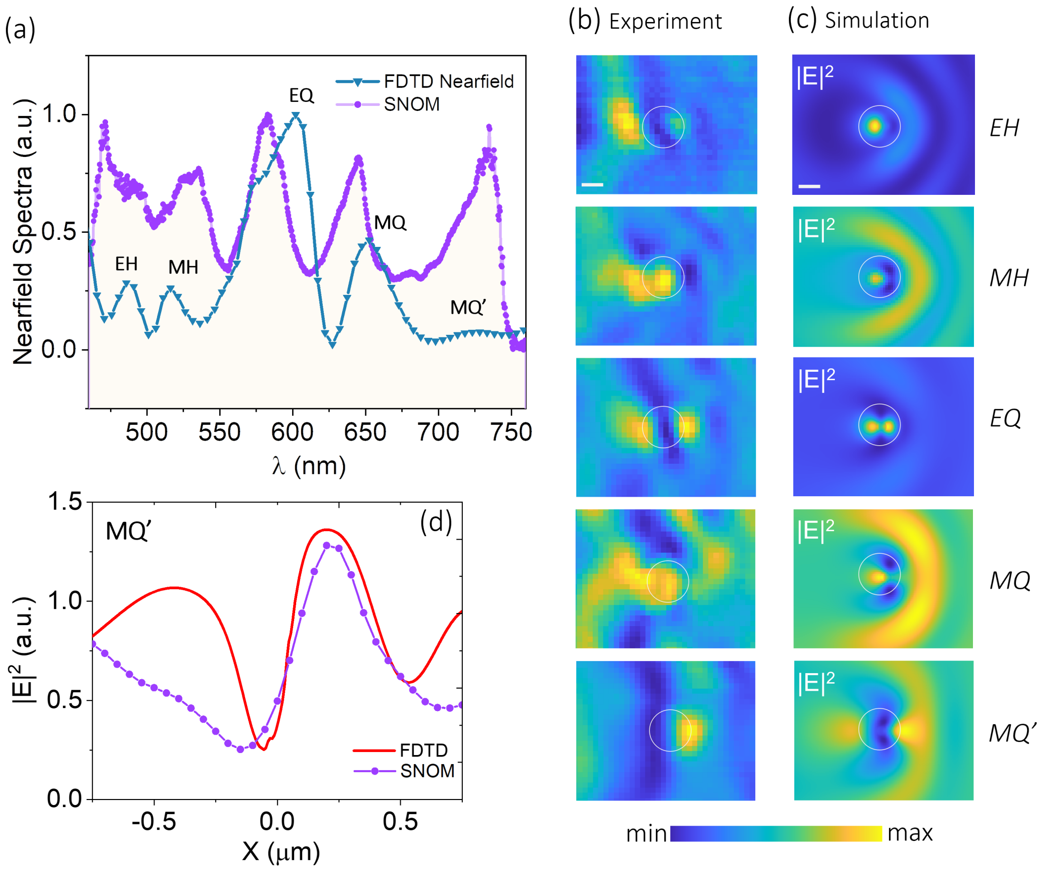

Figure 5.7. **(a)** Normalized SNOM scattering spectrum collected on top of the dewetted island of $d = 330$ nm (purple dots) and FDTD near-field spectrum acquired at 10nm distance from the top center of a hemisphere of the same diameter (in dark green). **(b)** Experimental SNOM maps filtered around the central wavelength of the purple spectrum in **(a)**, respectively relative to the EH ($\lambda = 490$ nm), MH ($\lambda = 530$ nm), EQ ($\lambda = 570$ nm), MQ ($\lambda = 645$ nm) and MQ’ $\lambda = 735$ nm modes. **(c)** FDTD maps of the electric field intensity of the multipolar resonances detected in the dark-green spectrum: EH ($\lambda = 485$ nm), MH ($\lambda = 521$ nm), EQ ($\lambda = 602$ nm), MQ ($\lambda = 654$ nm) and MQ’ $\lambda = 728$ nm. All white scalebars correspond to 200 nm. **(d)** Horizontal cuts along the central part of the experimental and the FDTD maps relative to the MQ’ resonance.

lations. Experimental and simulated maps show striking similarities in the spatial symmetry of the resonances that are typical of each mode and in the relative weights of the lobes of each mode, indicating preferential directions of scattering (Fig.5.7b and c). The asymmetric "ring crowns" are well reproduced, both in intensity, spatial location and distance from the island. Under tilted illumination, higher energy modes, like EH and MH, display a near-field scattered intensity that is unbalanced in opposite direction with respect to lower energy modes, like MQ and MQ' (towards left for EH and MH, towards right for MQ, MQ')). The EQ mode instead, exhibits a more symmetric distribution both in theory and experiment. The symmetry of EQ is well recognizable in the experimental map, where a vertical dip in the intensity of the signal is visible. In particular, the signal intensity of the MQ' mode reproduces with high fidelity the expected spatial modulation characterized by a bright lobe on the left side of the island and a clear signal dip on the opposite side. Deviations between theory and experiment can be ascribed to several factors: *i*) approximation of the island shape as an ideal hemisphere in contrast with a smaller aspect ratio, typical of the equilibrium shape of dewetted silicon [40]; *ii*) asymmetries and imperfections of the island shape that did not yet reach its final equilibrium shape [65, 64]; *iii*) presence of residual Si and intermixing of Si with the underlying SiO_2 resulting from the high temperature annealing [147] producing a strong scattering from the areas nearby the island, *iv*) projection of the near-field intensity neglecting the change in tip height during the scan on a 3D object that modifies the collection efficiency and slightly distort the reconstructed SNOM optical image. These results show that, in the perspective of maximizing the surface enhancement in absorption or in Raman scattering of a single molecule or other quantum system [34], it is possible to control the spatial overlap between the quantum center and the electric field hot spot by acting on the illumination angle. This represents an interesting alternative way to the most common approach based on the accurate positioning at the fixed field maximum.

5.3 Dark-field hyperctral imaging through scanning microscopy

In Section 4.2 of Chapter 4 we explained how dark-field spectroscopy, the most common and widely used technique for the study of the far-field properties of Mie resonators, was implemented on our SNOM microscope (Fig.4.6).

Sub-wavelength optical resonators, thanks to the unidirectional scattering arising from constructive and destructive interference between electric and magnetic dipolar modes, enable efficient manipulation of electromagnetic fields at the nanoscale, and can be a building block of functional metamaterials and metasurfaces. However, as explained in Section 2.2, the experimental determination of radiation patterns of individual nanoobject has been limited by the inability of angular analysis in conventional optical microscopes. Moreover, just like in the case of near-field measurements, only limited information about the multipolar character of higher order modes has been achieved [49].

In this Section we show how we are able to exploit the piezoelectric movements of the sample holder in the SNOM microscope in order to perform dark-field scanning microscopy. This advanced technique represents an important improvement with respect to standard dark-field microscopy, that usually implies the collection of a single far-field spectrum in a single point, generally on top of the scatterer. Here, we demonstrate, thanks to the reconstruction of a hyperspectral map, that dark-field spectra from a single scatterer display significant variations within 200 nm displacements of the collection spot, therefore implying a certain incompleteness of standard dark-field spectra. This is not the only improvement that we achieve: infact, we show how, thanks to the special combination of the lateral illumination and the collection objective sending the signal to an achromatic lens at the entrance of a 10µm core fiber (see Section 4.2, Fig.4.6), we are able to perform actual *Dark-field hyperspectral imaging*, that gives information correlated to the beam steering properties of a single scatterer.

5.3.1 Experiment

The investigated samples, of which a schematic representation can be found in Fig.5.1d, are monocrystalline SiGe islands (Ge 20%), fabricated through EBL assisted solid-state dewetting [18], separated by a thin layer (25 nm) of SiO_2 from the Si bulk substrate. In Fig.5.8a is shown a SEM image of the sample showing an ordered array of islands; since islands of different diameters can be fabricated, we focused on scatterers of two diameters, $d = 330$ nm and $d = 530$ nm. The dark-field setup, implemented on the SNOM microscope was used in order to study the far-field emission of the nano-resonators under an illumination tilted by an angle $\theta =$ 30°, as sketched in Fig.5.8b. We recall, as it has been explained in Section 4.2, that the presence of the 10 µm core optical fiber in the collection branch acts as a spatial filter, thanks to witch resulting collection spot is roughly of 1 µm diameter. The illumination source is the Super-continuum laser, and its spectral emission, collected with the objective after it was scattered by a lambertzian surface (*Spectralon*), can be found in Fig.5.2d. With this configuration it is possible to collect the scattered spectra in the dark-field, that are then sent to the CCD camera (complete setup description in Fig.4.6). We exploited the piezoelectric movements in the sample holder in order to obtain dark-field spatially resolved maps, collecting a single spectrum for every position of the scatterer under the objective. In Fig.5.8c and d (upper panels) we report the results of the dark-field scans performed on two SiGe islands, respectively with diameter $d = 330$ nm and $d = 530$ nm. The inset in the graphs represent the reconstructed optical maps (3 µm × 3 µm with 200 nm/px spatial step) integrated over the entire wavelength range (400-900 nm). The overlapped spectra, normalized to the illumination source spectrum, are obtained by performing a horizontal cut of 3 µm in the maps (highlighted with the colored rectangle), and are reported in a colorscale that reproduces the direction of the cut, from pixel A (yellow) to pixel B (blue). Every pixel of the cut corresponds to a single spectrum. The first thing to be noted is the clear difference between the two graphs: the far-field spectra of island with diameter 530 nm (upper panel of Fig.5.8d) show resonances at higher wavelengths with respect to the ones displayed by the island with $d = 330$ nm (upper panel of Fig.5.8c). This is a confirmation of what is well known in the literature of Mie resonators: bigger nanoparticles exhibit Mie resonances that are redshifted with respect to smaller ones [27] (see Section 2.2). The experimental

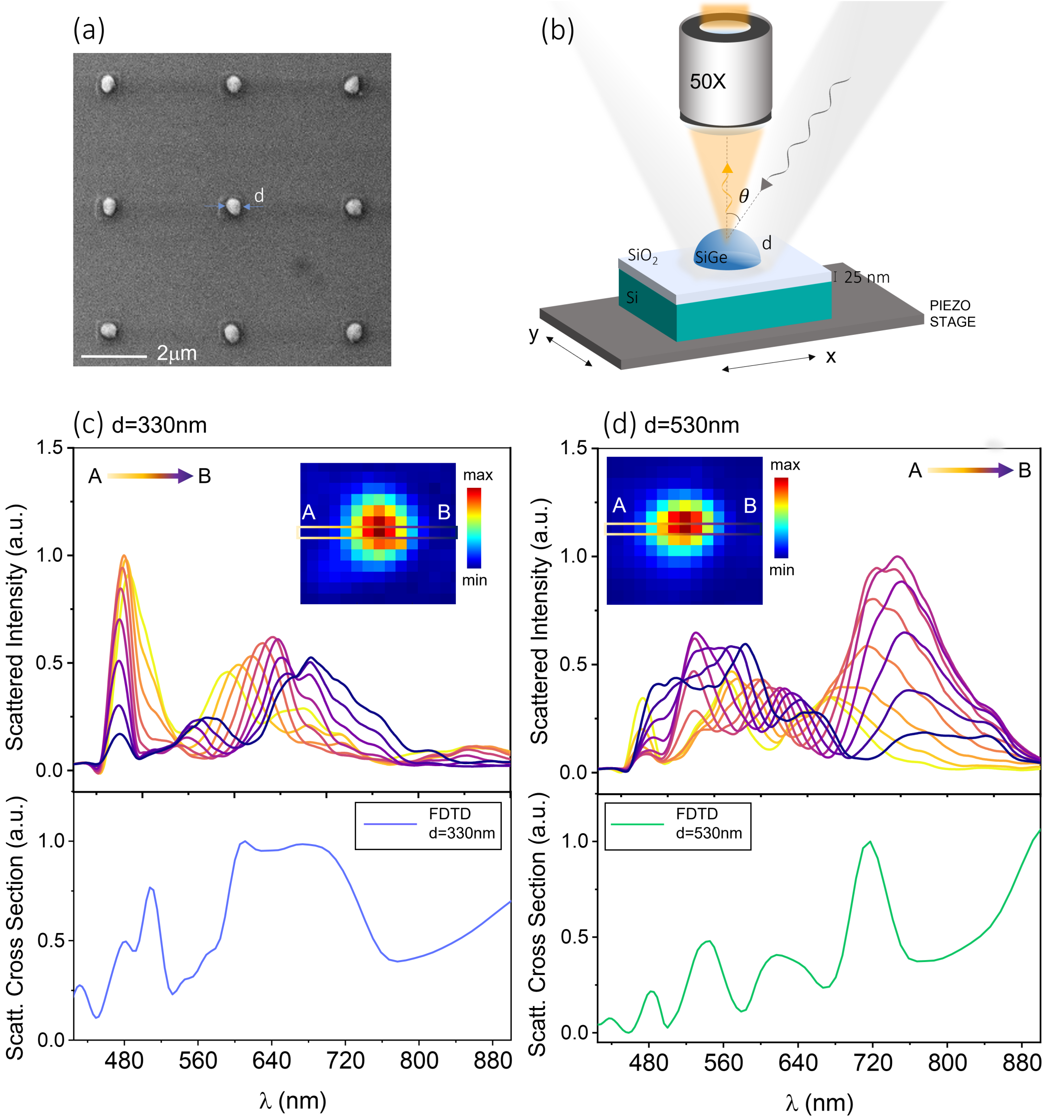

Figure 5.8. **(a)** SEM image of an ordered pattern of dewetted SiGe islands. **(b)** Sketch of the experimental set up: the tilted illumination (of an angle $\theta = 30°$ with respect to the axis perpendicular to the sample) from the Super-continuum is scattered by the island.**(c)** and **(d)** *Upper panels*: dark-field spectra of an island with diameter $d =$ 330 nm and $d = 530$ nm normalized to the Super-continuum source. The spectra are obtained by performing an horizontal cut on the hyperspectral map reported in the inset. The maps are filtered around the entire wavelength interval (400-900 nm). The cut is highlighted with a colored rectangle, and the colorscale of the spectra reproduces the direction of the cut, from pixel A (yellow) to pixel B (blue). *Bottom panels*: FDTD scattering cross sections of a hemisphere of $d = 330$ nm (purple) and $d = 530$ nm (green).

resonances are infact interpreted also with the help of FDTD simulations; we model the island with a hemisphere and simulate the broad illumination with a TFSF source (as explained in Section 5.2.2)[1]. A good agreement can be found between the experimentally detected resonances and the peaks of the calculated scattering cross section, reported in the bottom panels of Fig.5.8c and d (purple and green respectively for d = 330 nm and d = 530 nm), that well reproduce the redshift of the modes with the increasing of d. A second feature of the far-field emission can be deduced from this analysis; the spectra overlapped in the two graphs of Fig.5.8c and d have been acquired in adjacent pixels of the map, hence they correspond to spatial movements of the scatterer of 200 nm. A clear modulation of the spectra can be observed, and significant variations of the relative weights of the peaks arise between acquisition positions at only 200 nm distance from each other. Therefore, conventional dark-field measurements in which the spectra are acquired in a single position, clearly limit the amount of information deducible from the far-field emission of nanoparticles in the case of tilted illumination.

5.3.2 FDTD Hyperspectral map

As explained above, at the end of a dark-field scan measurement it is possible to reconstruct a hyperspectral map. This is because for every step of the scan, i.e. every position of the scatterer, the objective collects a single spectrum. This led us to discover the modulations in the far-field spectra of a single scatterer within acquisitions distant only 200 nm. In order to validate the measurements, we reproduced the dark-field scanning with FDTD simulations. In Fig.5.9a it is reported a sketch of the top view simulation scheme that allows to reproduce the measurement; the orange square represents the FDTD domain, and the blue square delimits the scanning area, 2 µm × 2 µm. At 1 µm distance from the the scatterer, and at the center of this area, a 1 µm × 1 µm monitor is placed (in order to reproduce the experimental 1 µm collection spot), and collects the far-field spectra scattered by the SiGe nanoparticle of diameter d = 330 nm (under an x-polarized plane wave source tilted by 30° with respect to the axis perpendicular to the xy plane) in all its positions during the scan. The movements of the scatterer, of 200 nm each, are reproduced by imposing a sweep in the x and y position coordinates of the island starting from the top right coordinate (1,1) µm (as highlighted by the red cross). In the picture of Fig.5.9a, the scatterer is displayed in four x positions relative to the central row (y = 0 µm). For every (x,y) position of the scatterer, the electric field intensity spectra acquired by the monitor are then integrated in a cone of NA = 0.45 (corresponding to the experimental collection angle of 27°). In this way we reconstruct the FDTD hyperspectral map of Fig.5.9b, filtered over the whole wavelength interval (400-900) nm; in this map, the bottom left pixel (labelled with the red cross) is relative to the spectrum acquired for the scatterer position (1,1) µm. Analogously to what we showed in Fig.5.8, we performed a 2 µm horizontal cut in the map of Fig.5.9b; the results are shown in the bottom graph of Fig.5.9c, where

---

[1] The FDTD results of Fig.5.8c and d bottom panels are obtained with a TFSF source at normal incidence. This choice is due to the fact that the Mie resonances of islands on thin substrates (in this case 25 nm) are not subjected to significant spectral shifts by changing the angle of illumination (as explained in Section 5.2.2, Fig.5.5).

the FDTD spectra of the cut are compared with experimental ones, obtained on an island of the same size (same graph of Fig.5.8c).

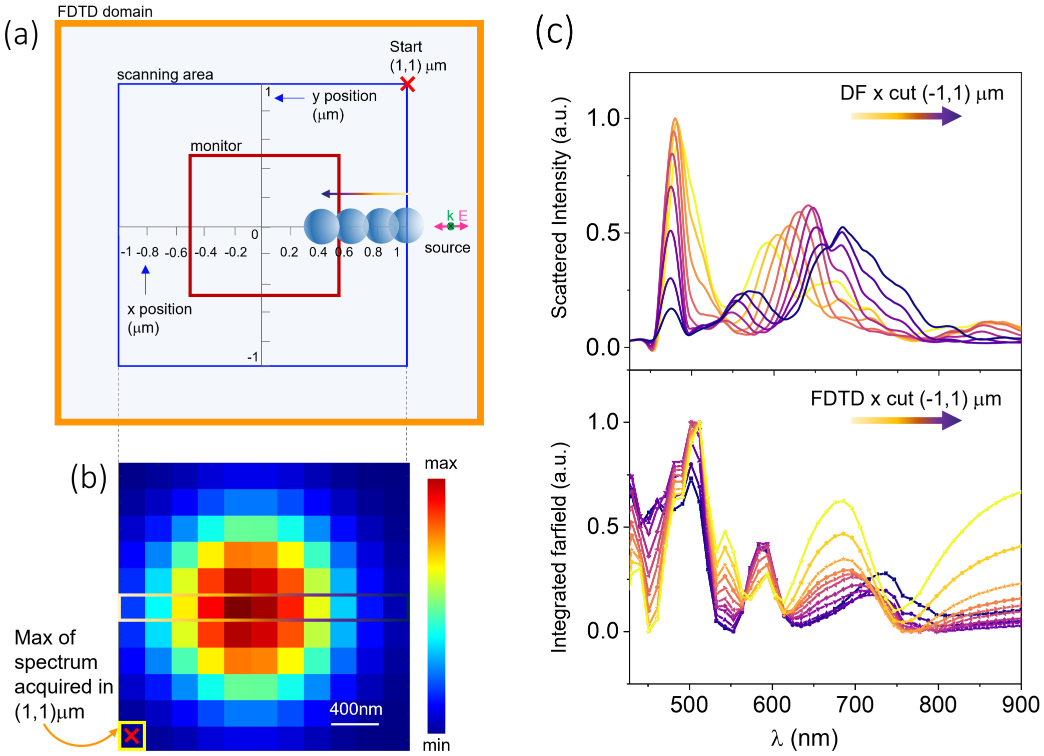

Figure 5.9. **(a)** Top view sketch of the FDTD simulation of scanning. The scanning area is highlighted by the 2 μm × 2 μm blue square; the central monitor (red square) acquires the electric field intensity spectra scattered by the SiGe hemisphere of diameter $d = 330$ nm starting from the top right position (1,1) μm (red cross) and ending at (-1,-1) μm, at 200 nm steps. The scatterer in the sketch is represented in four position during a scanning in the central row. The source is an x-polarized plane wave tilted by 30° with respect to the axis perpendicular to the xy plane. **(b)** FDTD Hyperspectral map reconstructed with the scanning 2 μm × 2 μm; each pixel is 200 nm. **(c)** Comparison between the experimental (top panel) and simulated (bottom panel) spectra obtained with a 2 μm horizontal cut respectively in the dark-field map of Fig.5.8c and the FDTD map of b.

We observe a fairly good reproduction of the spectral positions and a quite good agreement between experiment and simulation regarding the modulation and spectral shift of the peaks with the different scatterer positions. Specifically, if we refer to the colorscale (yellow-purple) relative to the displacement of the scatterer, the yellow peaks around $\lambda = 700$ nm are redshifted in both graphs.

5.3.3 Dark-field Hyperspectral Imaging Experiment

We now move to the final results of this Section. We report the results obtained through a dark-field scanning on the SiGe island of diameter $d = 330$ nm, and we demonstrate experimentally that the hyperspectral maps reconstructed from the measurement are related to the beam steering properties of the multipolar Mie terms, to wich we have access through FDTD simulations. The performed measurement is a 200 nm/px spatial step scan, obtained by collecting the dark-field signal for every position of the island, illuminated with the super-continuum source tilted by 30°. All the spectra are normalized to the illumination source. In Fig.5.10a it is reported in magenta a typical normalized dark-field spectrum acquired in a position of maximum scattered intensity; the experimental spectrum is compared with the FDTD scattering cross section σ of a hemisphere of diameter 330 nm (purple spectrum) on a 25 nm SiO_2 substrate, that was also shown in the bottom panel of Fig.5.8c. The two curves nicely agree with each other. The identification of the multipolar Mie resonances is done according to the procedure described in Section 5.2.2, i.e. analyzing the crosscuts of the electric and magnetic field intensity along with the current loops starting from the bare case of the island in air. The four higher order terms are identified in the scattering cross section peaks and labelled with the colored triangles: magnetic quadrupole MQ ($\lambda = 675$ nm, orange triangle), electric quadrupole EQ ($\lambda = 604$ nm, red triangle), and electric hexapole EH ($\lambda = 502$ nm, blue triangle). Note that if we compare this σ (island on a 25 nm SiO_2 substrate) with respect to the one of the island in air (as reported in Fig.5.3), the MH mode results suppressed. Thanks to the agreement between the dark-field spectrum and the FDTD scattering cross section, it is possible to identify the modes in the experimental signal as well, as highlighted by the colored dots: MQ ($\lambda = 686$ nm, orange dot), EQ ($\lambda = 636$ nm, red dot) and EH ($\lambda = 485$ nm, blue dot). In order to theoretically characterize the beam steering properties of the island, and study how it is affected by the angle of illumination, we computed the far-field scattering distributions of the SiGe island sitting atop 25 nm of SiO_2 and illuminated by the TFSF source tilted by 30°. A 2.5 µm × 2.5 µm planar frequency monitor is placed at 60 nm distance from the scatterer, as sketched in Fig.5.10b (purple monitor). The data acquired from the monitor during the FDTD simulations can be converted into far-field angular distributions and then into $k-$space patterns that can be viewed in 3D as a radiation plot. An example of this procedure regarding the EQ mode can be viewed in the sketch of Fig.5.10b, where it shown how the 3D radiation plot results from the planar far-field angular distribution at $\lambda = 604$ nm. In Fig.5.10c are reported the three FDTD far-field plots of the Mie resonances EH, EQ and MQ, describing the angular emission of the scattered electric field intensity along the two axis of the k-space, u_x and u_y. Interestingly, we find that the angular distribution of scattering is decentralized with respect to the u_y axis due to the lateral illumination from the x-polarized wave coming from the right direction. This can result clear by looking at the bottom right inset of Fig.5.10b, where the polar plots of EQ for normal illumination and tiled illumination are compared. This result is strictly correlated with what has arised from the near-field analysis in a condition of tilted illumination (see Fig.5.4 and 5.7), where we have shown that it is possible to exploit the modes distribution sensitivity to the angle of illumination to redirect and control light. The polar plots of Fig.5.10c confirm that the beam steering properties of Mie resonators can indeed be modulated, enhanced or suppressed by playing with the illumination angle. We further investigate the scattering properties of the nanoparticle by looking at the real space maps of each mode's electric field intensity $|E|^2$; in order to do this, a 4 µm × 4 µm planar frequency monitor is placed at 5 µm distance from the scatterer (represented in red in the sketch of

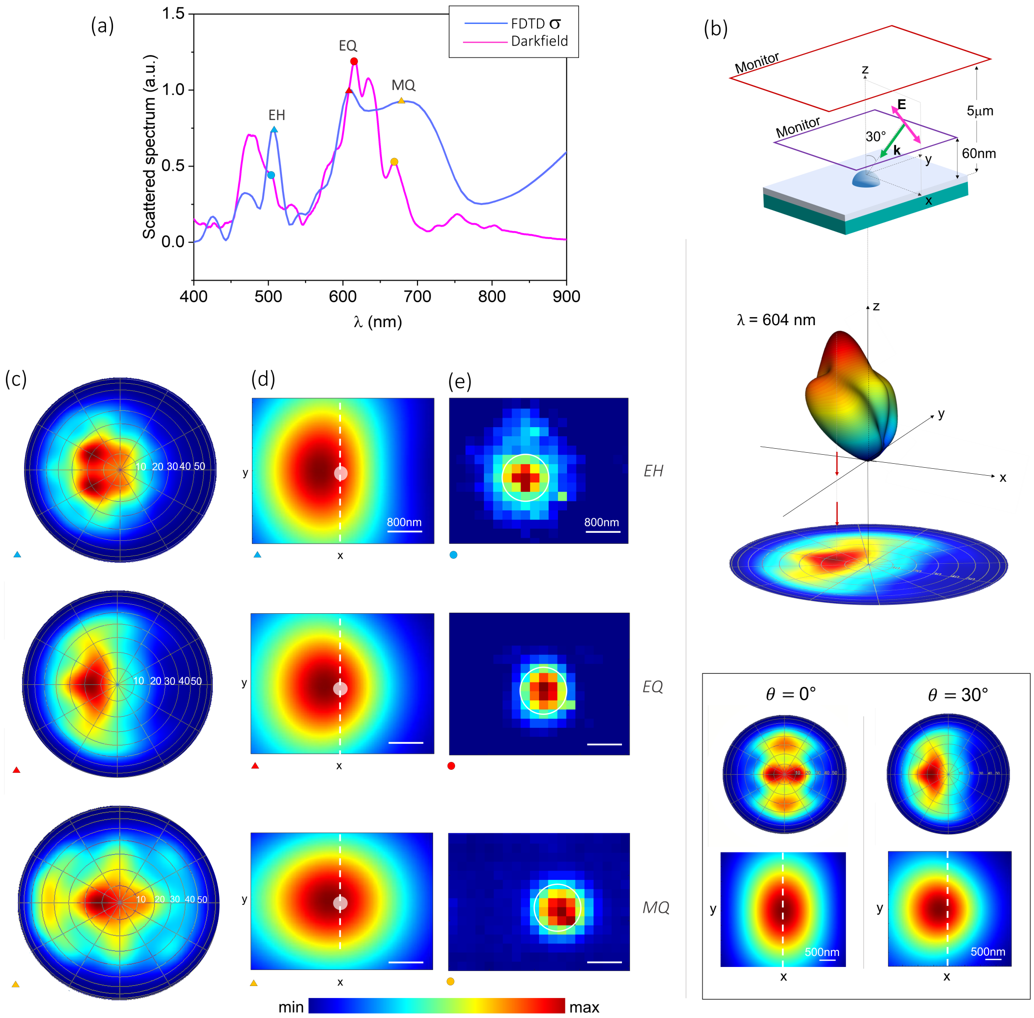

Figure 5.10. **(a)** FDTD scattering cross section (purple) of a SiGe island separated by Si-bulk by a SiO_2 substrate of thickness 25 nm under normal illumination, compared with a normalized dark-field spectrum acquired on top of the island during a darkfield scanning of 200 nm/px spatial step. The peaks indicate the presence of three Mie resonances, labelled with the colored triangles (dots) in the FDTD (experimental) curve. **(b)** Sketch of the FDTD simulation that leads to the extraction of far-field angular patterns that can be projected in 3D to reconstruct the scatterer beam steering at a single wavelength, in this case $\lambda = 604$ nm (corresponding to EQ). In the bottom inset the EQ polar plots in k-space and $|E|^2$ spatial distribution maps in real space, for normal illumination (0°) and tilted illumination (30°) are compared. All maps are normalized to their own maximum. **(c)** FDTD polar plots (or Fourier space maps) of every mode corresponding to the peaks in the scattering cross section, reported in order of decreasing energy: MQ $\lambda = 675$ nm-orange triangle in the blue spectrum of (a), EQ $\lambda = 604$ nm-red triangle and EH $\lambda = 502$ nm-blue triangle. **(d)** FDTD real space maps of the electric field intensity spatial distribution for the three peaks MQ, EQ and EH; the white small dot indicates the position of the island ($d = 330$ nm). **(e)** Experimental hyperspectral maps obtained through dark-field scanning microscopy, filtered around the central wavelengths of the three experimental peaks.

Fig.5.10b). The maps of $|E|^2$ are reported in Fig.5.10d for EH, EQ and MQ. The small white dot indicates the scatterer position and dimension. We observe that these maps are related with the ones in Fig.5.10c, since the spatial distribution of $|E|^2$ follows the directionality of the polar plots, reproducing the decentralization determined by the lateral illumination. A further confirm comes from the bottom inset of 5.10d, where the $|E|^2$ map of the EQ mode is reported under normal illumination and compared with the one obtained under tilted illumination. It is worth noticing that, in terms of increasing wavelength, the three modes (EH, EQ and MQ) scattered electric field intensity shifts from left to right of about 400 nm. If we compare this to Fig.5.10c, we see that in Fourier space this translates into each mode hotspots to point towards different angles, specifically $\approx 20°$ for EH, $\approx 18°$ for EQ and $\approx 15°$ for MQ. This unidirectional scattering behaviour is reproduced in the maps of Fig.5.10d, that are the experimental hyperspectral maps obtained through dark-field scanning microscopy, filtered around the central wavelengths of the three experimental peaks; from the EH map to the MQ, the maximum intensity hotspot moves from left to right, analogously with what is observed for FDTD maps. The reduced dimension of the maximum intensity spot (highlighted by the white circle) is due to the presence of the collection fiber that acts as a spatial filter.

In conclusion, we provided a complete optical characterization on the higher order multipolar Mie resonances in a single all dielectric island obtained by solid state dewetting. Through the Near-field hyperspectral imaging technique, we were able to study the modes arising from the combination of the Mie resonances of the scatterer with the etalon effect due to a thick SiO_2 layer below the scatterer. By means of FDTD simulations we achieved a full comprehension of the sensitivity of *magnetic light* with respect to the thickness of the substrate and the angle of illumination. The combination of numerical and experimental results offers a detailed analysis of how such sensitivity affects the near-field scattering pattern of the antenna, suggesting a novel approach to engineer the coupling of a single emitter with localized electric field maxima: infact, if external illumination can have an impact on the emission, in particular, it could offer certain control on the absorption of the emitter in this kind of photonic applications.

We completed the study by focusing on the beam steering properties of an island on thin SiO_2 substrate; thanks to FDTD simulations we were able to detect how the far-field emission of the Mie resonator is influenced by the angle of illumination, further confirming what arised from the Near-field study. The theoretical results are validated by the new developed technique of Dark-field hyperspectral imaging, that allowed us not only to discover a high degree of space dependence of the modulation in the scattered fields; it also allowed to reconstruct the spatial profiles of the electric field intensity for high order multipolar Mie term, that resulted intrinsically related to the scattering directionality.

Chapter 6

Deep subwavelength imaging of Hyperuniform Disordered Systems: from light transport regimes to quantum electrodynamics

Disordered photonic nanostructures have attracted tremendous interest in the past three decades, for the fascinating, complex and elusive physics of light transport in random media, and for peculiar functionalities in a wealth of interesting applications. Recently the interest in dielectric disordered systems has received new inputs by exploiting the role of long-range correlation within scatterers configurations. In particular, hyperuniform photonic structures, that share features of both photonic crystals and random systems, constitute the archetypal of a system where light transport can be tailored from diffusive transport to an intermediate regime dominated by light localization due to the presence of photonic band gap. Here, we exploit a Hyperuniform Disordered (HuD) special design in slab photonics, the use of embedded quantum dots for feeding the HuD resonances and Near-field hyperspectral imaging with sub-wavelength resolution in the optical range to explore the transition from localization to diffusive transport. In Section 5.1 we provide a description of the theoretical design and of the fabrication process of the first ever optically active HuD samples. In Section 5.2 we show, both theoretically and experimentally, that photonic HuD systems support a variety of resonances ranging from strongly localized modes to extended modes. Then, in the Section 5.3, we explain that Anderson-like modes with high Q/V are created, intrinsically reproducible and resilient to fabrication-induced disorder, thereby paving the way for a novel photonic platform for quantum applications. We conclude the Chapter by presenting a near-field imaging of high-Q optical cavities in slab architectures in HuD enviroment.

Whereas periodic structures with perfect translational symmetries display only a limited number of rotational symmetries, disordered and aperiodic geometries display arbitrary rotational symmetries, which can lead to superior optical functionalities in many photonic applications, such as enhanced light extraction from light emitting diodes [148], omnidirectional absorption for solar applications [149] and random lasing [150]. In the last few years, disordered dielectric materials with structural correlations, which fill the gap between random structures and perfectly ordered photonic crystals, have generated an ever-growing interests [151, 152]. A special class of these materials are the Hyperuniform Disordered (HuD) photonic systems, that we have introduced in Chapter 3, where we stressed how a quantitative experimental demonstration of the variety in light transport within a single HuD structure is missing in the optical range. In this Chapter, we directly measure the transition from localization to diffusive transport within a single system by exploiting near-field mode imaging capable of subwavelength resolution in the near-IR range. To this end we are employing a special design of HuD in slab photonics with embedded quantum dots for feeding the HuD resonances via photoluminescence, realizing the first ever *optically active* HuD system. The use of near-field Hyper Spectral Imaging with subwavelength resolution allowed us to perform a statistical analysis of individual many photonic modes, determining their Q factor, Inverse Participation Ratio (IPR), mode volume V and areal density. We theoretically predict and experimentally demonstrate that photonic HuD systems support a variety of transport regimes as well as a photonic band gap. We also show that high Q-factor and small mode volume resonances are created in strong similarity to photonic crystal cavity but with the advantage of having a very small footprint. Eventually these modes turn out to be intrinsically reproducible, with the mode spatial distribution robust against fabrication-induced disorder.

6.1 Studied samples

6.1.1 Theory and design

In this Section we aim to give a description of how the design of the studied samples was generated within the theoretical framework introduced in Section 3.3.1. The theoretical design was developed in the University of Surrey. We begin our analysis with the study of a purely 2D HuD network system (shown in Fig.6.1a), generated with a protocol described in Section 3.3.1. Analogously to the lattice constant in photonic crystals, we define a length scale $a = L/\sqrt{N}$, such that an N-point hyperuniform pattern in a square box of side length L has a scatterer density of $1/a^2$. The point pattern we use contains N =500 points and belongs to a further sub-category of HuD systems, known as “stealthy” [103] (Section 3.2), whose name relates to their property of being transparent to incident radiation for a certain range of wavevectors k. In particular, we consider a stealthy point pattern with a structure factor $S(k)$ that is statistically isotropic, continuous and precisely equal to zero for a finite range of wavenumbers smaller than a certain wavevector k_c, i.e., $S(k < k_c) = 0$. The stealthiness parameter χ is defined as ratio between the number of k vectors for which the structure factor $S(k)$ (shown in the inset of Fig.6.1a) is constrained to vanish and the total number of k vectors. A summary of the main

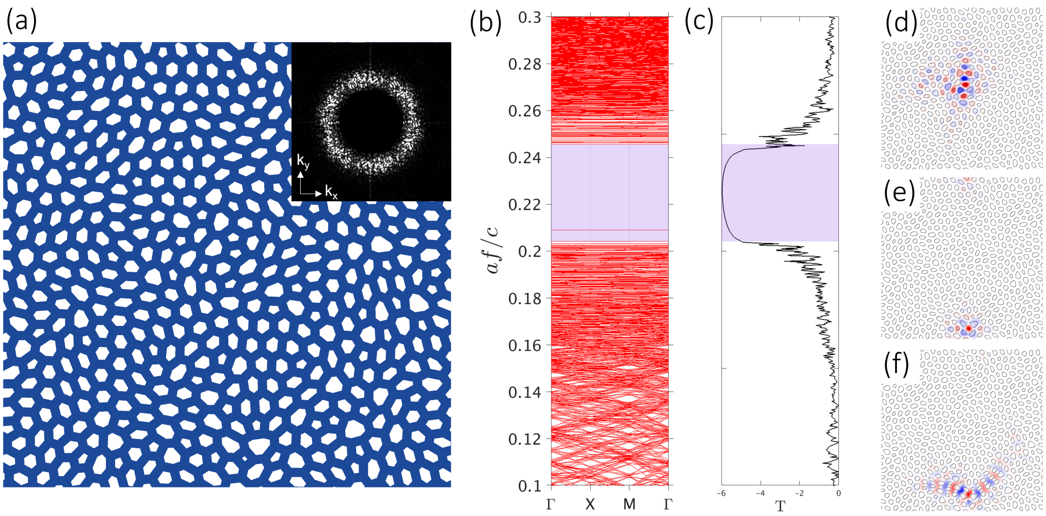

Figure 6.1. **(a)** Sketch of the theoretical design of the studied hyperuniform disordered network, with length scale a = 380 nm and wall thickness $w = 0.44a$. The pattern contains 500 points. The inset shows the structure factor $S(k)$ of the system. **(b)** 2D Bandstructure (MPB) corresponding to the design in a). f is the frequency. **(c)** 2D transmission spectrum. The purple stripe corresponds to the PBG. **(d)**, **(e)**, **(f)** Magnetic field H_z (component normal to the plane) of band 499, 500 and 501. Structure contours are shown as black lines.

properties for a system with χ=0.5 and a = 380 nm is given in Fig.6.1; the index of refraction is set to $n = 3.4$, and thickness of the dielectric veins (the network wall thickness) is $w = 0.44a$. The 2D photonic band structure reported in Fig.6.1b is calculated using the planewave expansion software MPB [105]. The photonic band gap (purple region) is not affected by the folding and is located between bands (red lines) N and $N + 1$, where N is the number of scattering cells in the supercell, in this case $N = 500$. The transmission spectrum (Fig.6.1c) is obtained via FDTD methods (Section 4.3.1). The resulting transmission spectrum and 2D bandstructure are in very good agreement; the clear suppression of the transmission over a range of frequencies indicates the presence of a PBG, as predicted by the bandstructure calculations. As explained in Section 3.3.2, like other conventional disordered structures, unperturbed HuD structures display spatially localized modes. These Anderson-like localized modes occur naturally at the PBG edges and are predicted to spread over a few cells of HuD network structures [101, 153]. Calculation of the HuD network's bandstructure with MPB offers information on both the frequency and spatial distribution of the modes. By itself, the spatial extent provides useful knowledge on the wave transport process. In Figs.6.1(d), (e) and (f) we report the distributions of the magnetic field component normal to the xy-plane, H_Z, of bands 499, 500 and 501, respectively. These modes are archetypal examples of the main features of HUD; interestingly, mode 500 (corresponding to the most isolated band inside the gap in Fig.6.1b), is an accidental defect mode arising due to local peculiar topology [153] on the four-sided cells; we note that most of the cells in the structure are surrounded by five, six or seven sides with an average of six sides per cell. The accidental defects are quite rare but unavoidable, and we introduced them in Section 3.3.2. The defect modes associated with them are most often located around the lower edge of the PBG, and they represent an interesting peculiarity of HuD; they are improper Anderson-localized modes, in the sense that they require disorder in order to exist, and vanish as disorder is increased. Differently, all the other modes arising at the band edges can be considered actual Anderson-like, as their localization length decreases with disorder. Mode 499 is the first localized mode in the dielectric band, while mode 501 is the first localized mode of the air band. This means that the difference between them, in terms of frequency, defines the side of the HuD-PBG. In addition, as we have seen in Section 3.3.2, they are easily distinguishable as below (Fig.6.1d) or above (Fig.6.1f) the PBG due to the electric field being concentrated in the dielectric or air fraction, respectively. The physical reason is that below the bandgap, TE modes concentrate the magnetic field inside the air fraction (electric field concentrated in the dielectric material) as to reduce the electromagnetic energy functional [91]. Above the gap, due to the requirement that solutions to the Maxwell-eigenproblem are orthogonal, the magnetic field is pushed into the dielectric material as nodes form in the air fraction; this is a well understood paradigm in periodic structures [66] that can be observed also in HuD systems. The method of wave transport can also be inferred from the field profiles. Low-frequency modes have an extended profile that suggests ballistic propagation; the structure has limited influence on the mode profile. For higher frequencies, the modes become much more localized; the band-edge modes are confined to within just a few cells due to Anderson localization. Consequently, in hyperuniform systems the quality factors for the low-frequency modes are low and increase approaching the band gap. The field profiles of these modes echo the nature of the transition in the wave transport of the modes. Low frequency modes have extended field profiles, with the electromagnetic energy quickly leaking out through in-plane boundaries. On the other hand, localized modes are confined away from the in-plane boundaries; their decay is therefore slower and their quality factors higher. Resonances in close spectral proximity to the PBG have very large Qs relative to other modes, owing to Anderson-like localization confinement in the plane of structuring.

The mode profiles shown so far are calculated for a structure with infinite extent in the vertical direction i.e., a 2D simulation. For an in-plane slice at the vertical center of a 3D slab with the same design, we expect to find a very similar field profile to the mode's 2D counterpart, just at a higher frequency. As a result, from the 2D field profile of a band-edge mode, we can deduce the exact band edge frequency of the 3D-slab. By monitoring the evolution of the in-plane field with time, we obtain the electric field profiles of three selected modes of the 3D HuD network slab as presented in Figs.6.2(a), (b) and (c), together with the corresponding Fourier transforms in Fig.6.2(d), (e) and (f). From the profile of their Fourier transforms, is evident that these three modes are well confined in the vertical direction, with most of the reciprocal space components located outside the light cone. In particular, Figs.6.2a, d are relative to a typically delocalized mode (band 479, $\lambda = 1349$ nm) with a Q-factor of 920, which is much lower than the Q factor of the localized mode at the band edge in Figs.6.2b, e (band 499, $\lambda = 1310$ nm) displaying a Q-factor of 4200. Figures 6.2c, f display the behavior of the four-fold topological defect (band 500, $\lambda = 1280$ nm): this mode displays a lower Q-factor (750) despite the tighter in-plane spatial confinement, due to the losses in the vertical direction associated with

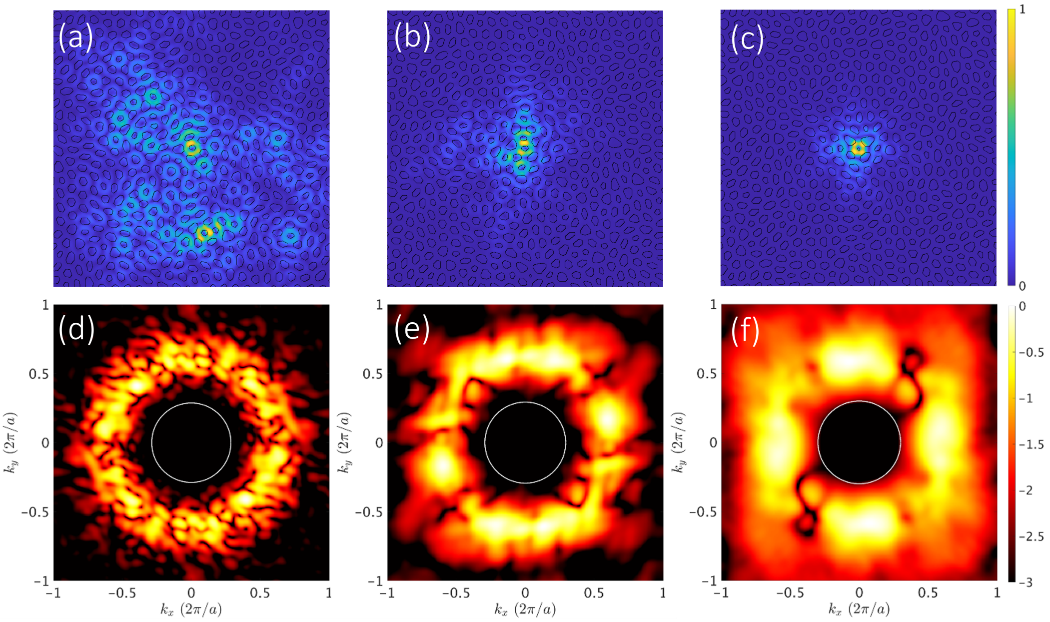

Figure 6.2. FDTD Electric field intensity profile ($|E|^2$) of band 479 **(a)**, 499 **(b)** and 500 **(c)** modes respectively. Note that mode 500 has been translated in the center of the simulation window. **(d)** , **(e)** and **(f)**: Fourier transform of the magnetic fields that correspond to the electric field intensity profiles in **(a)**, **(b)** and **(c)** respectively; the light cone in each case is indicated by the white circle.

the $k-$space components inside the light cone and directly related to the symmetry and the spatial extent of the intensity profile [100].

6.1.2 Samples fabrication

The samples were fabricated at the University of Technology, in Eindhoven, by molecular beam epitaxy on a GaAs (001) wafer and consist of two GaAs parallel membranes. The integration of small scale optoelectronic devices with electromechanical systems forms a novel class of devices commonly denoted as micro or nano-opto electromechanical systems (MOEMS and NOEMS) [154, 155, 156]. Double membrane photonic systems have been recently proposed as novel devices for sensing and metrology applications, based on the achievement of deterministic control of the supported modes [134, 157, 158]. The long term objective of this study is to lay the foundations for a novel employment of HuD systems in the field of tunable devices, which is outside the scope of this thesis.

The steps of the fabrication process are shown in Fig.6.3a. The epitaxial growth of III/V wafers was performed by molecular beam epitaxy. The sample growth starts with an undoped (100) substrate. A thick (1–1.5 µm) $Al_{0.7}Ga_{0.3}As$ sacrificial layer is initially deposited to separate the double-membrane structure from the substrate. Then, two structural membrane layers (GaAs) having the same thickness and an $Al_{0.7}Ga_{0.3}As$ inter-membrane sacrificial layer are grown (Step 1 of Fig.6.3a). In the middle of the upper membrane membrane of GaAs, high-density Indium Arsenide (InAs) Quantum Dots (QDs) are grown by molecular beam epitaxy by exploiting

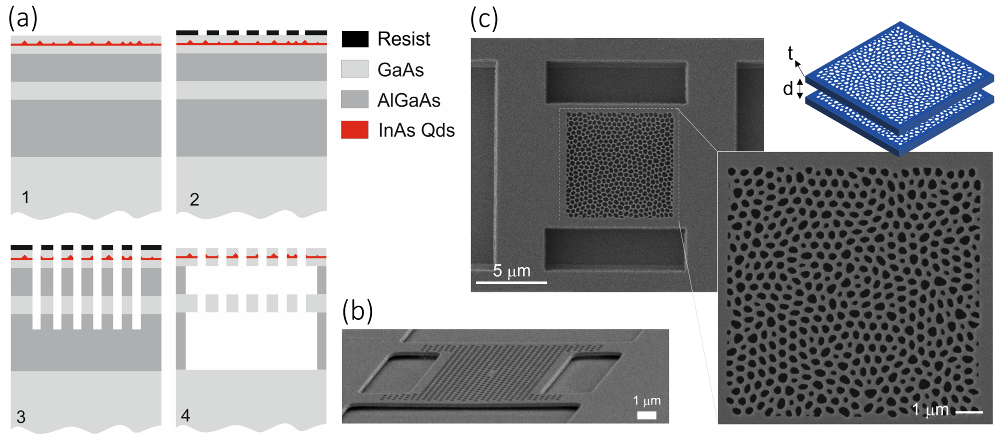

Figure 6.3. **(a)** Four subsequent fabrication steps (1-4) performed to create the GaAs (light-gray) double membrane system with InAs QDs embedded (red layer). The dark-gray region represents the $Al_{0.7}Ga_{0.3}As$ sacrificial layer and the black layer is the SiN resist mask. **(b)** SEM image displaying an example of a typical double membrane photonic crystal cavity. Reprinted from [154]. **(c)** SEM image top view and zoom of the studied sample, a double membrane patterned with the HuD design of Fig.6.1a. On the right upper part a 3D reconstruction of the device is shown, highlighting the two structural parameters, inter-membrane distance d and membrane thickness t.

the Stranski-Krastanov self-assembly technique [159]. The QDs emit at room temperature, and their ground-state emission is centered around 1300 nm. The desired HUD pattern is realized by combining Electron Beam Lithograhy (EBL) and Reactive Ion Etching (RIE). A thick (400 nm) SiN layer is deposited on the sample and then coated with ZEP 520A (e-beam resist). The patterns are exposed, aligned to the existing structures, by EBL (Step 2 of Fig.6.3a). After development, the holes are etched in the SiN mask by RIE with pure CHF_3 for approximately 20 minutes. The residual resist is stripped off with O_2 plasma. From the hard mask, the HUD pattern is etched into both membranes (and the inter-membrane sacrificial layer) with inductively coupled plasma (ICP) for 2.5 minutes (in Cl_2/N_2), (Step 3 of Fig.6.3a). The sacrificial layers are etched using a selective hydrochloric acid solution without removing the SiN mask. After the sample has dried, the SiN mask is removed in a barrel etcher with CF_4 plasma (Step 4 of Fig.6.3a). Finally, the free-standing structures are released after the wet etching of a sacrificial layer. An example of a typical photonic crystal cavity MOEMS is reported in the SEM image of Fig.6.3b. The studied samples have been patterned with the HuD design shown in Fig.6.1a, and the SEM top view image (and zoom) of the final result of fabrication is reported in Fig.6.3c. Two important parameters must be taken into account in order to comprehend the spectral positions of the modes in MOEMS: the inter-membrane distance d and the membrane thickness t (upper right 3D sketch of Fig.6.3c). In the special case of HuD design, also a third structural parameter must be considered: the wall thickness w, i.e. the width of the dielectric walls separating each air hole. Infact, during the fabrication of photonic devices, the EBL process often determines an enlargement of the air holes with respect to nominal value. In photonic crystal lattices this phenomenon has a well known effect of blueshifting the spectral resonances (*air defect* effect [66]). Also in the novel case of photonic HuD systems, as it will be explained in the next Sections, the enlargement of the holes (and therefore a decrease in the wall thickness w) strongly affect the spectral positions of the resonances. This led us to perform a post-fabrication SEM analysis to give a rough estimation of the actual structural parameters, to which the following paragraph is dedicated.

SEM characterization of structural parameters

In order to achieve a full comprehension of the experimental results and to obtain a better comparison with theory, we performed a detailed post- fabrication Scanning Electron Microscopy (SEM) investigation of the measured sample. From the analysis of the images, we were able to give a rough estimation of the actual structural parameters, slightly different from the nominal ones due to the fabrication process. In Fig.6.4a it is shown a SEM image acquired on the tilted sample, from which it was possible to extract (with a geometrical proportion that takes into account the tilting angle) the values of the thickness of the membranes t and the inter-membrane distance d, respectively $t \approx 130$ nm and $d \approx 105$ nm. As explained before, the top view SEM images like the one shown in Fig.6.4b allowed to see that the holes of the sample resulted bigger than the ones in the original design. This effect was graphically quantified in two ways: a first approach consisted in measuring w from some of the dielectric veins in the image (as shown in the zoom of the yellow square in Fig.6.4b) and then performing an average calculation. The values of the selected veins are reported in the table. We extrapolated a mean value of $w \approx 135$ nm. However, a more precise estimation came from the construction of a binary image in black and white of the network, starting by using the polynomial relation between the filling fraction ff and the thickness w of the walls, shown in Fig.6.4c, provided by theory. In the provided samples, many designs were fabricated, different from each other by the value $a = 340$ nm, 360 nm and 380 nm, and by the wall thickness $w/a = 0.394$, 0.44 and 0.489. Moreover, many nominal copies of the same design were realized. Therefore, we analyzed with SEM many of these different designs and replicas; from the SEM top views images, converted into binary images, we graphically estimated ff. Then, by using the polynomial relation that links ff to w in HuD systems, we determined the approximated value of w/a. The results are shown in in Fig.6.4d; the three blue dots correspond to the three nominal values of w/a (labelled on the x axis as 1 for 0.394, 2 for 0.44 and 3 for 0.489). The three values of w/a were designed to remain constant for different values of a. However, due to some fabrication effects, from the SEM analysis they resulted slightly different for different a: this is clear by looking at the grey dots, where for every nominal position 1, 2 and 3, different values of w/a for different a are evidently not coinciding. From a global point of view, all the fabricated samples display a w/a that is smaller with respect to the nominal design w/a, and this is a quite typical effect of the EBL process.

For the specific sample that will be analyzed in the next sections, we obtained $w/a = 0.385$ with respect to the nominal value $w/a = 0.44$. This confirm the fact that the actual wall thickness is smaller than the nominal value, and in the studied case

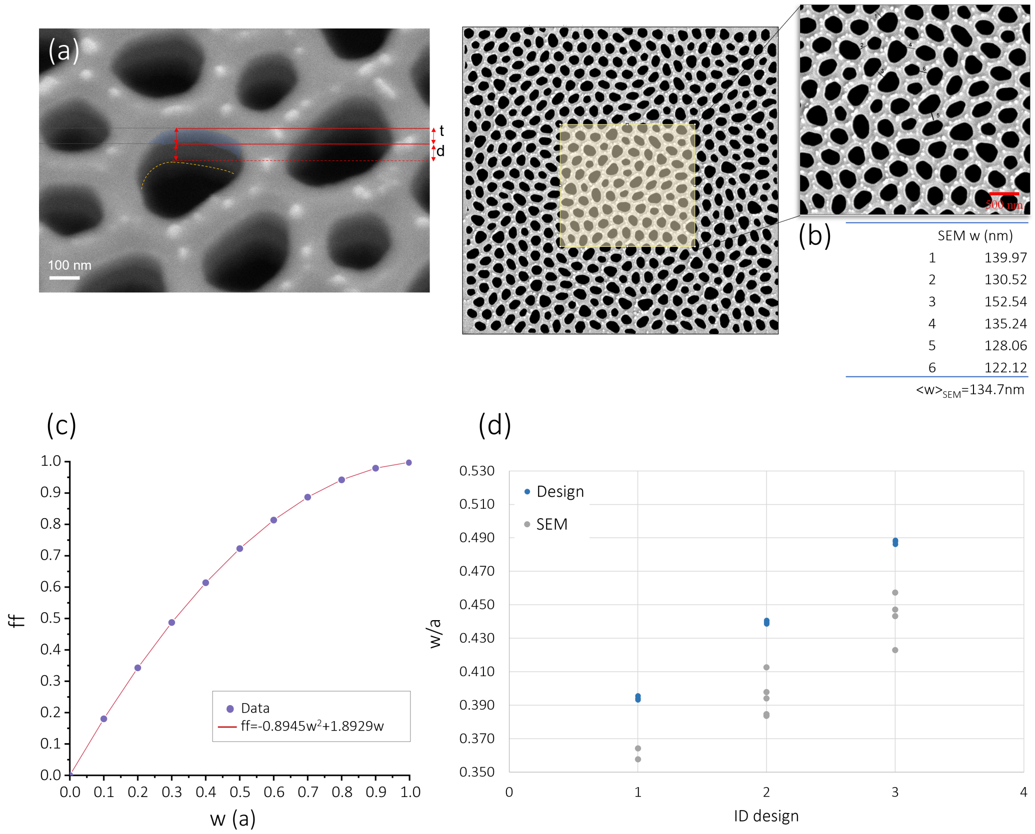

	SEM w (nm)
1	139.97
2	130.52
3	152.54
4	135.24
5	128.06
6	122.12

$\langle w \rangle_{SEM}$=134.7nm

Figure 6.4. **(a)** SEM image acquired on the tilted sample, from which it is possible to roughly estimate the thickness of the membranes t and the intermembrane distance d. **(b)** Top view SEM image of the sample; the yellow squares represent the area shown in the upper right inset, used to measure some values of w, reported in the table. **(c)** Polynomial relation between the filling fraction ff and the thickness w of the walls. **(d)** Three nominal values of w/a (blue dots), specifically $w/a = 0.394$ (1), 0.44 (2) and 0.489 (3). The grey dots represent instead the w/a estimated from the SEM images of structures that differ for the values of a and of some other replica; the deviation from the nominal value of w/a, that should be the same for all a, is evident.

we report a variation of $w_{Nom} - w_{SEM} = \Delta w \approx 20.9$ nm (which is $\approx$ 10 nm smaller than the rough estimation of $\Delta w \approx 135$ nm given in the table of Fig.6.4b). As we will see in the next Sections, the minor wall thickness contributed to explain the spectral shift between theory and experiment.

6.2 Near-field detection of light transport regimes

The samples described in the previous section were analyzed with the SNOM in *illumination/collection* configuration (see Section 4.1.2). Fig.6.5a shows the top view SEM image of one of the investigated samples, with nominal lattice constant $a = 380$ nm and wall thickness $w = 0.44a$. The spatially resolved optical maps were recorded by scanning the probe tip over the sample at a fixed distance (few tens of nm), and this technique allows us to perform HSI, that is we collect a full spectrum of the photonic local density of states (LDOS) of a system for any spatial pixel of the near-field map. In Fig.6.5b is reported a typical PL spectrum acquired in one position of the HuD sample. We first evaluated the spatially averaged spectrum over a large area (8 µm × 8 µm, 100 nm/px spatial step) which smooths out the photonic resonances in the LDOS and gives back the PL spectrum of the embedded QDs, reported in orange in Fig.6.5b. By design the QDs emission is spectrally overlapped to modes at the lower PBG. Then, we calculated the PL enhancement spectrum at a fixed position by dividing the recorded near-field spectrum by the spectrum of the QDs. By doing this for every tip position during the SNOM scan, i.e. for every pixel of the map, it was possible to reconstruct the near-field spatial distribution of the PL enhancement (i.e. of the photonic LDOS) over a broad range of wavelengths (1165-1280) nm. In the near-field spectra collected at fixed tip positions, several resonances related to the modes of the system, are clearly visible. For example, in the spectrum of Fig.6.5b, many sharp peaks that are superimposed on the QDs emission occur, mostly at short wavelengths. In order to achieve an overall comprehension of these many peaks behaviors in the entire spectral range, in Fig.6.5c we show six collective maps (corresponding to the same six λ intervals of Fig.6.5b), in which we report the maximum PL enhancement measured in the spectral regions reported on the top of each map. In each map, every bright spot refers to the brightest mode (or sometimes the superposition of more modes) in that spatial region, within the selected spectral window. Each map is normalized to the maximum PL enhancement in the correspondent spectral window. We report an absolute maximum PL enhancement of the order of 20, which is double with respect to the typical enhancement factor obtained in ordinary random structures studied so far [70]. Interestingly, in these collective maps it is possible to observe that while at shorter wavelengths isolated and localized modes with high PL enhancement dominate, as the wavelength increases, the modes tend to be more and more delocalized all over the structure. Hence, as highlighted in the typical PL enhancement spectrum reported in Fig.6.6a, the experimental data clearly define three main spectral regions, according to what theory predicts: region 1 ($\approx$ (1100-1160) nm) is characterized by the effect of the PBG with no detected modes. The very first resonances appear around 1160 nm, showing strongly localized field profiles (similar to the one in Fig.6.2b); this feature is shared with

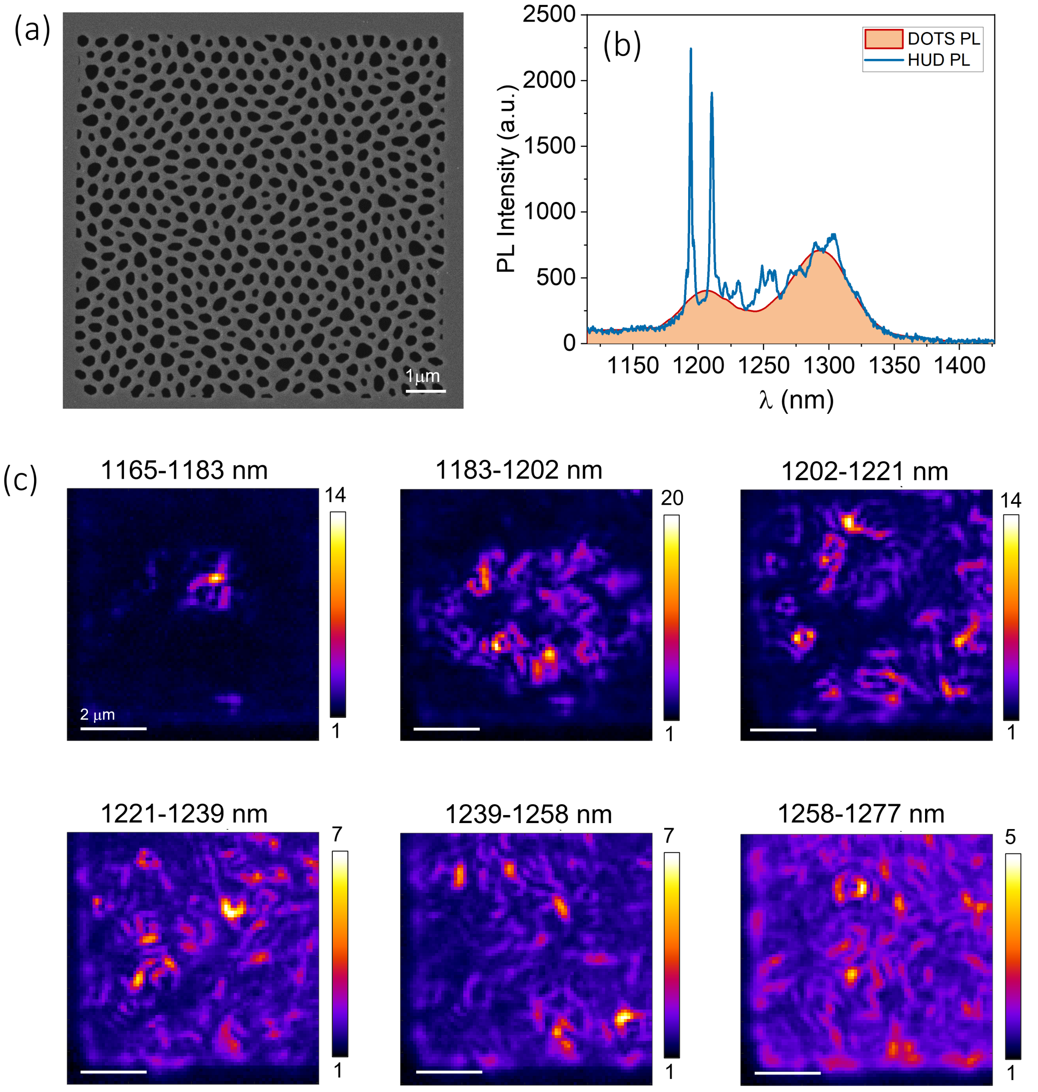

Figure 6.5. **(a)** SEM top view image of the structure, with $a = 380$nm and $w = 0.44a$. **(b)** Typical SNOM-PL spectrum (blue line) at a given tip position, and QDs-PL emission spectrum (orange). **(c)** Maps of the maximum PL enhancement in six spectral regions. Each map is normalized to the maximum PL enhancement in the correspondent spectral window. All white scalebars correspond to 2 µm.

all modes within region 2 ($\approx$ (1160-1195) nm). Then, increasing the wavelength, after a transition region ($\approx$ (1195-1225) nm), the modes show a delocalization over the whole structure (similar to the one in Fig.6.2a), and we named this region 3 ($\lambda > 1225$ nm). In Fig.6.6b (c) we report the SNOM PL enhancement map of a typical localized (delocalized) resonance at $\lambda = 1191$ nm ($\lambda = 1259$ nm). The two modes also differ for the PL enhancement, that is much more higher in the case of the localized mode. Notably, the PL signal is mostly localized into the dielectric, as predicted by simulations for the electric field intensity of modes below the band gap. Based on this experimental evidence, a rigorous statistical analysis was performed on the collected data in order to address the physics at the basis of the different features displayed by these spectral windows. Infact, near-field imaging gives direct access to the spatial extension of the HuD modes, allowing us to study the details of the transition between localized and delocalized modes near the dielectric band edge. In the next Sections we will go through the analytical methods employed to achieve this task.

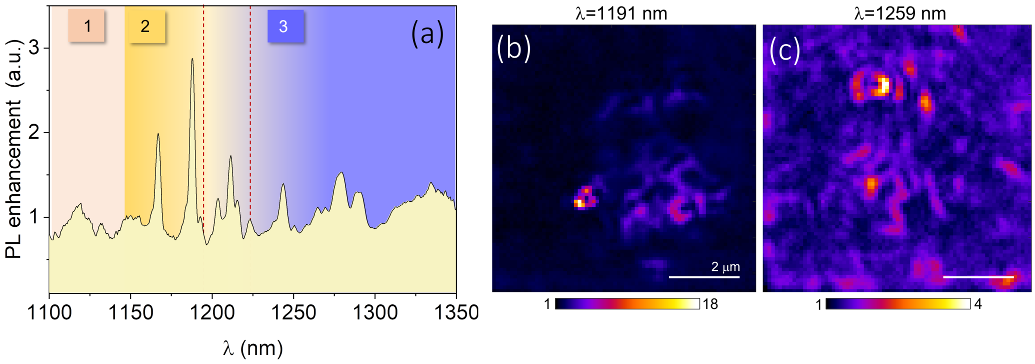

Figure 6.6. **(a)** Typical PL enhancement spectrum at a given tip position on a broad wavelength interval. Labels 1, 2 and 3 indicate the PBG spectral region and the spectral intervals in which localized (2) and delocalized (3) modes are detected, respectively. The transition spectral window between region 2 and 3 is indicated by red dashed lines. **(b)** SNOM PL enhancement map filtered around the central wavelength of a peak that belongs to region 2 ($\lambda = 1191$ nm), showing a localized mode with a PL enhancement factor of 18. **(c)** SNOM PL enhancement map filtered around the central wavelength of a peak that belongs to region 3 ($\lambda = 1259$ nm), showing a delocalized mode, with a PL enhancement factor of 4.

6.2.1 Evaluation of the modes spatial extension

In order to isolate the modes and calculate their statistical properties (like localization length and Q factors), given their high spatial and spectral density, we performed multi-Lorentzian peaks fits (from one to five peaks) on PL SNOM maps acquired with the 0.11 nm/px dispersion grating. In this Paragraph we want to explain the used fitting method and the key of interpretation of the results obtainable from this procedure. In order to do this, in Fig.6.7 we report an example of a three-Lorentzians fit performed on a triplet of HuD modes of the structure, located in the same spatial region and spectrally separated by 1-3 nm from each other.

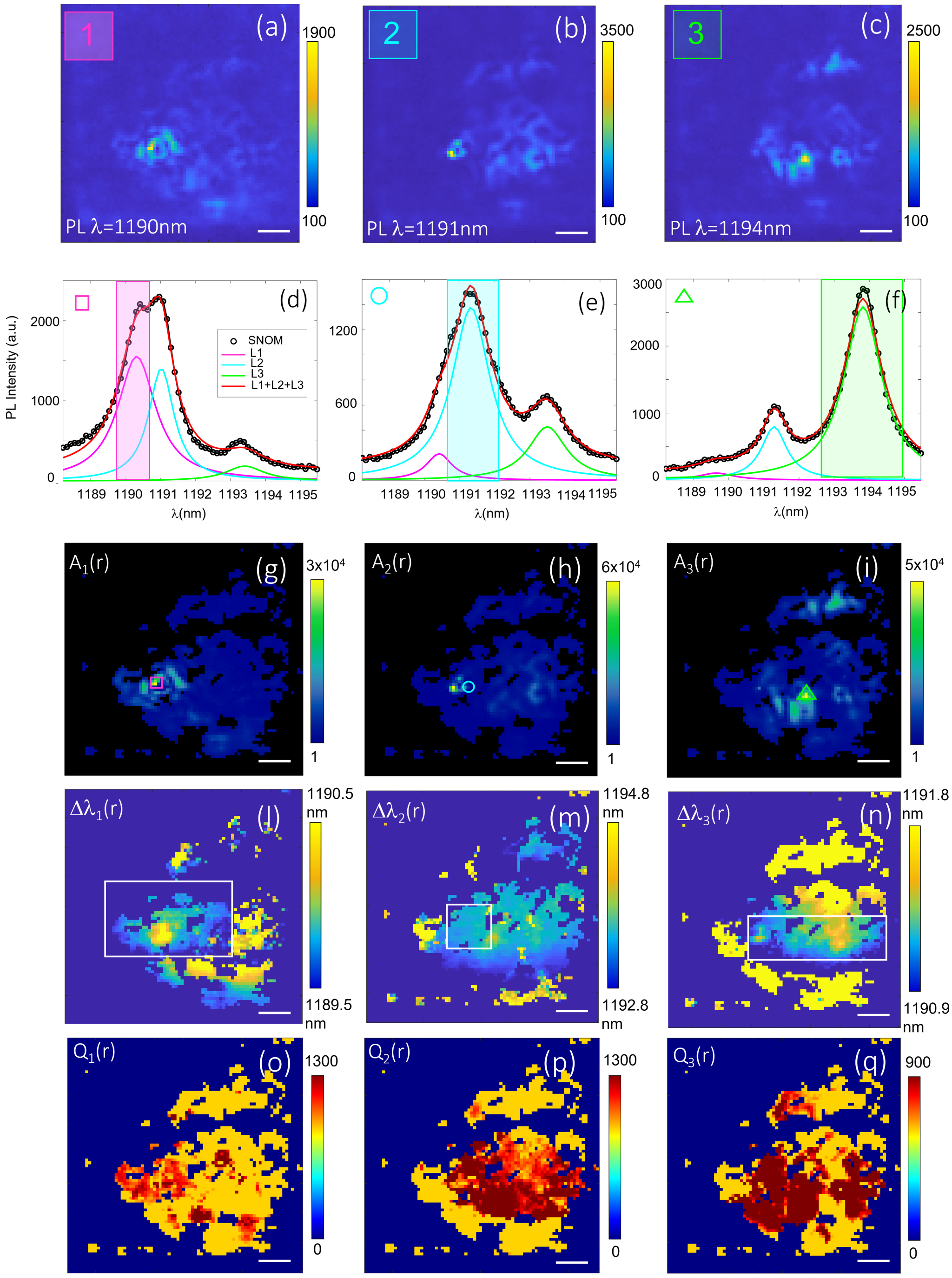

Figure 6.7. **(a)**, **(b)** and **(c)**: PL maps at the central wavelengths of modes 1, 2 and 3, respectively λ = 1190 nm, 1191 nm and 1194 nm. **(d)**, **(e)** and **(f)** The dashed dots are the PL data acquired in the points indicated by the symbols: magenta square (d), cyan circle (e) and green triangle (f). The fitted Lorentzian lines are represented by the magenta curve (L1), the cyan curve (L2) and the green curve (L3). The collective fit line L1+L2+L3 is indicated by the red lines. The colored bands in the three spectra are an indication of the spectral range in which each Lorentzian curve was fitted. **(g)**, **(h)** and **(i)** Fitted amplitude maps for the three modes. **(l)**, **(m)** and **(n)** Spectral shift maps; the white squares represent the area in which the fit is considered good. **(o)**, **(p)** and **(q)** Fitted Q maps.

We will refer to these three modes as mode 1 (magenta label), 2 (cyan label) and 3 (green label). Here and in the following, different scale colors are used for different maps.

The SNOM-PL maps acquired at the central wavelengths of the three peaks are shown in Fig.6.7a, b, c, respectively at $\lambda = 1190$ nm, 1191 nm and 1194 nm; the fit was executed for every pixel of the SNOM-PL map, applying different constraints (in terms of spectral range, spectral width, central wavelengths and amplitude) for the three peaks.

In Fig.6.7 d, e, f are reported three spectra relative to the fit of the three modes, that allowed to extract the fitted amplitude maps shown in Fig.6.7 g, h, i. Each PL spectrum (black dots) is acquired in the pixel indicated by the symbols of the amplitude maps (the magenta square for the spectrum of Fig.6.7d, the cyan circle for e and green triangle for f). In the graphs, along with the PL signal we can observe the Lorentzian fits (magenta, cyan and green for mode 1, 2 and 3), together with the sum of the three curves (red line). The colored bands in the graphs indicate the spectral regions to which the single mode fit is constrained. As the signal is below a fixed threshold, the fit is not performed and this is visualized in the black areas of the fitted amplitude maps (Fig.6.7 g, h, i). These maps, that show submicrometric details within the spectral resolution of the measurements (given by the tip dimension ≈ 200 nm), can be here considered as actual spatial maps of the electric field intensity of the modes.

But how do we evaluate the reliability of the fits? Firstly, by checking the fitted spectra on the whole area, then we consider two other results that can be extracted from the fit: the central wavelengths λ and the spectral broadening. Infact, we are able to reconstruct the spatial distributions of the fitted central wavelength $\lambda(r)$ (Fig.6.7 l, m, n), and of the Q factor (Fig.6.7 o, p, q). We reported a maximum Q factor of 1300 for the first two modes, and 900 for the third.

Based on the work by F. Intonti *et al* [160], we know that the dielectric SNOM tip induces a local perturbation of the modes in photonic crystal cavities; this allowed to recover important details on the LDOS of such cavities that were otherwise lost in the PL maps. This states a criterium based on the uniformity of the spectral shift $\Delta\lambda$ and the Q factor maps that allowed us to exclude some of the fitted areas. Starting from the point of maximum PL intensity, where $\Delta\lambda$ is maximum and Q is minimum (due to the tip perturbation), we considered the fit reliable in the areas highlighted by the white rectangles in the maps of Figs.6.7 l, m, n.

This reasoning was applied to several other modes in the HuD structure; then, in order to perform a statistical analysis on the overall spatial localization, we exploited the fitted amplitude maps as an evaluation of $|E(r)|^2$ for every resonance; infact, $|E(r)|^2$ is a quantity that, as we will see in the next Sections, is strictly related to the spatial localization of modes.

6.2.2 FEM simulations on the HuD structure

Numerical simulations are important tools that allow to validate and fully comprehend the experimental results. We now describe how we modelled the problem with Finite Element Method simulations, and how this allowed to comprehend the modes spectral dependence with respect to structural parameters like inter-membrane distance d, membrane thickness t and wall thickness w. The combination of this sistematic study with the SEM analysis reported in Section 6.1.2 allowed to confirm a clear interpretation of the resonances experimentally detected. FEM simulations (with the commercial software Comsol) were performed at first by pattering the membranes with the theoretical design (reported in Fig.6.1a of Section 6.1.1, employed for fabricating the sample). The system of two parallel membranes of thickness t = 130 nm and inter-membrane distance d =105 nm was modelled by simulating half of the system (i.e. the upper membrane and an air gap of $d/2$) by imposing symmetry conditions in order to save computational time. A sketch of the simulation system is shown in Fig.6.8a. In fact, it was recently demonstrated that, due to the symmetry of the problem, the photonic modes of two parallel membranes couple as they are neared. Each mode of both the membranes split into symmetric (S) and antisymmetric solutions (AS), whose spectral separation increase as the intermembrane distance diminishes. An example of this phenomenon is shown in Fig.6.8b in the case of a double membrane L3 cavity. As explained in Section 4.3.3, due to the parity with respect to the plane separating the two membranes, A and AS modes can be respectively detected whenever a Perfectly Magnetic Conductor (PMC) or Perfect Electric Conductor (PEC) is imposed on that plane. In our case, since we experimentally detect AS conditions (due to the spectral location of the QDs), we imposed a PEC condition. In Figs.6.8 c-h we report three examples of HuD modes detected in the experiment and in the simulations. Fig.6.8 c, e, g (on the left) display the SNOM PL maps acquired at the central wavelengths of the peaks of the selected modes, respectively $\lambda = 1203$ nm, $\lambda = 1204$ nm and $\lambda = 1219$ nm; on the right column (Fig.6.8 d, f, h), we reported the FEM maps of the electric field intensity of the modes, that are found at $\lambda = 1225$ nm, $\lambda = 1227$ nm and $\lambda = 1236$ nm. From these images, it is evident the very good agreement between the near-field and the theoretical spatial profiles of the modes, but also a shift between the theoretical maps and the SNOM PL maps of the order of $\approx$ 20-30 nm (deduced from a global analysis). In order to explain this, and to study the dependence of the HuD modes wavelength with respect to the width of the dielectric veins w, the same FEM simulation was repeated by changing one parameter at a time. We found roughly $\Delta\lambda/\Delta w = 1.5$. Thanks to these estimations, and to the SEM analysis that allowed to determine that the wall thickness of the sample resulted $\approx$ 20 nm thinner than the nominal value, we were able to explain the shift between the wavelengths of the modes in theory and experiment. Specifically, we concluded that $\Delta w \approx 20$ nm determines a spectral shift of about 30 nm. In order to decrease this discrepancy between theory and experiment we extracted a more realistic design from the SEM top view image of our sample, and simulated the double membrane system with this pattern. The nominal design and the "SEM-design" are compared in Fig.6.8i and l. Notably, we observe that the actual fabricated sample is slightly bigger than the nominal structure, and the smallest hole inside the four-fold topological defect was

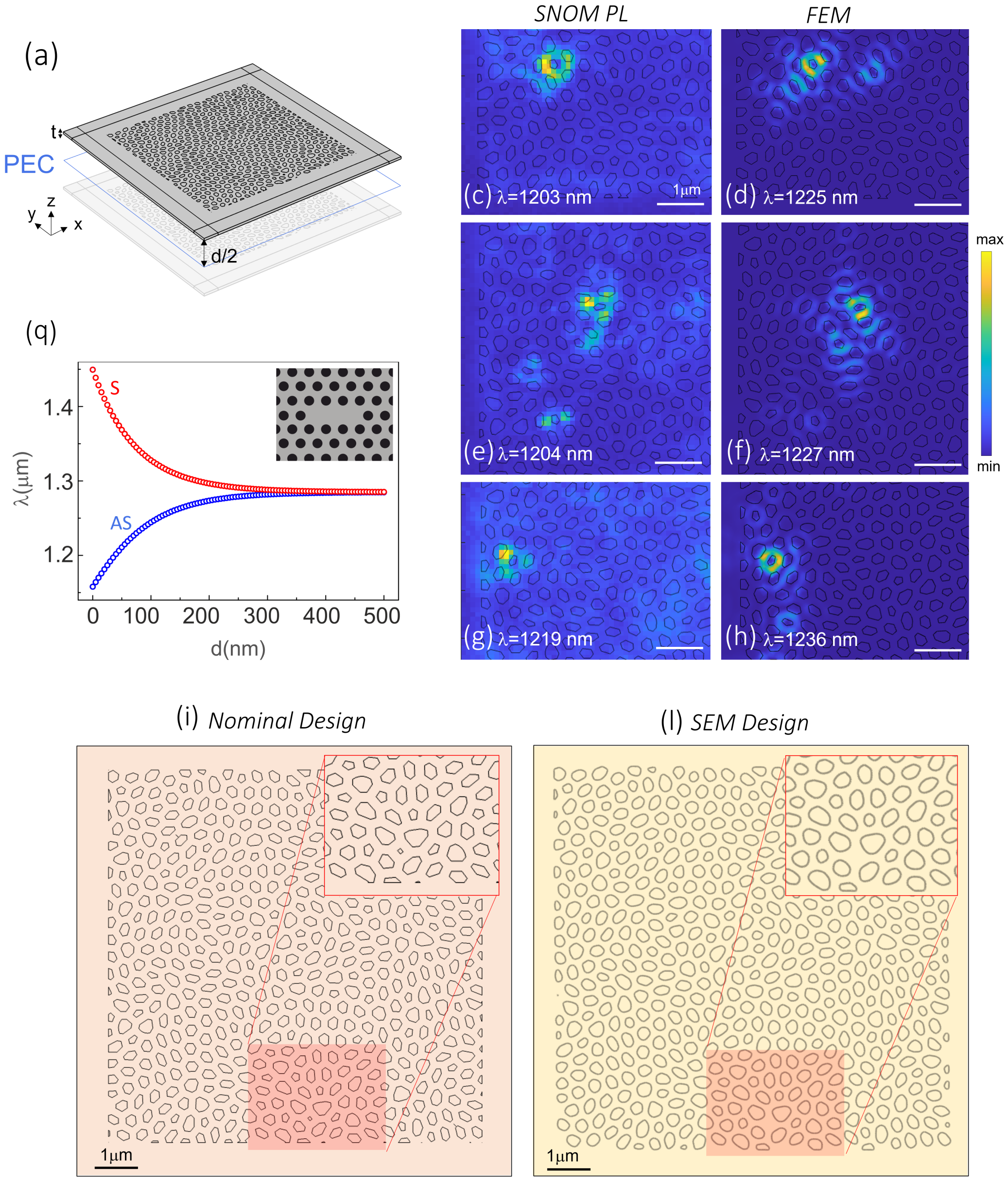

Figure 6.8. **(a)** Sketch of the double membrane system modelled in the FEM simulations. **(b)** Spectral splitting of the fundamental mode of an L3 double membrane photonic cavity into symmetric (S) and antisymmetric (AS) modes with respect to the inter-membrane distance. **(c)-(e)-(g)** Typical examples of SNOM-PL maps in which it is possible to recognize the spatial profile of the electric field intensity of modes. The correspondent FEM maps of $|E|^2$ are reported in **(d)-(f)-(h)**. All scalebars correspond to 1µm. **(i)** Nominal design; **(l)** SEM-design.

not fabricated (as highlighted by the insets). Moreover, the SEM-design takes into account of the smaller value of w. For this reason, only the FEM simulations on the SEM-design are presented in the final results, where the spectral shift between theory and experiment that is left is ≈ 15 nm, to be attributed to uncertainties on the real structural parameters of the real sample like t and d.

Graphic Extrapolation of the SEM-design

In Fig.6.9 are resumed the main steps of the process through which we extracted the SEM-design for FEM simulations starting from the SEM image (Fig.6.9a). The first step is done by converting the image into a binary image (black and white) with the free software ImageJ, shown in Fig.6.9b. Although it is possible to convert an image in png format into a CAD file in order to model the system in the simulation software, the presence of the pixels would demand a very high computational effort in order to run the calculations. The inset of Fig.6.9b displays a zoom in which it is possible to observe how the domains of the holes are strongly affected by the pixels. For these reasons, we converted the png binary image into a vectorial format, by using the free graphic editor Inkscape, and a representation of this further passage is shown in Fig.6.9c. It was then possible to convert the vectorial image into a CAD file with smooth lines defining the separation between air and dielectric. This last conversion was performed with the commercial software LinkCAD.

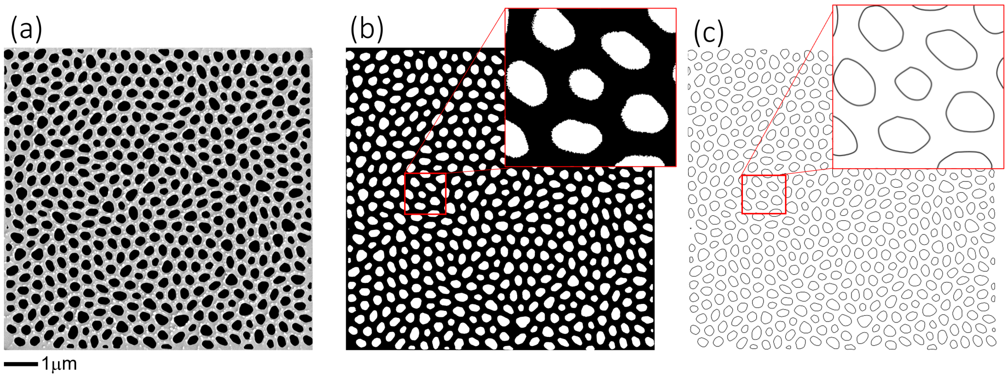

Figure 6.9. **(a)** SEM top view image of the sample that was used to create the "SEM-design" used in FEM simulations. **(b)** Binary image of (a). **(c)** Representation of the vectorial image that allowed to eliminate the presence of the pixels.

6.2.3 Statistical description of the sample

A relevant aspect in a statistical analysis and the comprehension of potential performances of a photonic structure, is the evaluation of the areal density of modes. There are several methods that have been adopted in previous works on disordered photonic structures to address the number of modes; here, we adopt the procedure of Balestri *et al* [70], carried out on photonic random structures, that typically exhibit very high spatial density of modes. We performed a 6 μm × 6 μm SNOM scan (at step of 50 nm/px). The correspondent PL enhancement map (evaluated in the

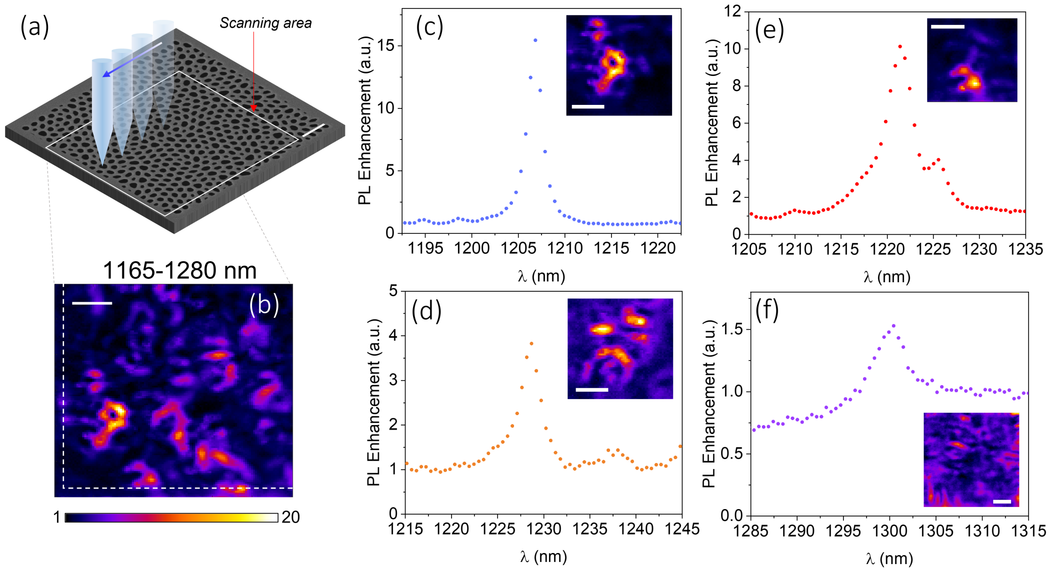

Figure 6.10. **(a)** Sketch of the probe scanning the sample; the white square represents the scanned area (6 µm × 6 µm). **(b)** PL enhancement map in the spectral window (1165-1280) nm. **(c)** Typical examples of spatial profiles and spectral line shapes of four HuD modes. The white scales correspond to 1 µm.

entire spectral range 1165-1280 nm) is reported in the bottom part of Fig.6.10a, that we can compare with the SEM top view of the sample in order to have an idea of the scanned area. Then we evaluate the integral over space and wavelength of the enhancement $E(\boldsymbol{r}, \lambda)$, and in order to exclude noise and very leaky modes we put to zero the points in which $E(\boldsymbol{r}, \lambda) < 1$ (due to the deviations in the normalization of the PL signal to the QDs PL). Assuming $E(\boldsymbol{r}, \lambda)$ is a linear superposition of modes of maximum enhancement E_{max}, area S and spectral broadening $\Delta\lambda$, we have

$$\langle E \rangle = \int d^2 r \int d\lambda E(\boldsymbol{r}, \lambda) = \langle N \rangle \langle S \rangle \langle \Delta\lambda \rangle \tag{6.1}$$

Where $\langle S \rangle$ is the averaged mode area and $\langle \Delta\lambda \rangle$ is the averaged spectral broadening (over N modes). Hence

$$N \approx \frac{\langle E \rangle}{\langle S \rangle \langle \Delta\lambda \rangle \langle E_{max} \rangle} \tag{6.2}$$

We evaluate $\langle S \rangle$ and $\langle \Delta\lambda \rangle$ from the analysis of isolated modes; in fact, at this point it is possible to extract the spatial distribution of the modes. In Figs.6.10c-e we report the PL enhancement spectra of three typical HuD localized modes (belonging to region 2), and the relative insets shows the PL enhancement spatial profile filtered at the central wavelength of each peak. As explained above, in agreement with theoretical prediction (see Section 6.1.1), these localized modes (similar to the one in Fig.6.2b) display higher Q factors and lower localization length, and to them will be dedicated Section 6.3. Differently, Fig.6.10f is relative to a more spectrally broadened mode (belonging to region 3), delocalized over the whole structure. This resonance, at a higher wavelength with respect to the others, shown in Fig.6.10, is far from the PBG and therefore carries other types of information as explained in

Section 6.1.1 (Fig.6.2a). In order to evaluate the number density of modes, we treat modes from region 2 and 3 differently. Localized modes are estimated to show a mean spatial extension of $\langle S \rangle \approx 2.5 \mu m^2$ and a mean spectral width of $\langle \Delta\lambda \rangle \approx 2.6$ nm. In order to obtain a fair result, we excluded the modes at the border of the structure (dashed white lines in Fig.6.10b), that are subjected to great losses in the dielectric and therefore invalidate the analysis due to their spectral broadening. Regarding the delocalized modes, we found a mean spectral broadening of $\langle \Delta\lambda \rangle \approx 4$ nm, and we assumed a spatial extension of 8 µm × 8 µm (corresponding to the whole structure). A last passage consists in normalizing the total number of modes to the entire area of the sample, since we have counted the modes after a scan of 6 µm × 6 µm, while the actual sample area is 8 µm × 8 µm. Assuming a uniform density of modes, we multiplied N by a factor 1.6 (the ratio between the total area and the scanned area).

The results obtained with this analysis are reported in Fig.6.11a together with the expected number of modes predicted by FEM simulations. In Fig.6.11a we show that the number of modes determined experimentally (red diamonds) is in good agreement with the theoretical predictions from FEM simulations (purple diamonds). The wavelength axis, that reports the broadest spectral range achieved in the measurements, is the same for both data for simplicity of comparison (shifted by the opportune value $\Delta\lambda \approx 15$ nm). The transition spectral window between region 2 and 3 displays the highest number of modes.

We can also quantify the spatial location of the modes with a more precise method. Through this method we are experimentally able to detect different regimes of light transport, quantifying what has been observed at the beginning of the Section (Fig.6.5 and Fig.6.6). The spatial localization of the modes can be indicated by calculating the Inverse Participation Ratio (IPR) [161, 162, 163], which is defined as

$$IPR = \frac{\int |E(r)|^4 dr}{\left(\int |E(r)|^2 dr\right)^2} Vtot \tag{6.3}$$

where $|E(r)|^2$ is the intensity distribution of the electric field in the eigenstate and V_{tot} is the total volume of the system. Values of IPR close to one indicate the electric field intensity being constant throughout the system volume, while higher values are associated with the intensity confined to a small volume. In Fig.6.11b we show the trend of the theoretical and experimental calculation of the HuD modes with respect to the wavelength; the blue dots represent the values obtained by Finite Element Method (FEM) simulations on the SEM-design, while the red dots are relative to the results extracted from the SNOM experimental data with the multi-Lorentzians fit method (more technical details on the fitted values are reported at the end of the Section). The error bars come from the propagation ΔIPR, estimated as the maximum deviation between the minimum and maximum acceptable values of the IPR obtained by changing the threshold of the fits. Note that, as mentioned above, there is a wavelength shift of 15 nm between measurements and simulations, which is to be attributed to uncertainties on the structural parameters of the real sample. For this reason the experimental (bottom of the graph) and theoretical (top of the graph) λ axis are different. It is also worth noting that a value of IPR of the order of 13 is considered as the threshold (represented by the horizontal green dashed

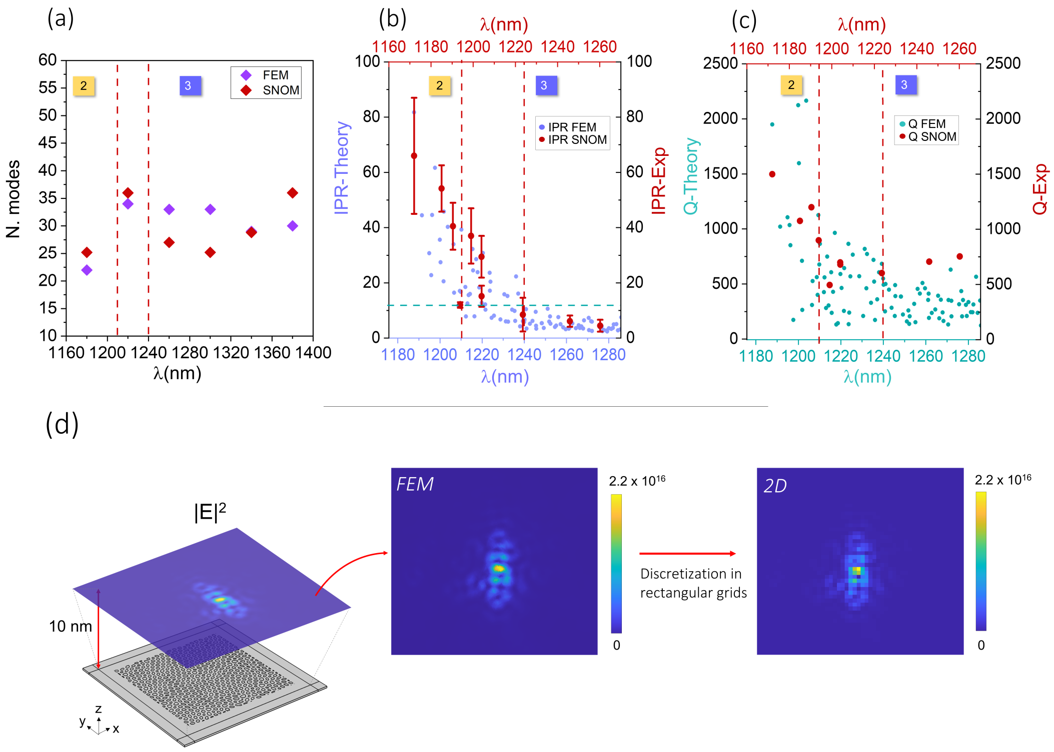

Figure 6.11. **(a)** Number of modes for different spectral regions calculated with FEM simulations (purple diamonds), and extracted from the SNOM measurements (red diamonds). **(b)** Evolution of IPR with respect to the wavelength as a description of light localization for experimental values (red dots, calculated by using the fitted amplitude maps of the selected modes) and eigenstates of the SEM-design structure (blue dots) obtained with FEM simulations. The green dashed horizontal line indicates the threshold of $IPR = 13$, while the red dashed vertical lines highlight the transition window from region 2 to region 3. The error bars in the experimental data are estimated as the maximum deviation between the minimum and maximum acceptable values of the IPR obtained by changing the threshold of the fits. **(c)** Theoretical Qs (green dots) and experimental Qs (red dots) calculated from fit with respect to the wavelength. No error bars are reported since, because of the spectral resolution (0.11nm/px), they wouldn't be visible in the graph. **(d)** Sketch of the process that leads to the correction factor between theoretical and experimental IPR; we extract from the FEM simulation a near-field map of the electric field intensity of the mode at plane 10 nm above the membrane (tetrahedral mesh), then we discretize it in a square grid, and finally calculate the IPR in 2D from FEM simulations with the same procedure adopted with the SNOM maps (Eq 6.6).

line in Fig.6.11b) above which the modes become localized, and it corresponds to a localization length [164] of the order of 2 µm. Following this threshold, we demonstrate the presence of two regions with only localized (2) or delocalized (3) modes, as well as a spectral window between the two, highlighted by the vertical red dashed lines, displaying modes with IPR above and below 13. This region is very interesting, likely describing the coexistence between localization and diffusive transport. The theoretical values are in good agreement with the experimental data. An interesting theoretical prediction is that HuD modes may have high quality factors when localized and close to the PBG, while the Q decreases for extended modes far from the band edge. This trend is well represented in Fig.6.11c, in which we show the theoretical Q values (green dots), together with the experimental fitted values (red dots) obtained by near-field PL. The experimentally detected resonances are characterized by quality factors ranging from 1500 to 500 and reproduce well the theoretical trend. In order to obtain a full characterization of the physical properties of HuD modes, we address the relation between cavity mode volume and the rate of spontaneous emission [15] by evaluating the modal volume V following the definition based on quasi-normal modes theory [165]. By considering the HuD modes as a set of n modes with normalized complex electric fields $\tilde{E}_n(r)$ and complex frequencies:

$$V = \frac{I}{2\epsilon_0 \max\left(\epsilon(r)|E(r)|^2\right)} \tag{6.4}$$

where I is the normalization condition of the quasi-normal modes:

$$\int\int\int_V = \left[\epsilon_0\epsilon(r)\tilde{E}_n^2(r) - \mu_0\tilde{H}_n^2(r)\right] \tag{6.5}$$

We obtained an experimental value of $V \approx 0.06$ µm^3 for the most localized mode at the PBG edge, which is comparable with the modal volume of an L3 cavity, $V \approx$0.07 µm^3 [9]. Clearly, HuD modes located in the band gap vicinity are characterized by a high ratio Q/V (of 25000 µm^{-3}), suggesting their exploitation for Quantum Electrodynamics (QED) effects [166, 167]. This topic will be covered in the next Section (6.3). By putting together all the information in Fig.6.11a, b and c, we combine relevant aspects for applications such as areal density and localization properties; interstingly, we find that there are more than 50 HuD modes with high Q/V in a spectral region of 80 nm; this is much higher when compared to photonic crystal cavities, where in the same sample area usually only one cavity (with two or three modes) is designed. This result clearly shows how HuD photonic devices display the advantages of both ordered and disordered systems.

A final technical question should be addressed, regarding how we were able to extract the IPR and V values from the fits. Infact, the experimental IPR (or V) is associated with the 2D imaging of the field intensity by SNOM, while the theoretical IPR is evaluated from a 3D reconstruction of the mode profiles. For this reason, from FEM simulations we have calculated a scaling factor of 1.5 between the two IPRs, and rescaled the theoretical IPR values in Fig.6.11b by this factor 1.5. Let's consider a single mode detected in the SNOM scan, for example the very first mode at the lower PBG edge. After performing the multi-Lorentzian peaks fit we are able to isolate it and extract the fitted amplitude map $A(r)$, that can be considered as an evaluation of $|E(r)|^2$ in the two dimensions of the SNOM map. Therefore, adapting Eq.6.3 we have:

$$IPR = \frac{\sum_{i=1}^{n} A_i^2 dXdY}{(\sum_{i=1}^{n} A_i dXdY)^2} S \tag{6.6}$$

where n is the number of pixels in the map, and $dXdY$ is the area of one pixel (0.01 µm^2 for a 100 nm/px scan). S is the total area of the system, in our case 8 µm × 8 µm. For the considered mode we obtain an experimental value of $IPR = 99$. An analogue method was used to calculate the modal volume V, adapting Eq.6.4 by considering the fitted amplitude map $A(r)$ as an evaluation of $|E(r)|^2$. Differently, from FEM simulations, in which the integrals in the IPR formula are evaluated on the whole volume in 3D, we get $IPR = 123$. Then, in order to obtain a correction factor between 2D and 3D we extract from the FEM simulation a near-field map of the electric field intensity of the mode at plane 10 nm above the membrane; the process is schematized in Fig.6.11d. By discretizing this map in a certain number of squared pixels (note that in Comsol the used mesh is tetrahedral), we calculate the IPR in two dimensions with the same routine used for the experimental data, obtaining a value of 80.3. The reconstructed 2D FEM map is on the right part of Fig.6.11d. Therefore, the correction factor used to the 3D FEM IPR values in order to compare them with the experimental data is $123/80 \approx 1.5$.

6.3 HuD band-edge modes for QED applications

The interaction of light with matter is the foundation for the fundamental processes of emission, absorption, transmission, and reflection. The ability to control how light interacts with matter is therefore the key to achieving technological breakthroughs across a wide range of photonic and optoelectronic applications. Optical localization in strongly disordered photonic media is an attractive topic for proposing novel cavity-like structures. Light interference can produce random modes confined within small volumes, whose spatial distribution in the near-field is predicted to show hot spots at the nanoscale. Random photonic modes have been investigated for their basic physical insights, such as Anderson localization, and recently several applications have been envisioned in the field of renewable energies, telecommunications, and QED. An advantage for optoelectronics and quantum source integration offered by random systems is their high density of photonic modes, which span a large range of spectral resonances and spatial distributions, thus increasing the probability to match randomly distributed emitters. However, typical random modes of photonic disordered structures recently studied [10, 134], display Q factors not higher than 200. On the other hand, photonic crystal cavities, that have been engineered and studied in the most various ways in the last decades, and have been considered the most efficient building blocks for QED applications due to their high Q/V values [167], are often limited by the low spatial and spectral density of modes, and by their strong sensitivity to unavoidable fabrication induced disorder. In this work, we aim at overcoming these limitations by proposing a novel class of photonic modes arising at the PBG of a HuD structure, capable of combining the advantages of both ordered and disordered systems. An unexpected result emerges from our analysis: we demonstrate, theoretically and experimentally, that these modes exhibit a higher resistance with respect to fabrication induced disorder and local perturbations, than the one found in typical random modes. They can therefore be proposed as a promising platform for QED and optoelectronic applications.

6.3.1 Near-field HSI for detection of modes at PBG edges

Thanks to the analysis presented in the previous Section, we were able to experimentally prove the theoretical predictions regarding HuD modes arising at the PBG edges. In particular, we showed (in Fig.6.11d-e) how the modes at lower PBG edge display a lower localization length and a higher Q factor with respect to the ones at lower frequencies. This was obtained by scanning a HuD structure (Fig.6.12a) with the SNOM in *illumination/collection* configuration. To further explore the assessment of the suitability of HuD for QED effects, we exploit the Hyper Spectral Imaging (HSI) technique as a powerful tool to obtain, for every peak of a spectrum, the corresponding spatial profile. In order to present a comprehensive picture of the collective mode distributions, we report a map of the maximum PL enhancement measured at each SNOM tip position within a broad spectral region (1165-1280) nm in Fig.6.12b. The map is obtained after a 8 µm × 8 µm SNOM scan with 100 nm/px spatial step. We note that this map is neither a single-mode map, nor a map

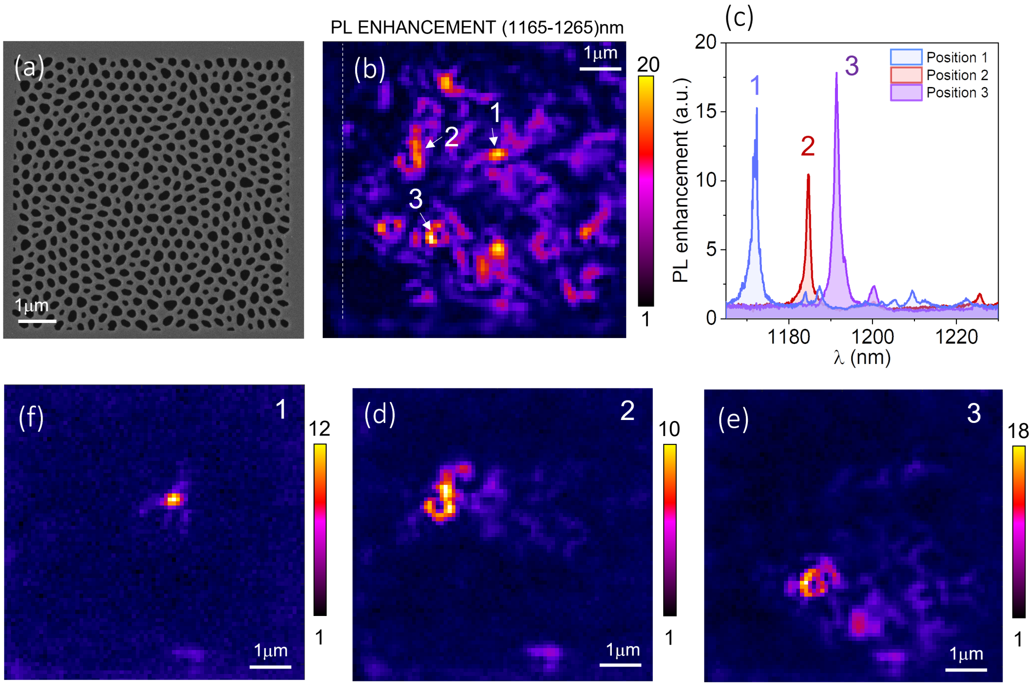

Figure 6.12. **(a)** SEM top view image of the structure, with $a = 380$nm and $w = 0.46a$. **(b)** Map of the maximum PL enhancement in the spectral region (1165-1265) nm, extracted from a SNOM PL map of 8 µm × 8 µm, with a scanning step of 100 nm/px. 1, 2 and 3 indicates the positions where the blue, red and purple spectra, reported in **(c)**, were acquired. **(d)**. **(e)** and **(f)** show the PL enhancement maps filtered around the central wavelengths of peaks 1 and 2, 3, i.e. $\lambda = 1172$ nm, $\lambda = 1184.7$ nm and $\lambda = 1191.4$ nm.

at a single emission frequency: it is a collective map, where each bright spot refers to the brightest mode (or superposition of modes) in that spatial region, within the selected spectral window. Therefore, it can be used as an indication of the position of the localized modes. We observe many modes distributed over the whole patterned area, indicating there is a high spatial density of modes (as it has been confirmed in Fig.6.5b). Most of these modes exhibit a PL enhancement of the order of 20. Fig.6.12b display three of the many sharp resonances found in the structure, specifically acquired in three different positions of the map (1 in blue, 2 in red and 3 in purple). These peaks reveal a Q factor of 1000, 600 and 1500 respectively (for positions 1, 2 and 3), and can be easily spectrally isolated. The correspondent spatial profiles are reported in Figs.6.12 d, e and f (in order of position label in the map), filtered around $\lambda = 1172$ nm, $\lambda = 1184.7$ nm and $\lambda = 1191.4$ nm, denoting a modal volume of 0.06 μm^3 for the first two modes (1 and 2), and 0.08 μm^3 for mode 3, respectively. Interestingly, the mode in Figs.6.12d is the first mode appearing at the PBG after the topological defect (see Fig.6.2b and c). The high Q/V ratio, as well as the large areal density displayed by HuD resonances near the PBG edge make them appealing as a promising platform for QED applications.

6.3.2 Tests of modes resistance to perturbation

Even if Maxwell's Equations can solve exactly any dielectric problem, in real random structures the measured modes usually show large deviations from the nominal design due to unavoidable fabrication imperfections; as a consequence, it is almost impossible to predict where the photons localization will occur in a given sample. The aspect of predictability of photonic modes motivated an entire field of optoelectronic research whose aim has been to make the deterministic control of random resonances possible on top of a given unpredictable spatial distribution. One method of tuning modes and quantifying their response to local disorder is nano-oxidation or infiltration with dielectric liquids in the air pores. In the work by Balestri et al. [134], the tuning of a single random mode under the modification of the dielectric constant of a single air pore, near to the maximum electric field intensity, has been studied. The results are resumed for comparison purposes in the upper panel of Fig.6.13. In Fig.6.13a is reported the simulated random pattern, and in blue is highlighted the pore whose index of refraction has been changed for tuning, from $n_{pore} = 1$ (standard case) to $n_{pore} = 3$ at 0.5 steps. The simulated results of the perturbation procedure are reported for a single mode in graph Fig.6.13b, where it is shown how the central wavelength and the Q factor of the mode are affected for the different values of n_{pore}. The data suggest that a variation of the index of refraction of the pore n_{pore} from $n_{pore} = 1$ (air) to $n_{pore} = 3$ induces a spectral shift of 20 nm of the mode; moreover, by looking at the simulated electric field intensity spatial distribution of the selected random mode for $n_{pore} = 1$ and $n_{pore} = 3$ it is visible a strong alteration of its spatial profile.

In order to quantify the robustness of HuD modes with respect to disorder, we apply the same kind of perturbation to the first mode at the lower PBG edge (i.e. band 499, see Section 6.1.1) through FEM simulations. We will refer to this mode as "mode α". In Fig.6.13e is reported the simulated map of the electric field intensity of mode α. A sketch of the design with the infiltrated pore is shown in Fig.6.13f (also highlighted in Fig.e with the red circle); we choose a hole sufficiently big and near the point of electric field maximum intensity. We change the index of refraction of the selected pore from $n_{pore} = 1$ and $n_{pore} = 3$ at 0.5 steps. We find a spectral shift from the unperturbed case to n_{pore}= 3 of 6 nm (Fig.6.13g), less than the half of the shift displayed by the random mode. Strikingly, the spatial profile of the mode stays almost unvaried, as it can be observed in the maps of Fig.6.13h. Differently from the random mode however, we can state that we are dealing with the same mode even in the case of a strong increase in the refractive index of the pore.

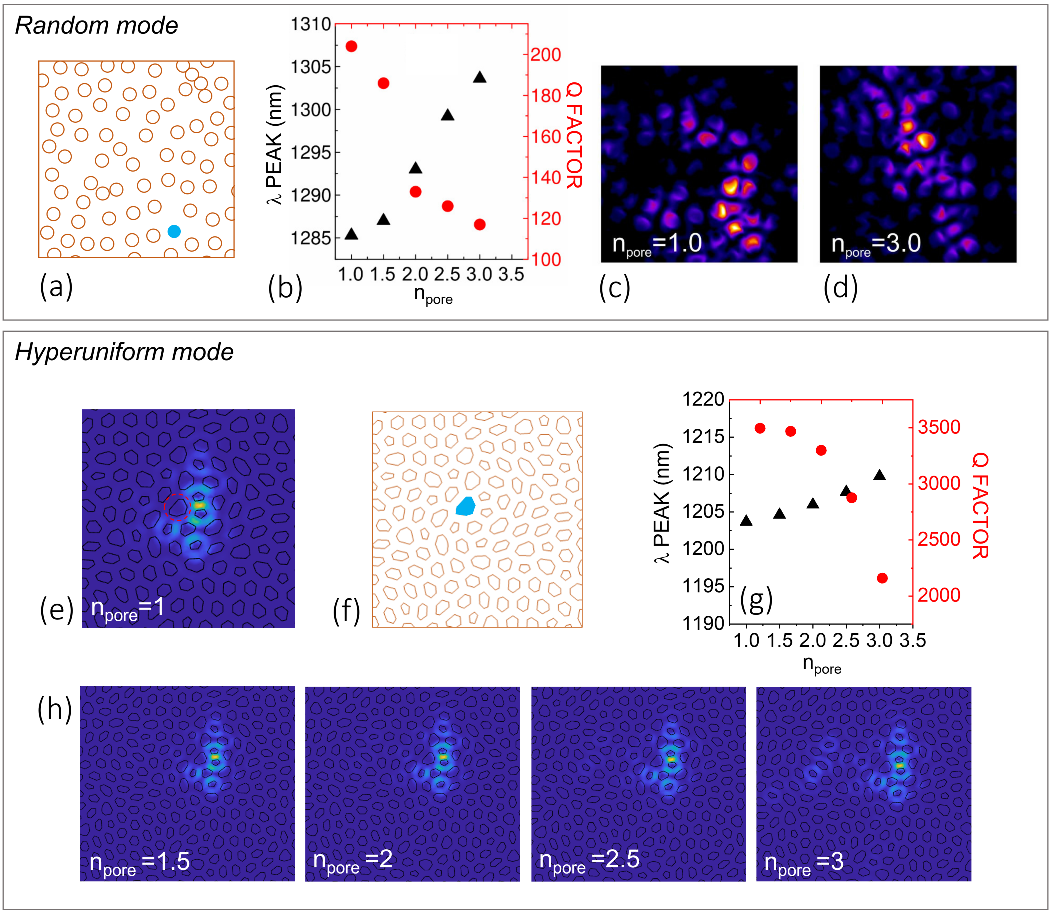

Figure 6.13. **(a)** Sketch of the simulated random pattern; the infiltrated pore is highlighted in blue. **(b)** Summary of the peak position and Q factor of the resonances as a function n_{pore}. **(c)** Spatial distribution of the electric field intensity of the considered random mode for n_{pore}=1 and n_{pore}=3 in **(d)**. All the upper panel is reprinted from SI of [70]. **(e)** FEM map of the electric field intensity of mode α; the red circle highlights the infiltrated pore. **(f)** Sketch of the simulated Hud pattern; the infiltrated pore is highlighted in blue. **(g)** Summary of the peak position and Q factor of the resonances as a function n_{pore}. **(h)** Spatial distributions of the electric field intensity of the considered mode for different values of n_{pore}.

The simulations on the SEM-design presented in Section 6.2.2 can be brought up as a final theoretical argument for the HuD modes resilience to disorder. Infact, by simulating a pattern extracted from the SEM image, it is correct to say that we are realistically taking into account of the smoothing of the corners in the air holes and the thinner wall thickness of the network, all effects generated during the fabrication process. Hence, the insertion of disorder in the simulations, not only managed to increase the convergence between theory and experiment, but also confirmed a robust possibility of reproducing the light localization of a large amount of modes in the HuD system. In order to underline this concept, we show the comparison between the FEM map of the electric field intensity of mode α obtained by simulating the nominal design (Fig.6.14a) and the SEM design (Fig.6.14b), respectively at λ =1203.7 nm and λ =1187.0 nm. These are also compared with the SNOM fitted amplitude map (Fig.6.14c), which agrees well with the theoretical predictions; notably, by overlapping the optical fitted map with the SNOM topography, we observe that the electric field is mainly located in the dielectric region (as predicted by theory regarding modes at the lower PBG edge), and the maximum intensity hotspot location is nicely reproduced. On the right, in Fig.6.14d, we report the PL spectrum acquired in the point of maximum intensity of mode α (blue dots), together with the Lorentzian fit (red line) that allowed to reconstruct the map in c. The spectral gap between the wavelength of mode α obtained by simulating the nominal design and the experimental one, is mainly due to the fact that the sample resulted bigger and the dielectric walls resulted thinner (as explained in Section 6.1.2). By simulating the SEM-design, we obtain a corresponding resonance that is shifted towards the experimental resonance. As specified before, the spectral shift of 16 nm that remains between theory and experiment can be attributed to other factors, like the rough estimation of the slab thickness and inter-membrane dis-

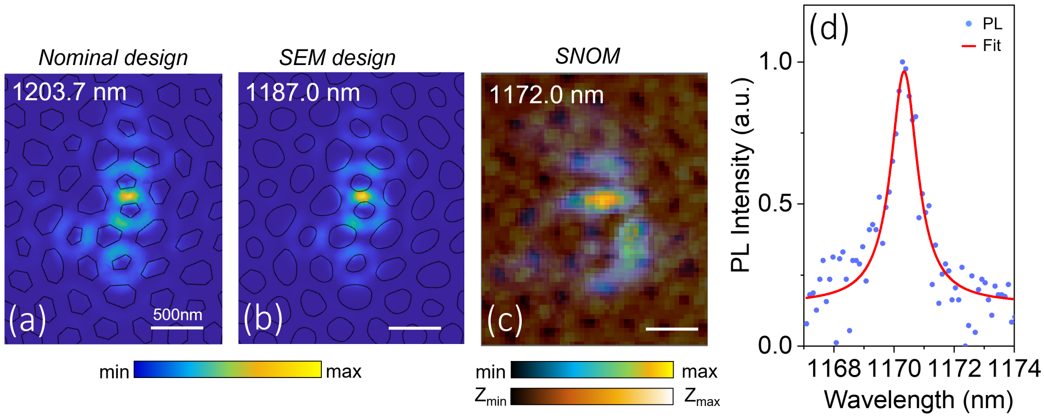

Figure 6.14. FEM Electric field intensity map of mode α obtained from the simulation of a double membrane system patterned with the nominal design **(a)** and the SEM-design **(b)**. **(c)** Fitted amplitude map of mode α, overlapping the SNOM topography. The two color bars are respectively related to the map of the fitted amplitude and the topography. In the first, yellow corresponds to the maximum amplitude, and black to the minimum but it is not visible due to the transparency. In the second, black (white) corresponds to the minimum (maximum) z position of the tip, and this is why the holes are in black. **(d)** PL spectrum (blue dots) acquired in the position of the tip corresponding to the maximum intensity of mode α, fitted with a one-Lorentzian function (red line).

tance extrapolated from the SEM images, and the approximation of the dielectric constant. More importantly however, despite the smoothing of the holes and the slightly altered morphology of the network, the field profile withstands and preserve the most important features that characterize its spatial footprint - i.e. unaltered intensity hotspots positions and spatial localization over few cells from the center. Therefore, it is correct to state that despite the disordered character of the HuD structures, the introduction of hyperuniformity and the presence of a photonic band gap makes these photonic structures robust against unavoidable fabrication induced disorder or perturbations.
We conclude this part of the work by reporting, in the next two paragraphs, the results of an experimental work whose aim is validating our idea of HuD modes robustness to disorder.

6.3.3 Modes arising from disorder in nominally ordered photonic crystals

To better comprehend the nature of this behavior that HuD modes exhibit in presence of fabrication induced disorder, we show that not only they are different from resonances in random photonic structures (as seen before), but also modes arising from disorder in nominally ordered photonic crystals seem to display very different reproducibility features. In Fig.6.15 are reported some of the results obtained by the SNOM measurement of two nominally identical nominally ordered photonic crystals (SEM image in Fig.6.15a). These samples consist in GaAs single membranes that were patterned via EBL with an ordered triangular lattice with the aim of studying the generation of modes determined by unavoidable fabrication induced disorder. Within this framework, we performed a large (10 µm ×10 µm) near-field PL map collecting a PL spectrum for each point at 100 nm steps. The PL map acquired in the whole wavelength range (1195-1305) nm is shown in Fig.6.15b, in which we can observe fringes of modes arising from disorder, parallel to the axis of the lattice. This interesting feature is clearly shown in Fig.6.15c, in which a PL is overlapped to the SNOM topography, highlighting the lattice main directions. Fig.6.15e shows normalized PL spectra acquired in different points of map of Fig.6.15b. These sharp resonances, reported in the spectra of Fig.6.15e, are spectrally separated between each other by 1-2 nm; we can observe the spatial profiles of the first and last peak in the maps of Fig.6.15g and Fig.6.15h, that are PL maps filtered around the central wavelengths of the peaks (1248.0 nm and 1256.9 nm). The circles on the maps represent the point in which the spectra were acquired. We performed an analogue analysis on the nominally identical replica of the sample; the PL map of the entire spectral range is reported in Fig.6.15d and shows completely different spatial distributions of the signal. The modes here detected are shown in Fig.6.15f, and not only are all spectrally shifted by 5-10 nm with respect to their counterparts in the replica, but they are also localized in different areas of the map. The spatial distributions of the first and last mode detected in the replica are visible in the PL maps of Fig.6.15i and l (acquired at 1255.8 nm and 1263.6 nm). In conclusion, we experimentally showed that modes arising from fabrication induced disorder in nominally ordered photonic crystals display no robustness nor steadiness in presence of perturbation. However, a clarification should be made; perfect photonic crystals

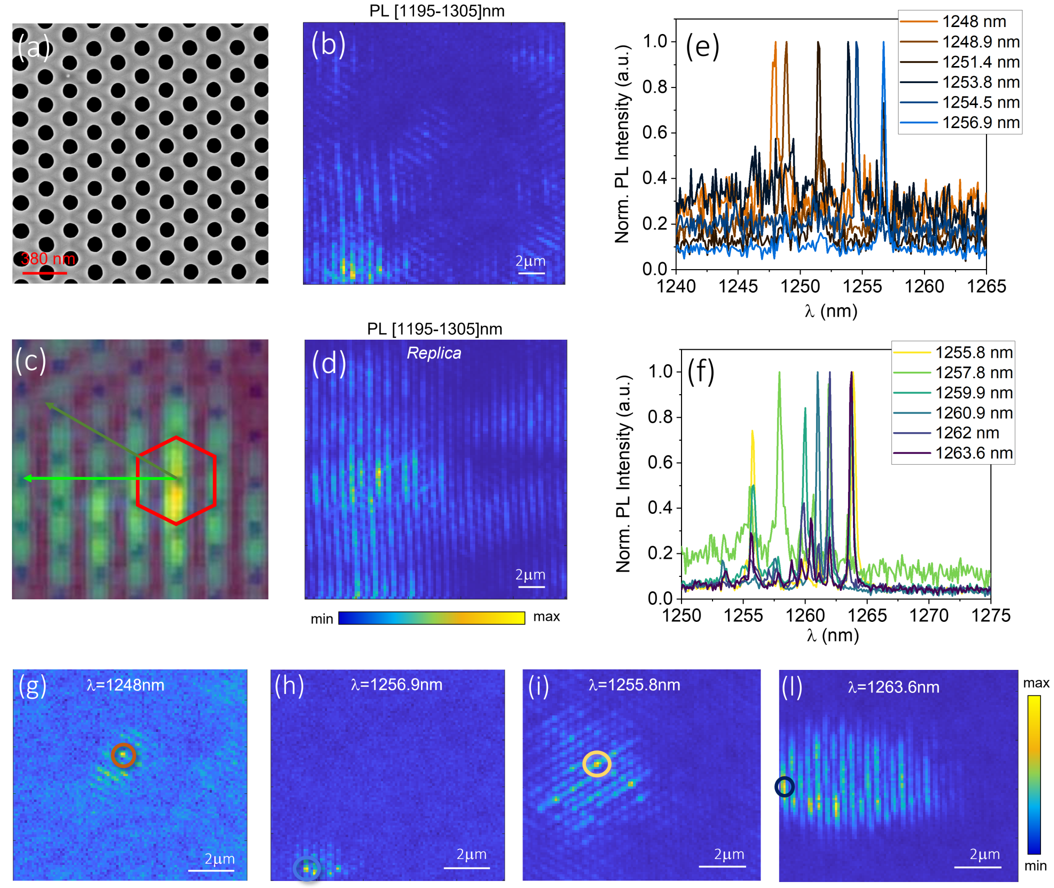

Figure 6.15. **(a)** SEM top view of the perfectly ordered photonic crystal. **(b)** PL map acquired in the wavelength range of (1195-1305 nm). **(c)** PL map overlapped to the topography of the sample. The sketch shows the elementary cell of the photonic crystal in $k-$space. **(d)** PL map acquired in the wavelength range of (1195-1305 nm) on the nominally identical replica of the sample measured in (b). **(e)** Normalized PL spectra acquired in different points of map (b), displaying all the modes arising from disorder in the original structure. **(f)** Normalized PL spectra acquired in different points of map, displaying all the modes arising from disorder in the replica. **(g)** and **(h)** are the PL maps at the central wavelengths of the first and last peak in (e), respectively $\lambda = 1248$ nm and $\lambda = 1256.9$ nm. **(i)** and **(l)** are the PL maps at the central wavelengths of the first and last peak in (f), respectively $\lambda = 1255.8$ nm and $\lambda = 1263.6$ nm. The circles on the maps represent the point in which the spectra were acquired.

display only extended and delocalized modes. Hence, it would be correct to state that they are strongly influenced by disorder since they probe a much larger area of the sample with respect to localized mode, and actually the disorder introduced during the fabrication is responsible of their origin. In the case of more localized modes, like the ones at the HuD PBG, the effect of disorder is slight, because it is on a scale smaller than the lattice parameters. For this reason, in the next Section we will show that HuD modes are more robust to fabrication induced disorder not only when they are localized, but also when they are extended.

6.3.4 SNOM measurements on nominally identical HuD replicas

We investigated two nominally identical samples and demonstrated that the same modes can be observed in the two samples, as a confirmation of our statement based on simulations regarding the modes robustness to fabrication induced disorder; some examples are given in Fig.6.16. In particular, we exploit the combination of HSI near-field mapping with topographic imaging of the sample for aligning different

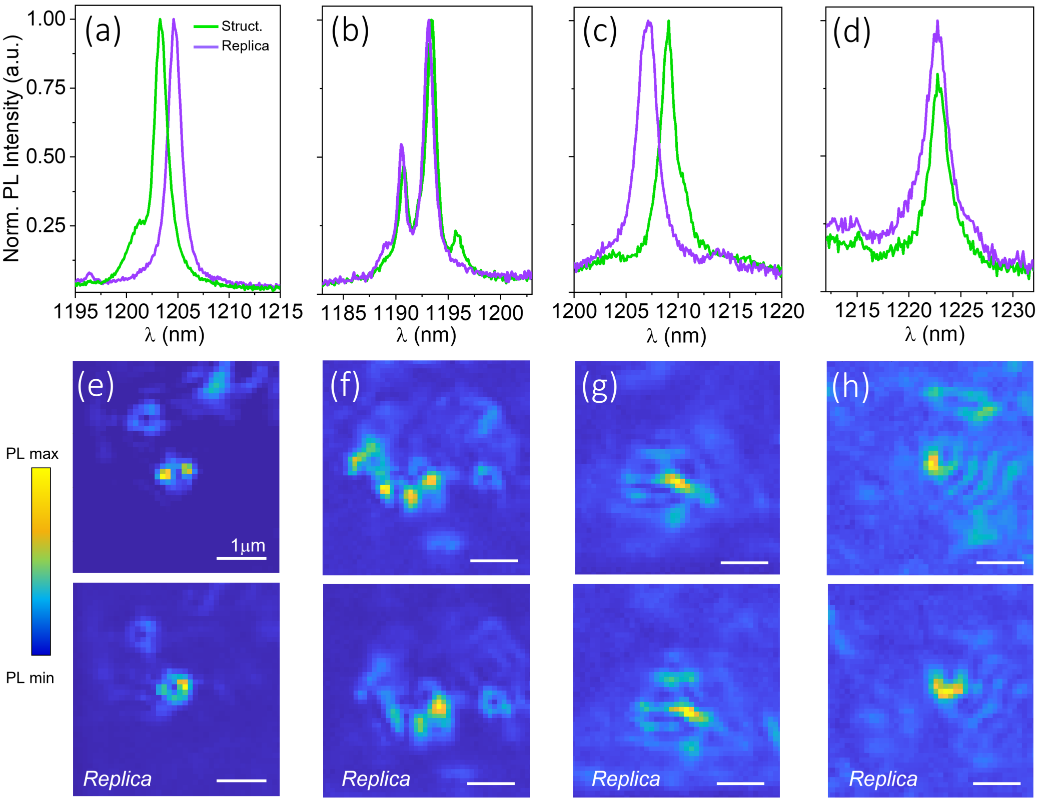

Figure 6.16. **(a)**, **(b)**, **(c)** and**(d)** are the PL spectra of four different modes acquired in the point of maximum intensity of each. In green are reported the spectra of the structure, in purple the ones of the replica. The top (bottom) panels of **(e)**, **(f)**, **(g)** and**(h)** are the SNOM PL maps filtered around the central wavelengths of the green (purple) peaks for the structure (replica), specifically $\lambda = 1203.3$ nm ($\lambda = 1204.6$ nm), $\lambda = 1194.0$ nm ($\lambda = 1193.0$ nm), $\lambda = 1209.0$ nm ($\lambda = 1207.0$ nm) and $\lambda = 1223.0$ nm ($\lambda = 1224.0$ nm).

maps at the nanoscale. In Fig.6.16a, b, c and d we present the spectra acquired at the position of maximum intensity of the PL signal of the selected mode in the replica (in purple), compared with the respect to its counterpart in the original structure (in green). Correspondingly, the upper panels of Figs.6.16e, f, g and h we show the SNOM PL maps acquired at the central wavelengths of the green peaks in the original structure, respectively $\lambda = 1203.3$ nm, $\lambda = 1194.0$ nm, $\lambda = 1209.0$ nm and $\lambda = 1223.0$ nm. In the bottom panels we show the SNOM PL maps acquired at the central wavelengths of the green peaks in the replica, respectively $\lambda = 1204.6$ nm, $\lambda = 1193.0$ nm, $\lambda = 1207.0$ nm and $\lambda = 1224.0$ nm. The similarity of the sub-micrometric details of the most variable shapes in the field distributions of the replicas is evident for all the four considered modes, not only in the brightest spots, but even throughout zones with a lower signal. As mentioned in the previous paragraph, also the localization scale of the modes is important when considering the effect of disorder. The modes of Fig.6.16 are the ones closest to the PBG edge, and are therefore localized. In order to make a fair comparison with the results obtained on the nominally ordered photonic crystals (Fig.6.15), we now focus on hyperuniform delocalized modes. In Fig.6.17 is reported an analysis analogue to the one performed for the localized modes; a and b show the PL spectra of two different

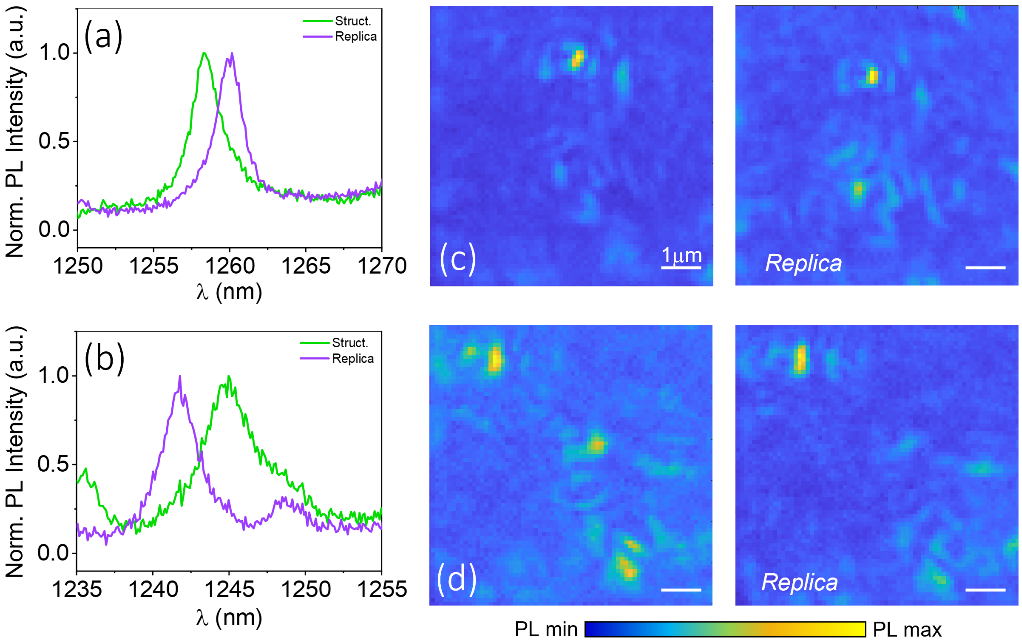

Figure 6.17. **(a)**, **(b)**: PL spectra of two delocalized modes acquired in the point of maximum intensity of each. In green are reported the spectra of the structure, in purple the ones of the replica. The left (right) panels of **(c)** and **(d)**, are the SNOM PL maps filtered around the central wavelengths of the green (purple) peaks for the structure (replica), specifically $\lambda = 1258$ nm ($\lambda = 1259$ nm) and $\lambda = 1244$ nm ($\lambda = 1242$ nm).

delocalized modes acquired in the point of maximum intensity of each. In green are reported the spectra of the structure, in purple the ones of the replica. The correspondent near-field maps are shown in Fig.6.17c and d, respectively filtered around 1258 nm and 1244 nm (1259 nm and 1242 nm for the replica). The spectral and spatial features are preserved; hence, not only HuD localized modes are slightly influenced by fabrication induced disorder. This provides a clear demonstration of the HuD modes robustness with respect to unavoidable fabrication induced disorder. In conclusion, we were able to demonstrate, both theoretically and experimentally, that photonic HuD structures combine the advantages of disordered and ordered systems for two reasons: first, they present a high density of modes that are more resilient to local perturbations with respect to typical random modes. Second, the localized modes arising at the PBG edges of a HuD structure exhibit a Q/V comparable to typical standard (not modified) photonic crystal cavities. Therefore, we conclude that it might be possible to exploit this peculiarity of HuD photonic modes, along with their high spatial density, to realize experiments in the field of QED and optoelectronics.

6.4 Optical photonic cavities in HuD materials

In Chapter 3 we have introduced the concept of hyperuniform "stealthy" disordered photonic solids with large isotropic band gaps comparable in width to the anisotropic band gaps found in photonic crystals; these solids challenge the conventional wisdom that band gaps require Bragg scattering and, hence, periodic or quasiperiodic order. The hyperuniform solids that we have described demonstrate that Mie scattering is sufficient to generate band gaps provided the disorder is constrained to be hyperuniform; in Section 3.3.1 we have explained how to design the dielectric materials [89], and in these last sections we explored their transport properties in the optical range, highlighting sparking features of their modes at the band-gap edges.

We now address the first near-field optical characterization of high-Q photonic cavities in slab architectures in hyperuniform disordered solids displaying isotropic band gaps. This kind of cavities, obtained by inserting intentional defects, were recently theoretically proposed in the work by Amoah and Florescu [100], and have never been experimentally realized so far. The architectures are based on carefully designed local modifications of otherwise unperturbed hyperuniform dielectric structures. Infact, in an HuD unperturbed structure, it is possible to create an intentional localized state of the electromagnetic field by reducing or enhancing the dielectric constant at a certain point in the structure, analogously to what is done to realize photonic crystal cavities. A wide range of confined cavity modes can be identified, that can be classified according to their approximate symmetry (monopole, dipole, quadrupole, etc) of the confined electromagnetic pattern. Here, we directly measure the resonant modes of a cavity in a HuD system by exploiting near-field mode imaging capable of subwavelength resolution in the near-IR range. To this end, similarly to the samples studied in the previous section, we are employing a special design of HuD in a single membrane with embedded quantum dots for feeding the HuD resonances via photoluminescence. By studying the same cavity modes for different nominal designs (i.e. different structural parameters) we are able to define the right combination of structural parameters to optimize the Q factors. We verify the cavity modes dependence with respect to the change in structural parameters, and therefore achieve an overall comprehension of the trends of the spectral positions and Q factors with respect to *air/dielectric* defects, finding a strong similarity with photonic crystals behaviours [66].

6.4.1 Cavity design and FEM simulations

The studied cavity design in HuD network enviroment is reported in Fig.6.18a. The HuD network, analogue to the one studied in the previous sections, has a length scale of $a = 380$ nm and comes from 500 points stealthy pattern.

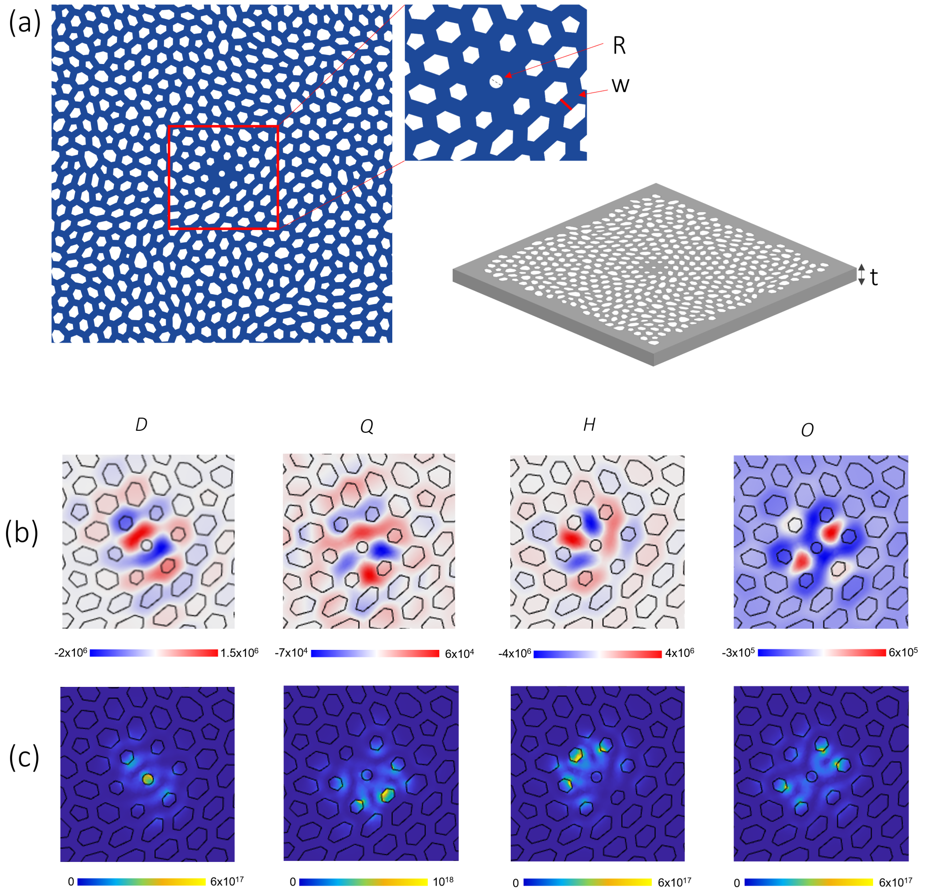

Figure 6.18. **(a)** Design of a modified cell cavity in a HuD network with length scale $a = 380$ nm and wall thickness $w = 0.36a$. On the top right of the figure are highlighted the wall thickness, the radius R of the central circular hole (in this case $R = 0.2a$), and the thickness $t = 180$ nm of the simulated GaAs membrane. **(b)** Magnetic field H_z simulated distribution for the four cavity mode. The modes are labelled, in order of increasing energy, D ($\lambda = 1345$ nm, dipole-like), Q ($\lambda = 1340$ nm, quadrupole like), H ($\lambda = 1321$ nm, hexapole-like) and O ($\lambda = 1283$ nm, octaple-like). The corresponding simulated electric field intensity distributions are reported in **(c)**, following the same order.

The most immediate way of realizing a cavity in this pattern would be to fill an air hole. Here, we concentrate on *modified* cavities [100].

A conventional method for achieving optimal designs is to reduce adjacent holes slightly in size and shift them outwards along the lattice directions. In the disordered case there are no lattice directions, and so the shrunken cells are shifted instead along the vector given by the center of mass of the cavity to the center of mass of the neighboring cell. The cavity is finally engineered by placing a circular hole (of radius R) at the center.
We performed FEM simulations on a GaAs single membrane of thickness t 180 nm and patterned with the described design with wall thickness $w = 0.36\ a$ and central hole radius $R = 0.2a$. We found four defects modes laying in the PBG, at $\lambda = 1345$ nm, $\lambda = 1340$ nm, $\lambda = 1321$ nm and $\lambda = 1283$ nm (in order of increasing energy). We label them after the convention introduced in [100], according to the spectral order and spatial distribution of the electromagnetic fields. In Fig.6.18b and c are reported respectively the magnetic field distribution H_z and electric field intensity distribution $|E|^2$ of the four modified cavity modes; the first one has a dipole-like profile (D), while the next higher frequency modes are a quadrupole-like mode (Q) and a hexapole-like mode (H). Comparing the H_z and $|E|^2$ patterns of the two modes (Q and H), we note that (due to disorder) the symmetry of the two modes is not entirely complete; for mode Q is more unbalanced in the bottom right direction, while for mode H the upper left part of the field is more intense. Lastly, there is the highest frequency mode which is rather difficult to define. We can identify 4 nodes lying within the cavity, so it can either be considered a second quadrupole mode or an octaple mode. Following the labelling of [100], we assert that since it is higher in frequency than the hexapole mode it can be named as an octapole-like mode (O).

6.4.2 Near-field imaging of HuD cavities

The analyzed samples consists in a single GaAs membrane patterned with the design reported in Fig.6.18a. The fabrication process, analogue to the one described in Section 6.1.2 is done through EBL and chemical etching. High-density InAs QDs, whose ground state emission is around 1300 nm, are embedded in the middle of the slab. In Fig.6.19a is shown the top view SEM image of one of the investigated samples, with nominal lattice constant $a = 380$ nm, wall thickness $w = 0.36a$ and radius of the central hole $R = 0.2a$. [100]. The experiment was realized by using the SNOM in *illumination/collection* configuration with a spectral resolution of 0.1 nm (see Section4.1.2). We performed a 3 µm × 3 µm scan with 50 nm/px spatial steps. In Fig.6.19b is shown a typical PL spectrum collected by the tip at a fixed position in the cavity region; four sharp resonances are detected, exhibiting a Q factor of 700, 1500, 2500 and 2150 (in order of increasing energy). By means of the morphological information given by the SNOM topography (Fig.6.19c), that can be compared with the optical maps filtered around each peak, we were able to establish that the four resonances correspond to the four cavity modes described in the previous paragraph (Fig.6.18b and c): the dipole-like mode D ($\lambda = 1307.4$ nm), the quadrupole-like mode Q ($\lambda = 1304.5$ nm), the hexapole-like mode H ($\lambda = 1291.7$ nm) and the octaple-like mode O ($\lambda = 1258.2$ nm). The $\approx$ 30-40 nm shift between theory and experiment can be attributed to several uncertainties regarding the difference between nominal and fabricated structural parameters (slab thickness, wall thickness, central hole radius etc). For each peak, we performed a single lorentzian fit, and obtained the four fitted amplitude maps reported in Fig.6.19d.

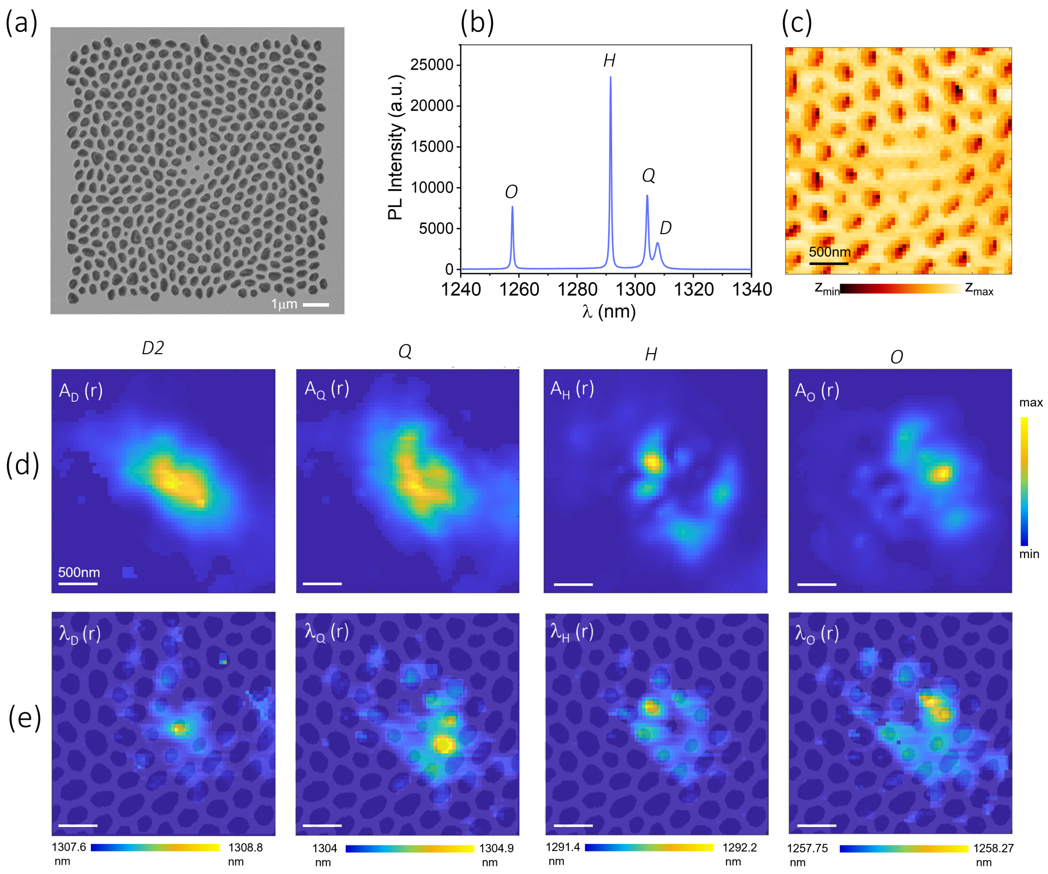

Figure 6.19. This Figure resumes the results of a 3 µm × 3 µm SNOM scan with 50 nm/px spatial steps, on the sample whose SEM image is shown in **(a)**, with $a = 380$ nm, $w = 0.36a$ thickness, and $R = 0.2a$. **(b)** Typical PL spectrum acquired in a tip position during the scan. The four peaks, D, Q, H and O are identified thanks to the combination of the optical and morphological information. **(c)** Topography acquired during the scan. **(d)** Fitted amplitude maps of the four peaks: $\lambda = 1307.4$ nm, $\lambda = 1304.5$ nm, $\lambda = 1291.7$ nm and $\lambda = 1258.2$ nm. **(e)** Spectral shifts map of the four peaks.

It was experimentally demonstrated, in the work by Intonti *et al* [160], that the local introduction of a subwavelength dielectric SiO_2 tip can be used for accurate tuning of the resonance frequency of a photonic crystal microcavity without necessarily introducing significant losses, and that this same principle can indeed be used as a powerful method for mapping the electromagnetic LDOS with high fidelity, which is essential for the proper characterization of photonic structure in general. Even if SNOM experiments have proven to have enough sensitivity and spatial resolution for this purpose, an unambiguous and artifact free determination of the LDOS is often difficult to achieve, partly due to the complex interaction between SNOM tip and sample. Infact, even if in conventional SNOM experiments the PL intensity is assumed to directly correspond to the spatial distribution of the electric field intensity [168, 169], the maps shown in Fig.6.19d, which report the fitted amplitude of the PL signal, demonstrate that this conventional method leads to a spatial resolution of ≈ 250 nm. This might be related to the fact that the PL intensity collected through the tip can be affected by different parameters, as the not perfect coincidence of the physical shape of the tip and its optically active region, the eventuality that the tip collects a mixture of evanescent and propagating waves, and the possible inhomogeneity of the quantum dots. We confirm here, regarding a HuD modified cavity, what has been demonstrated in [160]: a very good measure for the local electric field intensity is the tip-induced spectral shift. Since the strength of the tip induced spectral shift is proportional to the electric field intensity of the eigenmode [170], this improved imaging method can be applied also to the HuD cavity design. By constructing maps of this shift one obtains an imaging method which reproduces the LDOS with much higher fidelity than conventional SNOM methods. In addition, maps of the broadening of the resonance peaks can be used to determine the tip-induced losses and obtain important insights on the SNOM detection mechanisms. In Fig.6.19e we report the spectral shift maps of the four modes overlapped to the SEM image; by comparing them to the simulated map of Fig.6.18c, we can confirm that the map of the spectral shift represents a cleaner measurement of the LDOS with respect to the map of the fitted PL amplitude. This observation is particulary suited to the experimental maps of modes D and Q, where the hotspot location (in the central hole for D and in the bottom right part of the cavity for H), completely hidden by the amplitude maps, is revealed by the spectral shift.

We conclude the study on HuD modified cavities by studying how the resonances are dependent from the variation of two structural parameters: the wall thickness w and the central hole radius R. We performed SNOM measurements on cavities with three different values of w and three different values of R, specifically: $w = 0.36a$, $0.40a$ and $0.44a$, and $R = 0.2a$, $R = 0.3a$ and $R = 0.4a$. Three different topographies for the samples with $R = 0.2a$, $R = 0.3a$ and $R = 0.4a$ ($w = 0.36a$) are shown in Fig.6.20a, where we can observe the increasing of the air hole at the center of the cavity. We performed a statistical analysis (by means of the lorentzian fits) of the spectral position and Q factor changes with respect to w and R for the three higher order modes, O, H and Q, and the results are shown in Fig.6.20b and c. The modes are labelled with a full (empty) dot (O), an hexagon (H) and a square (Q) in the trend of the spectral positions (Q factors). In Fig.6.20b we display the spectral positions extracted by the fits for the three modes O, H and Q (from top graph to bottom graph); on the horizontal axis are reported the three values of R, while different values of w are highlighted in different colors (green for $w = 0.36a$, blue for $w = 0.40a$ and magenta for $w = 0.44a$). It is worth noticing an overall trend in two directions, depending respectively on the increasing of R and on the increasing of w: as the central hole radius increases, and this can be considered as an *air defect* following a photonic formalism [66], the central wavelength of all modes decreases. Differently, as the wall thickness is increased (*dielectric defect*), the spectral positions are redshifted. While mode O and H exhibit shifts that are comparable and approximately constant, mode Q results more affected by the structural changes and displays irregular shifts. In Fig.6.20c we report the trend of the Q factors extracted by the fits for the three modes O, H and Q (from top graph to

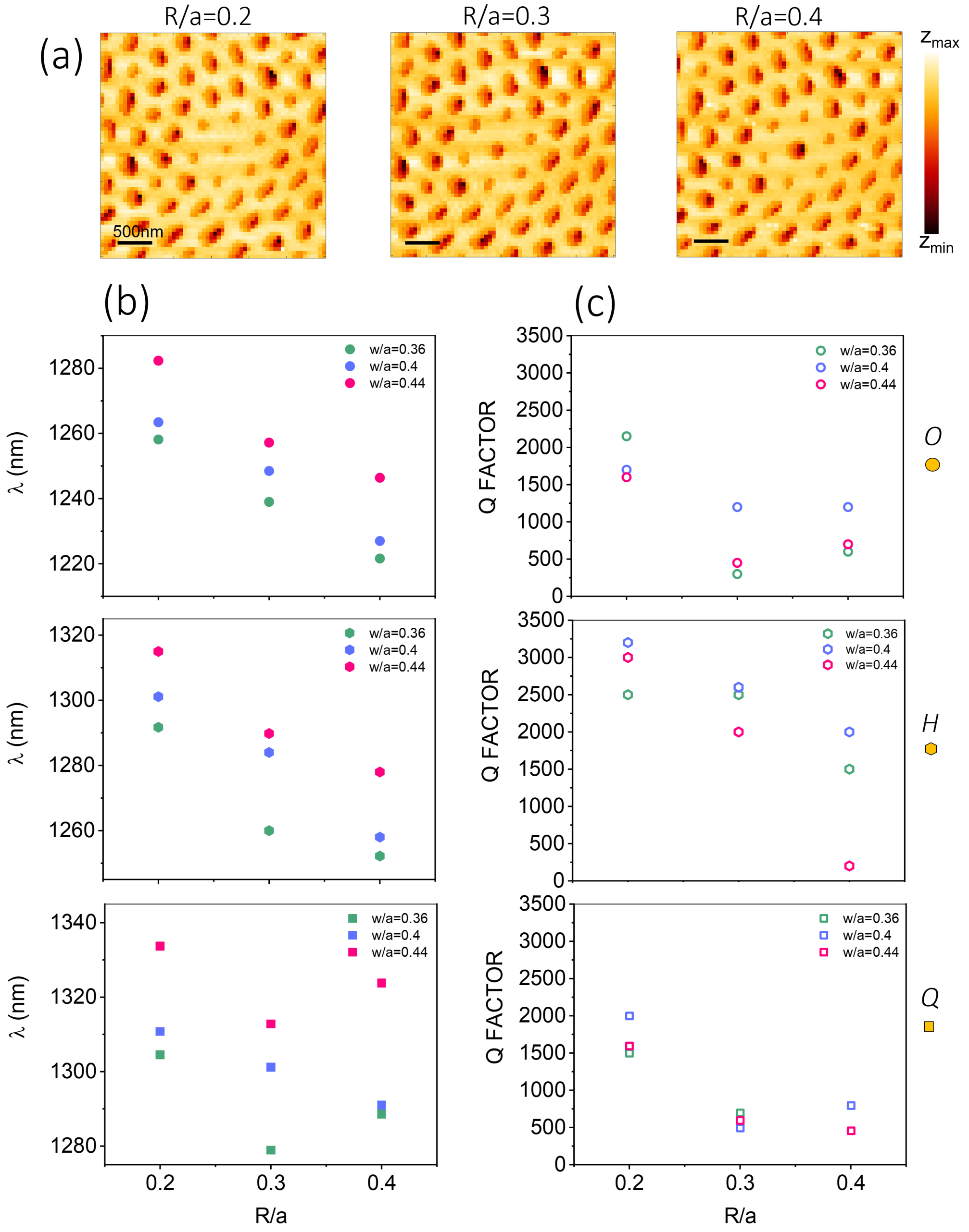

Figure 6.20. **(a)** SNOM topographies acquired during a 3 µm × 3 µm SNOM scan with 50 nm/px spatial steps, performed on three modified cavities with $R = 0.2a$, $R = 0.3a$ and $R = 0.4a$ ($w = 0.36a$). **(b)** Spectral positions extracted by the fits for the three modes O (full dots), H (full hexagons) and Q (full squares), from top graph to bottom graph; on the horizontal axis are reported the three values of R, while different values of w are highlighted in different colors (green for $w = 0.36a$, blue for $w = 0.4a$ and magenta for $w = 0.44a$). **(c)** Trend of the Q factors extracted by the fits for the three modes O (empty dots), H (empty hexagons) and Q (empty squares) (from top graph to bottom graph).

bottom graph); in this case the trend with respect to different nominal parameters is less intuitive than the spectral shift. For this reason it is interesting to search for the better configuration that maximize the Q factor. The overall highest Q value (3200) is obtained in mode H in the configuration of $R = 0.2a$ and $w = 0.40a$. Mode O achieves the maximum detected Q factor in the configuration of minimum R and minimum w, while the other two modes exhibit the highest Q value for the minimum R but intermediate w ($0.44a$). Analogously, the two modes H and Q have the smaller Q factor in the configuration $R = 0.4a$ and $w = 0.44a$; this similarity is probably due to the very similar broken symmetry that their spatial distribution exhibits.

In conclusion, we performed a near-field hyperspectral imaging experiment on the first high-Q photonic cavities in slab architectures in hyperuniform disordered systems. The ability of optically characterizing localized modes of different symmetry and frequency in the same physical cavity and to guide light through modes with different localization properties can have a great impact on all-optical switching, implementations of linear-optical quantum information processors and single photon sources. The results here presented might open novel approaches of finely tuning the resonant modes in HuD cavities, and also to deepen the study of the near-field probe interaction with a correlated disorder photonic enviroment.

With the investigations presented in this Chapter, we were able to present how hyperuniform disordered photonics can provide fascinating and versatile tools in the field of optoelectronics and QED applications.

Chapter 7

Conclusions and future perspectives

In this last Chapter we aim at giving the conclusions of this work and resume the main achievements that were presented. We then grab the opportunity to draw some lines towards what might come next, by presenting a general and qualitative idea of what are some of the possible future developments within the framework of the topics covered so far, based on the results obtained in this thesis.

7.1 Conclusions

The whole point of this thesis work is located within the framework of light localization in all-dielectric nanostructures, from single Mie resonators to correlated disordered media. Light propagation through a dielectric medium is determined by the spatial distribution of the material, as photons scatter at local variations of the refractive index. Just think of how the formation of photonic band gaps in random, quasicrystals or hyperuniform materials is strictly associated with the Mie resonances of the single scattering centers.

The application of groundbreaking imaging techniques like near-field and dark-field hyperspectral imaging on such complex architectures, is here proven to be a fascinating tool not only for the optical characterization, extremely important to understand their fundamental physical properties (like magnetic light eigenstates or light transport regimes in hyperuniform disordered systems) but also an efficient vehicle for probing their practical potentialities. The presented experimental results are carefully supported by theory and numerical calculations. We resume in the following the main achieved tasks.

Sub-wavelength Hyperspectral Imaging of dielectric Mie resonators

We provided a complete optical characterization on the higher order multipolar Mie resonances in a single all dielectric island obtained by solid state dewetting.

- Through the Near-field hyperspectral imaging technique, we were able to study the modes arising from the combination of the Mie resonances of the scatterer with the etalon effect due to a thick SiO_2 layer below the scatterer. By means of FDTD simulations we achieved a full comprehension of the sensitivity of *magnetic light* with respect to the thickness of the substrate and the angle of illumination. The combination of numerical and experimental results offers a detailed analysis of how such sensitivity affects the near-field scattering pattern of the antenna, suggesting a novel approach to engineer the coupling of a single emitter with localized electric field maxima: infact, if external illumination can have an impact on the emission, in particular, it could offer certain control on the absorption of the emitter in this kind of photonic applications.

- In order to characterize the beam-steering properties of such nanoparticles, we implemented Dark-field spectroscopy on the SNOM setup. By means of FDTD simulations we were able to interpret the information provided by the new developed technique. We found that the hyperspectral maps obtained in these measurements are a faithful reproduction of the real spatial distribution electric field intensity scattered by the nanoantenna under tilted illumination. The imaging of the single distributions resulted intrinsically related to the (simulated) scattering directionality. We also were able to demonstrate how in this configuration, the dark-field spectra display nice modulations within 200 nm displacements of the collection spot, demonstrating the incompleteness of standard dark-field spectra. The complementarity of near-field and dark-field hyperspectral imaging, together with the fundamental role played by the tilted illumination on a dielectric nanoantenna, contributed to fill a hole in this research field where only limited information on the higher order multipolar Mie terms is provided.

Deep subwavelength imaging of hyperuniform disordered systems

We exploited a novel idea of Hyperuniform Disordered (HuD) systems for a detailed experimental benchmark of several theoretical predictions, by designing and nanofabricating the first ever optically active hyperuniform structures with embedded quantum dots emitting at telecom wavelengths. This breakthrough in the field, which we linked with the very first optical near-field hyperspectral imaging of HuD systems, led to several innovative and unexpected results on the peculiarities of band edge HuD modes, in a novel class of materials that combines the advantages of both ordered and disordered structures.

- By taking the advantage of the combination of the HuD special design in slab photonics and the use of embedded quantum dots for feeding the HuD resonances, we were able to map the fluctuations, both spectrally and spatially, of photonic local density of states emerging from the correlated disorder. Thanks to the slab photonics aspect, we performed a deep subwavelength imaging of all HuD mode in a large optical frequency range so to detect the properties on each individual modes as well as to probe a large number of them in order to perform a statistical analysis.

- We experimentally benchmarked the transition from localized to delocalized light modes in correlated disorder photonic structure, monitoring relevant features for application such as quality factor, modal volume and inverse participation ratio.

- In contrast to previous studies of hyperuniform disordered structures, which show band edge states extended over a number of cells in the disordered network, we identify a novel band edge state tightly localized over a topological defect (a four-sided cell in the hyperuniform network). Our results show that whenever these extreme topological defects are presented in the structure, they are associated with states located at the lower band edge frequency.

- We were able to demonstrate, both theoretically and experimentally, that the localized modes arising at the PBG edges of a HuD structure are more resilient to local perturbations with respect to typical random modes, and exhibit a Q/V comparable to typical photonic crystal cavities. Therefore, it might be possible to exploit this peculiarity of HuD photonic modes, along with their high spatial density, to realize experiments in the field of QED and optoelectronics without any need of intentional defects.

- We performed a near-field hyperspectral imaging experiment on the first high-Q photonic cavities in slab architectures in hyperuniform disordered systems, showing how the ability of optically characterizing localized modes of different symmetry and frequency in the same optical cavity might bring HuD systems to be the next main player in the field of optoelectronic applications.

7.2 Future perspectives

Study of the topological defect in HuD systems

In Chapter 3 and 6 we have explained how in HuD systems, two types of localized modes are present: the first kind can be considered as Anderson-like modes, occur naturally at the PBG edge and have been widely characterized in this thesis. The other category is represented by the accidental modes that arise due to local peculiar topology [153]; an example of four-sided cell topological defect has been described in Section 6.1.1. This mode is particularly special for two main reasons: it displays a relatively low Q factor (750) despite the tighter in-plane spatial confinement, due to losses in the vertical direction associated with the $k-$space components inside the light cone and directly related to the symmetry and the spatial extent of the intensity profile. From a theoretical point of view, it is a fascinating defect, because it occurs exactly in the PBG, and disappears as disorder is increased.
By designing larger samples, like the one reported in Fig.7.1, in which several topological defects are visible, it has been clear that the only type of band edge topological defects are the four-folded ones. The next step is to investigate optically active samples of this kind with the SNOM, in order to study how the topological defects interact with each other and how they are conditioned by structural parameters if compared with modified optical cavities (like the one studied in Section 6.4).

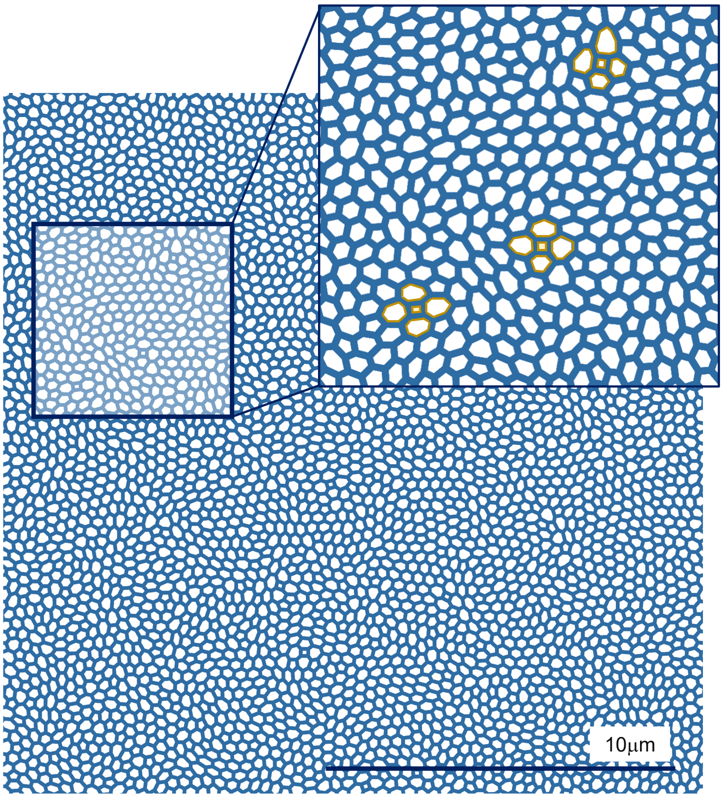

Figure 7.1. Topological defects in HuD - HuD large design where several topological defects can be seen.

Optically active Mie resonators

Highly confined electric field intensity and directional scattering of light are Mie resonators properties of a certain interest for the integration of such systems with light emitter. The integration of perovskites with Mie antennas is an emerging field in the optoelectronics community. Recent results demonstrated that the perovskite emission in polycrystalline thin films can be signifcantly enhanced by silicon submicrometric particles [171] or by nanoimprinting a metasurface directly into the perovskite thin film [172]. In addition, Mie resonances present in relatively large perovskite quasi-spheres were exploited to tune the emission wavelength [173] or generate Fano resonances [174]. Indeed, the use of perovskite materials has been recently reviewed as potential candidates to develop a new generation of "active metadevices." Recently, enhanced nanoscopy in individual green emitting perovskite ($CsPbBr_3$) nanocrystals via TiO_2 dielectric nanoantenna was realized in the work by Suarez et al [34]. On the other hand, the investigation of the spectral and spatial properties of resonant optical modes is much more clear and more reliable when the resonators are coupled with emitters and is then possible to study the spatial distribution of the photoluminescence signal of the emitters coupled with the optical modes of the resonators. Therefore, one of the most promising way of exploiting the Near-field and Far-field optical characterization performed on Mie resonators is to place a light emitter on the dewetted samples. One versatile approach is the use of inorganic perovskite that show a brilliant PL signal in the visible range, that can be tuned in a controlled way by varying their composition. To study the feasibility of this approach we grew a thin layer of $CsPbCl_xBr_{3-x}$ perovskite, that are expected to show resonances in the blue/green, on samples with dewetted structures (Germanium islands). A sketch of the idea, next to the preliminary results on the perovskite deposition and SNOM optical characterization of the sample are shown in Fig.7.2a. This preliminary test showed the feasibility of the deposition of perovskites on dielectric islands, and revealed that the perovskites settled spontaneously in the interstitial regions between the islands; moreover, the SNOM PL, obtained by scanning the sample with the tip in *illumination/collection* geometry, showed a crown-like distribution that well reproduces the perovskites collocation around the dewetted islands. With this result in mind, we are going to optically characterize the Mie resonances of single dewetted nanoparticles (possibly arranged in ordered arrays) before the perovskite deposition. Then, after the deposition, we will verify the emission enhancement to be attributed to near-field effects and emission steering promoted by the coupling between the perovskite nanocrystals and the dielectric sub-micrometric antennas Mie modes.

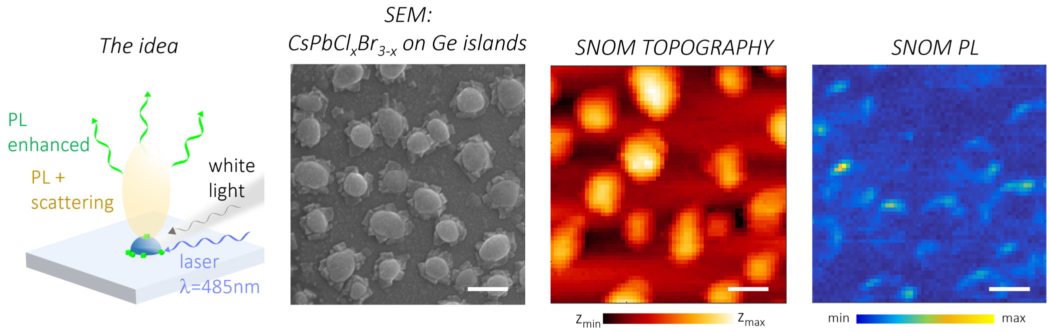
The idea
SEM: $CsPbCl_xBr_{3-x}$ on Ge islands
SNOM TOPOGRAPHY
SNOM PL

Figure 7.2. Enhanced nanoscopy idea on dewetted Mie resonators - *from left to right*, sketch of the future experiment to be performed on perovskites $CsPbCl_xBr_{3-x}$ coupled to dewetted dielectric islands; SEM image of the sample where the nanocrystals were deposited, SNOM topography on the sample; SNOM PL map of the signal emitted by the deposited perovskites around the Ge islands (λ=486 nm). All white scalebars correspond to 500 nm.

Electromagnetic fields in spinodal hyperuniform solids

The third perspective that we present contributes to further link the study of dewetted dielectric resonators and Hyperuniformity. In Chapter 6 we achieved a reliable comprehension of the near-field features of light-emitting disordered hyperuniform structures obtained via top-down approaches; a possible route of developement is to address bottom-up disordered hyperuniform nano-architectures obtained via spinodal dewetting. Infact, theoretically it is known that spinodal decomposition can lead to disordered hyperuniform architectures [78]; recently, as mentioned in Section 2.3, it has been shown that monocrystalline semiconductor-based structures, in particular $Si_{1-x}Ge_x$ layers deposited on silicon-on-insulator substrates, can undergo spinodal solid-state dewetting featuring correlated disorder with an effective

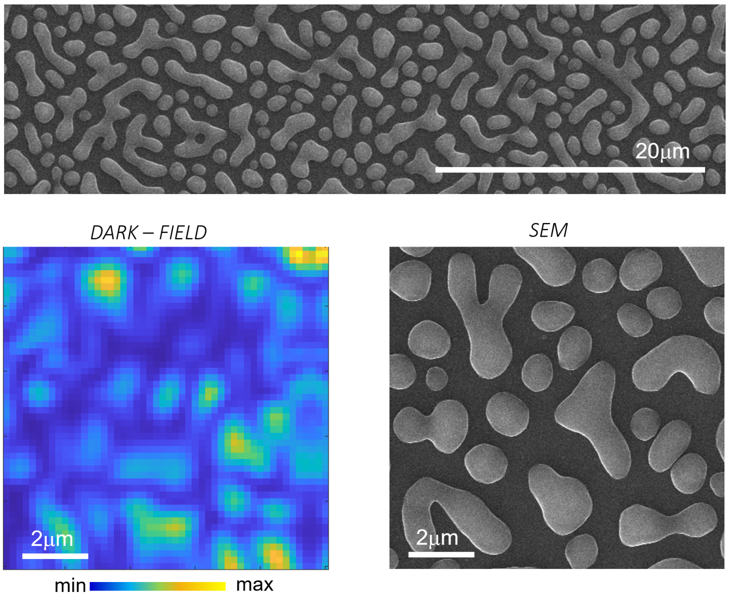

Figure 7.3. Spinodal dewetted dielectrics with hyperuniform character - SEM image of a spinodal dewetted sample that has been proven to exhibit hyperuniform character [41]. The bottom left image is a preliminary dark-field map at λ=685 nm of one part of the sample, showing the real distribution of the electric field scattered by the structure.

hyperuniform character [41]. This allows to fabricate on large scales nano- to micrometric sized structures targeting specific morphologies and hyperuniform character Fig.7.3, proving the generality of the approach and paving the way for technological applications of disordered hyperuniform metamaterials. The optical properties of such structures, and the comprehension of the electromagnetic fields localized inside them however, have never been attempted so far. We will take advantage of a special combination of numerical simulations and the dark-field scanning microscopy setup developed in this thesis in order to achieve this task. A preliminary dark-field measurement on this kind of samples can be observed in Fig.7.3. We believe that this investigation might pave the way for a total new way of integrating spinodal dewetted structures in the field of photonic and optoelectronics applications.

Papers produced during the PhD

(*i*) *"Multimode photonic molecules for advanced force sensing"*, **N. Granchi**, M. Petruzzella, D. Balestri, A. Fiore, M. Gurioli, and F. Intonti, *Optics Express* **27**, 37579-37589 (2019).

(*ii*) *"Fabrication of Si-based dielectric resonators: Combining etaloning with Mie resonances"*, D. Toliopoulos, M. Khoury, M. Bouabdellaoui, **N. Granchi**, J.-B. Claude, A. Benali, I. Berbezier, D. Hannani, A. Ronda, J. Wenger, M. Bollani, M. Gurioli, S. Sanguinetti, F. Intonti, and M. Abbarchi, *Optics Express* **28**, 37734-3774, (2020).

(*iii*) *"Flexible photonic devices based on dielectric antennas"*, A. Benali, J. Claude, **N. Granchi**, S. Checcucci, M. Bouabdellaoui, M. Zazoui , M. Bollani , M. Salvalaglio, J. Wenger, L. Favre, D. Grosso, A. Ronda, I. Berbezier, M. Gurioli and M. Abbarchi, *JPhys. Photonics*, **2**, 1, (2020).

(*iv*) *"Non-Lorentzian Local Density of States in Coupled Photonic Crystal Cavities Probed by Near- and Far-Field Emission"*, D. Pellegrino, D. Balestri, **N. Granchi**, M. Ciardi, F. Intonti, F. Pagliano, A. Y. Silov, F. W. Otten, T. Wu, K. Vynck, P. Lalanne, A. Fiore, and M. Gurioli, *Physical Review Letters*, **124**, 123902 (2020).

(*v*) *"Near field imaging of the Magnetic Complex Mode Volumes"*, N. Caselli, T. Wu, G. Arregui, **N. Granchi**, F. Intonti, P. Lalanne, and M. Gurioli, *ACS Photonics*, **8** (5), 1258-1263, (2021).

(*vi*) *"Near-field Hyperspectral Imaging of Resonant Mie Modes in a Dielectric Island"*, **N. Granchi**, M. Montanari, A. Ristori, M. Khoury, M. Bouabdellaoui, C. Barri, L. Fagiani, M. Gurioli, M. Bollani, M. Abbarchi, and F. Intonti, *APL Photonics*, **6**, 126102 (2021).

(*vii*) *"Deep subwavelength imaging of Hyperuniform Disordered Systems: from light transport regimes to quantum electrodynamics"*, **N. Granchi**, R. Spalding, M. Lodde, M. Petruzzella, F. W. Otten, A. Fiore, F. Intonti, R. Sapienza, M. Florescu and M. Gurioli, *submitted.*

(*viii*) *"Linear and non linear optical properties of dewetted SiGe islands"*, L. Fagiani, **N. Granchi**, A. Zilli, C. Barri, F. Rusconi, M. Montanari, E. Mafakheri, M. Celebrano, M. Bouabdellaoui, M. Abbarchi, F. Intonti, P.o Biagioni, M. Finazzi, M. A. Vincenti, and M. Bollani, *Optical Materials: X*, **13**, 100116, (2022).

(*ix*) *"Mie resonators beam steering properties detection through Dark-field Scanning Microscopy"*, **N. Granchi**, L. Fagiani, M. Montanari, A. Ristori, M. Khoury, M. Bouabdellaoui, C. Barri, M. Gurioli, M. Bollani, M. Abbarchi, and F. Intonti, *in preparation.*

(*x*) *"Near-field imaging of high Q cavities in hyperuniform architectures"*, **N. Granchi**, M. Lodde, R. Spalding, F.W. Otten, A. Fiore, R.Sapienza, F. Intonti, M. Florescu and M. Gurioli, *in preparation.*

Bibliography

[1] M. Born and E. Wolf, "Principles of optics," Dec. 2019.

[2] E. Abbe, "Beiträge zur theorie des mikroskops und der mikroskopischen wahrnehmung," *Archiv für Mikroskopische Anatomie*, vol. 9, pp. 413–468, Dec. 1873.

[3] Rayleigh, "XXXI. investigations in optics, with special reference to the spectroscope," *The London, Edinburgh, and Dublin Philosophical Magazine and Journal of Science*, vol. 8, pp. 261–274, Oct. 1879.

[4] Rayleigh, "XV.on the theory of optical images, with special reference to the microscope," *The London, Edinburgh, and Dublin Philosophical Magazine and Journal of Science*, vol. 42, pp. 167–195, Aug. 1896.

[5] E. Hecht, *Optics, Global Edition.* Pearson Education Limited, Dec. 2016.

[6] Q. Wu, G. D. Feke, R. D. Grober, and L. P. Ghislain, "Realization of numerical aperture 2.0 using a gallium phosphide solid immersion lens," *Applied Physics Letters*, vol. 75, pp. 4064–4066, Dec. 1999.

[7] J. D. Jackson and L. C. Levitt, "Classical electrodynamics," *Physics Today*, vol. 15, pp. 62–62, Nov. 1962.

[8] L. Novotny and B. Hecht, "Principles of nano-optics," 2006.

[9] Y. Akahane, T. Asano, B.-S. Song, and S. Noda, "High-q photonic nanocavity in a two-dimensional photonic crystal," *Nature*, vol. 425, pp. 944–947, Oct. 2003.

[10] F. Riboli, N. Caselli, S. Vignolini, F. Intonti, K. Vynck, P. Barthelemy, A. Gerardino, L. Balet, L. H. Li, A. Fiore, M. Gurioli, and D. S. Wiersma, "Engineering of light confinement in strongly scattering disordered media," *Nature Materials*, vol. 13, pp. 720–725, May 2014.

[11] G. Mie, "Beiträge zur optik trüber medien, speziell kolloidaler metallösungen," *Annalen der Physik*, vol. 330, no. 3, pp. 377–445, 1908.

[12] S. Jahani and Z. Jacob, "All-dielectric metamaterials," *Nature Nanotechnology*, vol. 11, pp. 23–36, Jan. 2016.

[13] M. Kerker, D.-S. Wang, and C. L. Giles, “Electromagnetic scattering by magnetic spheres,” *Journal of the Optical Society of America*, vol. 73, p. 765, June 1983.

[14] D. G. Baranov, D. A. Zuev, S. I. Lepeshov, O. V. Kotov, A. E. Krasnok, A. B. Evlyukhin, and B. N. Chichkov, “All-dielectric nanophotonics: the quest for better materials and fabrication techniques,” *Optica*, vol. 4, p. 814, July 2017.

[15] K. J. Vahala, “Optical microcavities,” *Nature*, vol. 424, pp. 839–846, Aug. 2003.

[16] J. A. Fan, C. Wu, K. Bao, J. Bao, R. Bardhan, N. J. Halas, V. N. Manoharan, P. Nordlander, G. Shvets, and F. Capasso, “Self-assembled plasmonic nanoparticle clusters,” *Science*, vol. 328, pp. 1135–1138, May 2010.

[17] J. B. Khurgin, “How to deal with the loss in plasmonics and metamaterials,” *Nature Nanotechnology*, vol. 10, pp. 2–6, Jan. 2015.

[18] M. Abbarchi, M. Naffouti, B. Vial, A. Benkouider, L. Lermusiaux, L. Favre, A. Ronda, S. Bidault, I. Berbezier, and N. Bonod, “Wafer scale formation of monocrystalline silicon-based mie resonators via silicon-on-insulator dewetting,” *ACS Nano*, vol. 8, pp. 11181–11190, Nov. 2014.

[19] L. Rayleigh, “X. on the electromagnetic theory of light,” *The London, Edinburgh, and Dublin Philosophical Magazine and Journal of Science*, vol. 12, pp. 81–101, Aug. 1881.

[20] Q. Zhao, J. Zhou, F. Zhang, and D. Lippens, “Mie resonance-based dielectric metamaterials,” *Materials Today*, vol. 12, pp. 60–69, Dec. 2009.

[21] C. F. Bohren and D. R. Huffman, *Absorption and Scattering of Light by Small Particles*. Wiley, Apr. 1998.

[22] H. C. V. de Hulst and V. Twersky, “Light scattering by small particles,” *Physics Today*, vol. 10, pp. 28–30, Dec. 1957.

[23] A. I. Kuznetsov, A. E. Miroshnichenko, M. L. Brongersma, Y. S. Kivshar, and B. Luk’yanchuk, “Optically resonant dielectric nanostructures,” *Science*, vol. 354, p. aag2472, Nov. 2016.

[24] J. van de Groep and A. Polman, “Designing dielectric resonators on substrates: Combining magnetic and electric resonances,” *Optics Express*, vol. 21, p. 26285, Oct. 2013.

[25] A. García-Etxarri, R. Gómez-Medina, L. S. Froufe-Pérez, C. López, L. Chantada, F. Scheffold, J. Aizpurua, M. Nieto-Vesperinas, and J. J. Sáenz, “Strong magnetic response of submicron silicon particles in the infrared,” *Optics Express*, vol. 19, p. 4815, Feb. 2011.

[26] P. Jin and R. W. Ziolkowski, “Metamaterial-inspired, electrically small huygens sources,” *IEEE Antennas and Wireless Propagation Letters*, vol. 9, pp. 501–505, 2010.

[27] A. I. Kuznetsov, A. E. Miroshnichenko, Y. H. Fu, J. Zhang, and B. Luk'yanchuk, "Magnetic light," *Scientific Reports*, vol. 2, July 2012.

[28] Y. H. Fu, A. I. Kuznetsov, A. E. Miroshnichenko, Y. F. Yu, and B. Luk'yanchuk, "Directional visible light scattering by silicon nanoparticles," *Nature Communications*, vol. 4, Feb. 2013.

[29] S. Person, M. Jain, Z. Lapin, J. J. Sáenz, G. Wicks, and L. Novotny, "Demonstration of zero optical backscattering from single nanoparticles," *Nano Letters*, vol. 13, pp. 1806–1809, Mar. 2013.

[30] N. Meinzer, W. L. Barnes, and I. R. Hooper, "Plasmonic meta-atoms and metasurfaces," *Nature Photonics*, vol. 8, pp. 889–898, Nov. 2014.

[31] H. Yonezawa, S. L. Braunstein, and A. Furusawa, "Experimental demonstration of quantum teleportation of broadband squeezing," *Physical Review Letters*, vol. 99, p. 110503, Sept. 2007.

[32] J. Proust, F. Bedu, B. Gallas, I. Ozerov, and N. Bonod, "All-dielectric colored metasurfaces with silicon mie resonators," *ACS Nano*, vol. 10, pp. 7761–7767, Aug. 2016.

[33] W. Liu and Y. S. Kivshar, "Generalized kerker effects in nanophotonics and meta-optics [invited]," *Optics Express*, vol. 26, p. 13085, May 2018.

[34] I. Suárez, T. Wood, J. P. M. Pastor, D. Balestri, S. Checcucci, T. David, L. Favre, J.-B. Claude, D. Grosso, A. F. Gualdrón-Reyes, I. Mora-Seró, M. Abbarchi, and M. Gurioli, "Enhanced nanoscopy of individual CsPbBr3 perovskite nanocrystals using dielectric sub-micrometric antennas," *APL Materials*, vol. 8, p. 021109, Feb. 2020.

[35] P. Fan, K. C. Y. Huang, L. Cao, and M. L. Brongersma, "Redesigning photodetector electrodes as an optical antenna," *Nano Letters*, vol. 13, pp. 392–396, Jan. 2013.

[36] P. Spinelli, M. A. Verschuuren, and A. Polman, "Broadband omnidirectional antireflection coating based on subwavelength surface mie resonators," *Nature Communications*, vol. 3, Jan. 2012.

[37] P. Spinelli, B. Macco, M. A. Verschuuren, W. M. M. Kessels, and A. Polman, "Al2o3/TiO2 nano-pattern antireflection coating with ultralow surface recombination," *Applied Physics Letters*, vol. 102, p. 233902, June 2013.

[38] K. G. Lee, X. W. Chen, H. Eghlidi, P. Kukura, R. Lettow, A. Renn, V. Sandoghdar, and S. Götzinger, "A planar dielectric antenna for directional single-photon emission and near-unity collection efficiency," *Nature Photonics*, vol. 5, pp. 166–169, Jan. 2011.

[39] W. Lukosz and R. E. Kunz, "Light emission by magnetic and electric dipoles close to a plane dielectric interface II radiation patterns of perpendicular oriented dipoles," *Journal of the Optical Society of America*, vol. 67, p. 1615, Dec. 1977.

[40] D. Toliopoulos, M. Khoury, M. Bouabdellaoui, N. Granchi, J.-B. Claude, A. Benali, I. Berbezier, D. Hannani, A. Ronda, J. Wenger, M. Bollani, M. Gurioli, S. Sanguinetti, F. Intonti, and M. Abbarchi, “Fabrication of spectrally sharp si-based dielectric resonators: combining etaloning with mie resonances,” *Optics Express*, vol. 28, p. 37734, Dec. 2020.

[41] M. Salvalaglio, M. Bouabdellaoui, M. Bollani, A. Benali, L. Favre, J.-B. Claude, J. Wenger, P. de Anna, F. Intonti, A. Voigt, and M. Abbarchi, “Hyperuniform monocrystalline structures by spinodal solid-state dewetting,” *Physical Review Letters*, vol. 125, p. 126101, Sept. 2020.

[42] J. A. Schuller, R. Zia, T. Taubner, and M. L. Brongersma, “Dielectric metamaterials based on electric and magnetic resonances of silicon carbide particles,” *Physical Review Letters*, vol. 99, p. 107401, Sept. 2007.

[43] Q. Zhao, L. Kang, B. Du, H. Zhao, Q. Xie, X. Huang, B. Li, J. Zhou, and L. Li, “Experimental demonstration of isotropic negative permeability in a three-dimensional dielectric composite,” *Physical Review Letters*, vol. 101, p. 027402, July 2008.

[44] L. Cao, P. Fan, E. S. Barnard, A. M. Brown, and M. L. Brongersma, “Tuning the color of silicon nanostructures,” *Nano Letters*, vol. 10, pp. 2649–2654, May 2010.

[45] G. Brönstrup, N. Jahr, C. Leiterer, A. Csáki, W. Fritzsche, and S. Christiansen, “Optical properties of individual silicon nanowires for photonic devices,” *ACS Nano*, vol. 4, pp. 7113–7122, Nov. 2010.

[46] K. Seo, M. Wober, P. Steinvurzel, E. Schonbrun, Y. Dan, T. Ellenbogen, and K. B. Crozier, “Multicolored vertical silicon nanowires,” *Nano Letters*, vol. 11, pp. 1851–1856, Mar. 2011.

[47] A. B. Evlyukhin, S. M. Novikov, U. Zywietz, R. L. Eriksen, C. Reinhardt, S. I. Bozhevolnyi, and B. N. Chichkov, “Demonstration of magnetic dipole resonances of dielectric nanospheres in the visible region,” *Nano Letters*, vol. 12, pp. 3749–3755, June 2012.

[48] S. H. Gage, “Modern dark-field microscopy and the history of its development,” *Transactions of the American Microscopical Society*, vol. 39, p. 95, Apr. 1920.

[49] T. Hinamoto, M. Hamada, H. Sugimoto, and M. Fujii, “Angle-, polarization-, and wavelength-resolved light scattering of single mie resonators using fourier-plane spectroscopy,” *Advanced Optical Materials*, vol. 9, p. 2002192, Feb. 2021.

[50] D. E. Gómez, K. C. Vernon, P. Mulvaney, and T. J. Davis, “Surface plasmon mediated strong exciton-photon coupling in semiconductor nanocrystals,” *Nano Letters*, vol. 10, pp. 274–278, Dec. 2009.

[51] T. G. Habteyes, I. Staude, K. E. Chong, J. Dominguez, M. Decker, A. Miroshnichenko, Y. Kivshar, and I. Brener, “Near-field mapping of optical modes on

all-dielectric silicon nanodisks,” *ACS Photonics*, vol. 1, pp. 794–798, Aug. 2014.

[52] T. Coenen, J. van de Groep, and A. Polman, “Resonant modes of single silicon nanocavities excited by electron irradiation,” *ACS Nano*, vol. 7, pp. 1689–1698, Jan. 2013.

[53] M. A. van de Haar, J. van de Groep, B. J. M. Brenny, and A. Polman, “Controlling magnetic and electric dipole modes in hollow silicon nanocylinders,” *Optics Express*, vol. 24, p. 2047, Jan. 2016.

[54] J. Feng, Q. Li, and S. Fan, “Compact and low cross-talk silicon-on-insulator crossing using periodic dielectric waveguide: erratum,” *Optics Letters*, vol. 36, p. 2308, June 2011.

[55] I. Staude, A. E. Miroshnichenko, M. Decker, N. T. Fofang, S. Liu, E. Gonzales, J. Dominguez, T. S. Luk, D. N. Neshev, I. Brener, and Y. Kivshar, “Tailoring directional scattering through magnetic and electric resonances in subwavelength silicon nanodisks,” *ACS Nano*, vol. 7, pp. 7824–7832, Aug. 2013.

[56] S. Checcucci, T. Bottein, M. Gurioli, L. Favre, D. Grosso, and M. Abbarchi, “Multifunctional metasurfaces based on direct nanoimprint of titania sol–gel coatings,” *Advanced Optical Materials*, vol. 7, p. 1801406, Mar. 2019.

[57] R. Fenollosa, F. Meseguer, and M. Tymczenko, “Silicon colloids: From microcavities to photonic sponges,” *Advanced Materials*, vol. 20, pp. 95–98, Jan. 2008.

[58] S. Checcucci, T. Bottein, J.-B. Claude, T. Wood, M. Putero, L. Favre, M. Gurioli, M. Abbarchi, and D. Grosso, “Titania-based spherical mie resonators elaborated by high-throughput aerosol spray: Single object investigation,” *Advanced Functional Materials*, vol. 28, p. 1801958, May 2018.

[59] J. Proust, F. Bedu, S. Chenot, I. Soumahoro, I. Ozerov, B. Gallas, R. Abdeddaim, and N. Bonod, “Chemical alkaline etching of silicon mie particles,” *Advanced Optical Materials*, vol. 3, pp. 1280–1286, May 2015.

[60] J. Ye and C. V. Thompson, “Templated solid-state dewetting to controllably produce complex patterns,” *Advanced Materials*, vol. 23, pp. 1567–1571, Feb. 2011.

[61] C. V. Thompson, “Solid-state dewetting of thin films,” *Annual Review of Materials Research*, vol. 42, pp. 399–434, Aug. 2012.

[62] E. J. Weidmann and J. C. Anderson, “Structure and growth of oriented tellurium thin films,” *Thin Solid Films*, vol. 7, pp. 265–276, Mar. 1971.

[63] P. P. Zhang, B. Yang, P. P. Rugheimer, M. M. Roberts, D. E. Savage, F. Liu, and M. G. Lagally, “Influence of germanium on thermal dewetting and agglomeration of the silicon template layer in thin silicon-on-insulator,” *Journal of Physics D: Applied Physics*, vol. 42, p. 175309, Aug. 2009.

[64] M. Bollani, M. Salvalaglio, A. Benali, M. Bouabdellaoui, M. Naffouti, M. Lodari, S. D. Corato, A. Fedorov, A. Voigt, I. Fraj, L. Favre, J. B. Claude, D. Grosso, G. Nicotra, A. Mio, A. Ronda, I. Berbezier, and M. Abbarchi, "Templated dewetting of single-crystal sub-millimeter-long nanowires and on-chip silicon circuits," *Nature Communications*, vol. 10, Dec. 2019.

[65] M. Naffouti, R. Backofen, M. Salvalaglio, T. Bottein, M. Lodari, A. Voigt, T. David, A. Benkouider, I. Fraj, L. Favre, A. Ronda, I. Berbezier, D. Grosso, M. Abbarchi, and M. Bollani, "Complex dewetting scenarios of ultrathin silicon films for large-scale nanoarchitectures," *Science Advances*, vol. 3, p. eaao1472, Nov. 2017.

[66] J. D. Joannopoulos, S. G. Johnson, J. N. Winn, and R. D. Meade, "Photonic crystals," Oct. 2011.

[67] P. W. Anderson, "Absence of diffusion in certain random lattices," *Physical Review*, vol. 109, pp. 1492–1505, Mar. 1958.

[68] D. S. Wiersma, P. Bartolini, A. Lagendijk, and R. Righini, "Localization of light in a disordered medium," *Nature*, vol. 390, pp. 671–673, Dec. 1997.

[69] A. Lagendijk, B. van Tiggelen, and D. S. Wiersma, "Fifty years of anderson localization," *Physics Today*, vol. 62, pp. 24–29, Aug. 2009.

[70] D. Balestri, M. Petruzzella, S. Checcucci, F. Intonti, N. Caselli, F. Sgrignuoli, F. W. M. Otten, A. Fiore, and M. Gurioli, "Mechanical and electric control of photonic modes in random dielectrics," *Advanced Materials*, vol. 31, p. 1807274, Feb. 2019.

[71] T. M. Truskett, S. Torquato, and P. G. Debenedetti, "Density fluctuations in many-body systems," *Physical Review E*, vol. 58, pp. 7369–7380, Dec. 1998.

[72] P. Kumar, "The theory of critical phenomena: An introduction to the renormalization group. by j. j. binney, n. j. dowrick, a. j. fisher, and m. e. j. newman, clarendon press, oxford, 1992. 464 pp.," *International Journal of Quantum Chemistry*, vol. 46, no. 5, pp. 671–671, 1993.

[73] A. Wax, C. Yang, V. Backman, K. Badizadegan, C. W. Boone, R. R. Dasari, and M. S. Feld, "Cellular organization and substructure measured using angle-resolved low-coherence interferometry," *Biophysical Journal*, vol. 82, pp. 2256–2264, Apr. 2002.

[74] F. C. Grozema, S. Tonzani, Y. A. Berlin, G. C. Schatz, L. D. A. Siebbeles, and M. A. Ratner, "Effect of structural dynamics on charge transfer in DNA hairpins," *Journal of the American Chemical Society*, vol. 130, pp. 5157–5166, Apr. 2008.

[75] L. Berthier, G. Biroli, J.-P. Bouchaud, W. Kob, K. Miyazaki, and D. R. Reichman, "Spontaneous and induced dynamic fluctuations in glass formers. i. general results and dependence on ensemble and dynamics," *The Journal of Chemical Physics*, vol. 126, p. 184503, May 2007.

[76] P. J. E. Peebles, “Principles of physical cosmology,” Sept. 2020.

[77] S. Torquato and F. H. Stillinger, “Local density fluctuations, hyperuniformity, and order metrics,” *Physical Review E*, vol. 68, p. 041113, Oct. 2003.

[78] S. Torquato, “Hyperuniform states of matter,” *Physics Reports*, vol. 745, pp. 1–95, June 2018.

[79] M. M. Milošević, W. Man, G. Nahal, P. J. Steinhardt, S. Torquato, P. M. Chaikin, T. Amoah, B. Yu, R. A. Mullen, and M. Florescu, “Hyperuniform disordered waveguides and devices for near infrared silicon photonics,” *Scientific Reports*, vol. 9, Dec. 2019.

[80] S. Torquato, G. Zhang, and F. Stillinger, “Ensemble theory for stealthy hyperuniform disordered ground states,” *Physical Review X*, vol. 5, p. 021020, May 2015.

[81] O. U. Uche, F. H. Stillinger, and S. Torquato, “Constraints on collective density variables: Two dimensions,” *Physical Review E*, vol. 70, p. 046122, Oct. 2004.

[82] P. Yeh and M. Hendry, “Optical waves in layered media,” *Physics Today*, vol. 43, pp. 77–78, Jan. 1990.

[83] S. John, “Strong localization of photons in certain disordered dielectric superlattices,” *Physical Review Letters*, vol. 58, pp. 2486–2489, June 1987.

[84] E. Yablonovitch, “Inhibited spontaneous emission in solid-state physics and electronics,” *Physical Review Letters*, vol. 58, pp. 2059–2062, May 1987.

[85] C. Jin, X. Meng, B. Cheng, Z. Li, and D. Zhang, “Photonic gap in amorphous photonic materials,” *Physical Review B*, vol. 63, p. 195107, Apr. 2001.

[86] E. Lidorikis, M. M. Sigalas, E. N. Economou, and C. M. Soukoulis, “Gap deformation and classical wave localization in disordered two-dimensional photonic-band-gap materials,” *Physical Review B*, vol. 61, pp. 13458–13464, May 2000.

[87] C. Rockstuhl, U. Peschel, and F. Lederer, “Correlation between single-cylinder properties and bandgap formation in photonic structures,” *Optics Letters*, vol. 31, p. 1741, June 2006.

[88] K. Edagawa, S. Kanoko, and M. Notomi, “Photonic amorphous diamond structure with a 3d photonic band gap,” *Physical Review Letters*, vol. 100, p. 013901, Jan. 2008.

[89] M. Florescu, S. Torquato, and P. J. Steinhardt, “Designer disordered materials with large, complete photonic band gaps,” *Proceedings of the National Academy of Sciences*, vol. 106, pp. 20658–20663, Nov. 2009.

[90] L. S. Froufe-Pérez, M. Engel, P. F. Damasceno, N. Muller, J. Haberko, S. C. Glotzer, and F. Scheffold, “Role of short-range order and hyperuniformity in the formation of band gaps in disordered photonic materials,” *Physical Review Letters*, vol. 117, p. 053902, July 2016.

[91] W. Man, M. Florescu, K. Matsuyama, P. Yadak, G. Nahal, S. Hashemizad, E. Williamson, P. Steinhardt, S. Torquato, and P. Chaikin, “Photonic band gap in isotropic hyperuniform disordered solids with low dielectric contrast,” *Optics Express*, vol. 21, p. 19972, Aug. 2013.

[92] N. Muller, J. Haberko, C. Marichy, and F. Scheffold, “Silicon hyperuniform disordered photonic materials with a pronounced gap in the shortwave infrared,” *Advanced Optical Materials*, vol. 2, pp. 115–119, Dec. 2013.

[93] G. Zito, G. Rusciano, G. Pesce, A. Malafronte, R. D. Girolamo, G. Ausanio, A. Vecchione, and A. Sasso, “Nanoscale engineering of two-dimensional disordered hyperuniform block-copolymer assemblies,” *Physical Review E*, vol. 92, p. 050601, Nov. 2015.

[94] P. M. Piechulla, L. Muehlenbein, R. B. Wehrspohn, S. Nanz, A. Abass, C. Rockstuhl, and A. Sprafke, “Fabrication of nearly-hyperuniform substrates by tailored disorder for photonic applications,” *Advanced Optical Materials*, vol. 6, p. 1701272, Feb. 2018.

[95] W. Zhou, Z. Cheng, B. Zhu, X. Sun, and H. K. Tsang, “Hyperuniform disordered network polarizers,” *IEEE Journal of Selected Topics in Quantum Electronics*, vol. 22, pp. 288–294, Nov. 2016.

[96] R. Degl’Innocenti, Y. D. Shah, L. Masini, A. Ronzani, A. Pitanti, Y. Ren, D. S. Jessop, A. Tredicucci, H. E. Beere, and D. A. Ritchie, “Hyperuniform disordered terahertz quantum cascade laser,” *Scientific Reports*, vol. 6, Jan. 2016.

[97] M. Castro-Lopez, M. Gaio, S. Sellers, G. Gkantzounis, M. Florescu, and R. Sapienza, “Reciprocal space engineering with hyperuniform gold disordered surfaces,” *APL Photonics*, vol. 2, p. 061302, June 2017.

[98] C. D. Rosa, F. Auriemma, C. Diletto, R. D. Girolamo, A. Malafronte, P. Morvillo, G. Zito, G. Rusciano, G. Pesce, and A. Sasso, “Toward hyperuniform disordered plasmonic nanostructures for reproducible surface-enhanced raman spectroscopy,” *Physical Chemistry Chemical Physics*, vol. 17, no. 12, pp. 8061–8069, 2015.

[99] O. Leseur, R. Pierrat, and R. Carminati, “High-density hyperuniform materials can be transparent,” *Optica*, vol. 3, p. 763, July 2016.

[100] T. Amoah and M. Florescu, “High-qoptical cavities in hyperuniform disordered materials,” *Physical Review B*, vol. 91, p. 020201, Jan. 2015.

[101] M. Florescu, P. J. Steinhardt, and S. Torquato, “Optical cavities and waveguides in hyperuniform disordered photonic solids,” *Physical Review B*, vol. 87, p. 165116, Apr. 2013.

[102] G. J. Aubry, L. S. Froufe-Pérez, U. Kuhl, O. Legrand, F. Scheffold, and F. Mortessagne, “Experimental tuning of transport regimes in hyperuniform disordered photonic materials,” *Physical Review Letters*, vol. 125, p. 127402, Sept. 2020.

[103] R. D. Batten, F. H. Stillinger, and S. Torquato, “Classical disordered ground states: Super-ideal gases and stealth and equi-luminous materials,” *Journal of Applied Physics*, vol. 104, p. 033504, Aug. 2008.

[104] O. Sigmund and K. Hougaard, “Geometric properties of optimal photonic crystals,” *Physical Review Letters*, vol. 100, p. 153904, Apr. 2008.

[105] S. Johnson and J. Joannopoulos, “Block-iterative frequency-domain methods for maxwell's equations in a planewave basis,” *Optics Express*, vol. 8, p. 173, Jan. 2001.

[106] D. Weaire and M. F. Thorpe, “Electronic properties of an amorphous solid. i. a simple tight-binding theory,” *Physical Review B*, vol. 4, pp. 2508–2520, Oct. 1971.

[107] E. H. Synge, “XXXVIII.a suggested method for extending microscopic resolution into the ultra-microscopic region,” *The London, Edinburgh, and Dublin Philosophical Magazine and Journal of Science*, vol. 6, pp. 356–362, Aug. 1928.

[108] H. A. Bethe, “Theory of diffraction by small holes,” *Physical Review*, vol. 66, pp. 163–182, Oct. 1944.

[109] G. Binnig, H. Rohrer, C. Gerber, and E. Weibel, “Surface studies by scanning tunneling microscopy,” *Physical Review Letters*, vol. 49, pp. 57–61, July 1982.

[110] D. W. Pohl, W. Denk, and M. Lanz, “Optical stethoscopy: Image recording with resolution $\lambda/20$,” *Applied Physics Letters*, vol. 44, pp. 651–653, Apr. 1984.

[111] A. Lewis, M. Isaacson, A. Harootunian, and A. Muray, “Development of a 500 Å spatial resolution light microscope,” vol. 13, pp. 227–231, Jan. 1984.

[112] A. Harootunian, E. Betzig, M. Isaacson, and A. Lewis, “Super-resolution fluorescence near-field scanning optical microscopy,” *Applied Physics Letters*, vol. 49, pp. 674–676, Sept. 1986.

[113] E. Betzig and J. K. Trautman, “Near-field optics: Microscopy, spectroscopy, and surface modification beyond the diffraction limit,” *Science*, vol. 257, pp. 189–195, July 1992.

[114] R. D. Grober, T. D. Harris, J. K. Trautman, E. Betzig, W. Wegscheider, L. Pfeiffer, and K. West, “Optical spectroscopy of a GaAs/AlGaAs quantum wire structure using near-field scanning optical microscopy,” *Applied Physics Letters*, vol. 64, pp. 1421–1423, Mar. 1994.

[115] E. Betzig and R. J. Chichester, “Single molecules observed by near-field scanning optical microscopy,” *Science*, vol. 262, pp. 1422–1425, Nov. 1993.

[116] R. Stöckle, C. Fokas, V. Deckert, R. Zenobi, B. Sick, B. Hecht, and U. P. Wild, “High-quality near-field optical probes by tube etching,” *Applied Physics Letters*, vol. 75, pp. 160–162, July 1999.

[117] B. Hecht, B. Sick, U. P. Wild, V. Deckert, R. Zenobi, O. J. F. Martin, and D. W. Pohl, "Scanning near-field optical microscopy with aperture probes: Fundamentals and applications," *The Journal of Chemical Physics*, vol. 112, pp. 7761–7774, May 2000.

[118] J. A. Veerman, A. M. Otter, L. Kuipers, and N. F. van Hulst, "High definition aperture probes for near-field optical microscopy fabricated by focused ion beam milling," *Applied Physics Letters*, vol. 72, pp. 3115–3117, June 1998.

[119] T. Saiki, S. Mononobe, M. Ohtsu, N. Saito, and J. Kusano, "Tailoring a high-transmission fiber probe for photon scanning tunneling microscope," *Applied Physics Letters*, vol. 68, pp. 2612–2614, May 1996.

[120] Y. C. Martin, H. F. Hamann, and H. K. Wickramasinghe, "Strength of the electric field in apertureless near-field optical microscopy," *Journal of Applied Physics*, vol. 89, pp. 5774–5778, May 2001.

[121] S. Kühn, U. Håkanson, L. Rogobete, and V. Sandoghdar, "Enhancement of single-molecule fluorescence using a gold nanoparticle as an optical nanoantenna," *Physical Review Letters*, vol. 97, p. 017402, July 2006.

[122] J. N. Farahani, D. W. Pohl, H.-J. Eisler, and B. Hecht, "Single quantum dot coupled to a scanning optical antenna: A tunable superemitter," *Physical Review Letters*, vol. 95, p. 017402, June 2005.

[123] P. J. Schuck, D. P. Fromm, A. Sundaramurthy, G. S. Kino, and W. E. Moerner, "Improving the mismatch between light and nanoscale objects with gold bowtie nanoantennas," *Physical Review Letters*, vol. 94, p. 017402, Jan. 2005.

[124] N. Caselli, F. L. China, W. Bao, F. Riboli, A. Gerardino, L. Li, E. H. Linfield, F. Pagliano, A. Fiore, P. J. Schuck, S. Cabrini, A. Weber-Bargioni, M. Gurioli, and F. Intonti, "Deep-subwavelength imaging of both electric and magnetic localized optical fields by plasmonic campanile nanoantenna," *Scientific Reports*, vol. 5, June 2015.

[125] P. Lambelet, A. Sayah, M. Pfeffer, C. Philipona, and F. Marquis-Weible, "Chemically etched fiber tips for near-field optical microscopy: a process for smoother tips," *Applied Optics*, vol. 37, p. 7289, Nov. 1998.

[126] G. A. Valaskovic, M. Holton, and G. H. Morrison, "Parameter control, characterization, and optimization in the fabrication of optical fiber near-field probes," *Applied Optics*, vol. 34, p. 1215, Mar. 1995.

[127] G. Y. Shang, C. Wang, J. Wu, C. L. Bai, and F. H. Lei, "Shear force scanning near-field optical microscope based on a piezoelectric bimorph cantilever," *Review of Scientific Instruments*, vol. 72, pp. 2344–2349, May 2001.

[128] R. Zsigmondy, "Ueber wässrige lösungen metallischen goldes," *Justus Liebig's Annalen der Chemie*, vol. 301, no. 1, pp. 29–54, 1898.

[129] K. Yee, “Numerical solution of initial boundary value problems involving maxwell's equations in isotropic media,” *IEEE Transactions on Antennas and Propagation*, vol. 14, pp. 302–307, May 1966.

[130] A. C. Polycarpou, “Introduction to the finite element method in electromagnetics,” *Synthesis Lectures on Computational Electromagnetics*, vol. 1, pp. 1–126, Jan. 2006.

[131] W. Yan, R. Faggiani, and P. Lalanne, “Rigorous modal analysis of plasmonic nanoresonators,” *Physical Review B*, vol. 97, p. 205422, May 2018.

[132] T. Wu, M. Gurioli, and P. Lalanne, “Nanoscale light confinement: the q’s and v’s,” *ACS Photonics*, vol. 8, pp. 1522–1538, May 2021.

[133] J.-P. Berenger, “A perfectly matched layer for the absorption of electromagnetic waves,” *Journal of Computational Physics*, vol. 114, pp. 185–200, Oct. 1994.

[134] D. Balestri, *Nano-optics in random and non-Hermitian photonic systems.* PhD thesis, Univeristy of Florence, 2020.

[135] I. M. Hancu, A. G. Curto, M. Castro-López, M. Kuttge, and N. F. van Hulst, “Multipolar interference for directed light emission,” *Nano Letters*, vol. 14, pp. 166–171, Dec. 2013.

[136] N. Dotti, F. Sarti, S. Bietti, A. Azarov, A. Kuznetsov, F. Biccari, A. Vinattieri, S. Sanguinetti, M. Abbarchi, and M. Gurioli, “Germanium-based quantum emitters towards a time-reordering entanglement scheme with degenerate exciton and biexciton states,” *Physical Review B*, vol. 91, p. 205316, May 2015.

[137] A. Capretti, A. Lesage, and T. Gregorkiewicz, “Integrating quantum dots and dielectric mie resonators: A hierarchical metamaterial inheriting the best of both,” *ACS Photonics*, vol. 4, pp. 2187–2196, Aug. 2017.

[138] A. Tognazzi, K. I. Okhlopkov, A. Zilli, D. Rocco, L. Fagiani, E. Mafakheri, M. Bollani, M. Finazzi, M. Celebrano, M. R. Shcherbakov, A. A. Fedyanin, and C. D. Angelis, “Third-harmonic light polarization control in magnetically resonant silicon metasurfaces,” *Optics Express*, vol. 29, p. 11605, Mar. 2021.

[139] H. Alhalaby, H. Zaraket, and M. Principe, “Enhanced photoluminescence with dielectric nanostructures: A review,” *Results in Optics*, vol. 3, p. 100073, May 2021.

[140] F. Todisco, R. Malureanu, C. Wolff, P. A. D. Gonçalves, A. S. Roberts, N. A. Mortensen, and C. Tserkezis, “Magnetic and electric mie-exciton polaritons in silicon nanodisks,” *Nanophotonics*, vol. 9, pp. 803–814, Mar. 2020.

[141] F. Hao and P. Nordlander, “Efficient dielectric function for FDTD simulation of the optical properties of silver and gold nanoparticles,” *Chemical Physics Letters*, vol. 446, pp. 115–118, Sept. 2007.

[142] A. E. Miroshnichenko, A. B. Evlyukhin, Y. F. Yu, R. M. Bakker, A. Chipouline, A. I. Kuznetsov, B. Luk'yanchuk, B. N. Chichkov, and Y. S. Kivshar, "Nonradiating anapole modes in dielectric nanoparticles," *Nature Communications*, vol. 6, Aug. 2015.

[143] R. M. Bakker, D. Permyakov, Y. F. Yu, D. Markovich, R. Paniagua-Domínguez, L. Gonzaga, A. Samusev, Y. Kivshar, B. Luk'yanchuk, and A. I. Kuznetsov, "Magnetic and electric hotspots with silicon nanodimers," *Nano Letters*, vol. 15, pp. 2137–2142, Feb. 2015.

[144] E. D. Palik, "Handbook of optical constants of solids," 1985.

[145] N. A. Butakov and J. A. Schuller, "Designing multipolar resonances in dielectric metamaterials," *Scientific Reports*, vol. 6, Dec. 2016.

[146] J. Berzinš, S. Indrišiūnas, K. van Erve, A. Nagarajan, S. Fasold, M. Steinert, G. Gerini, P. Gečys, T. Pertsch, S. M. B. Bäumer, and F. Setzpfandt, "Direct and high-throughput fabrication of mie-resonant metasurfaces via single-pulse laser interference," *ACS Nano*, vol. 14, pp. 6138–6149, Apr. 2020.

[147] F. Leroy, Y. Saito, S. Curiotto, F. Cheynis, O. Pierre-Louis, and P. Müller, "Shape transition in nano-pits after solid-phase etching of SiO2 by si islands," *Applied Physics Letters*, vol. 106, p. 191601, May 2015.

[148] W. H. Koo, S. M. Jeong, F. Araoka, K. Ishikawa, S. Nishimura, T. Toyooka, and H. Takezoe, "Light extraction from organic light-emitting diodes enhanced by spontaneously formed buckles," *Nature Photonics*, vol. 4, pp. 222–226, Feb. 2010.

[149] M. Burresi, F. Pratesi, K. Vynck, M. Prasciolu, M. Tormen, and D. S. Wiersma, "Two-dimensional disorder for broadband, omnidirectional and polarization-insensitive absorption," *Optics Express*, vol. 21, p. A268, Feb. 2013.

[150] S. Yu, C.-W. Qiu, Y. Chong, S. Torquato, and N. Park, "Engineered disorder in photonics," *Nature Reviews Materials*, vol. 6, pp. 226–243, Dec. 2020.

[151] K. Vynck, R. Pierrat, R. Carminati, L. S. Froufe-Pérez, F. Scheffold, R. Sapienza, S. Vignolini, and J. J. Sáenz, "Light in correlated disordered media," 2021.

[152] D. S. Wiersma, "Disordered photonics," *Nature Photonics*, vol. 7, pp. 188–196, Feb. 2013.

[153] M. Florescu, S. Torquato, and P. J. Steinhardt, "Effects of random link removal on the photonic band gaps of honeycomb networks," *Applied Physics Letters*, vol. 97, p. 201103, Nov. 2010.

[154] L. Midolo and A. Fiore, "Design and optical properties of electromechanical double-membrane photonic crystal cavities," *IEEE Journal of Quantum Electronics*, vol. 50, pp. 404–414, June 2014.

[155] M. Petruzzella, F. M. Pagliano, Ž. Zobenica, S. Birindelli, M. Cotrufo, F. W. M. van Otten, R. W. van der Heijden, and A. Fiore, "Electrically driven quantum light emission in electromechanically tuneable photonic crystal cavities," *Applied Physics Letters*, vol. 111, p. 251101, Dec. 2017.

[156] Ž. Zobenica, R. W. van der Heijden, M. Petruzzella, F. Pagliano, R. Leijssen, T. Xia, L. Midolo, M. Cotrufo, Y. Cho, F. W. M. van Otten, E. Verhagen, and A. Fiore, "Integrated nano-opto-electro-mechanical sensor for spectrometry and nanometrology," *Nature Communications*, vol. 8, Dec. 2017.

[157] M. Petruzzella, F. L. China, F. Intonti, N. Caselli, M. D. Pas, F. W. M. van Otten, M. Gurioli, and A. Fiore, "Nanoscale mechanical actuation and near-field read-out of photonic crystal molecules," *Physical Review B*, vol. 94, p. 115413, Sept. 2016.

[158] N. Granchi, M. Petruzzella, D. Balestri, A. Fiore, M. Gurioli, and F. Intonti, "Multimode photonic molecules for advanced force sensing," *Optics Express*, vol. 27, p. 37579, Dec. 2019.

[159] B. Daudin, F. Widmann, G. Feuillet, Y. Samson, M. Arlery, and J. L. Rouvière, "Stranski-krastanov growth mode during the molecular beam epitaxy of highly strained GaN," *Physical Review B*, vol. 56, pp. R7069–R7072, Sept. 1997.

[160] F. Intonti, S. Vignolini, F. Riboli, A. Vinattieri, D. S. Wiersma, M. Colocci, L. Balet, C. Monat, C. Zinoni, L. H. Li, R. Houdré, M. Francardi, A. Gerardino, A. Fiore, and M. Gurioli, "Spectral tuning and near-field imaging of photonic crystal microcavities," *Physical Review B*, vol. 78, p. 041401, July 2008.

[161] J. Dong and D. A. Drabold, "Atomistic structure of band-tail states in amorphous silicon," *Physical Review Letters*, vol. 80, pp. 1928–1931, Mar. 1998.

[162] S. Imagawa, K. Edagawa, K. Morita, T. Niino, Y. Kagawa, and M. Notomi, "Photonic band-gap formation, light diffusion, and localization in photonic amorphous diamond structures," *Physical Review B*, vol. 82, p. 115116, Sept. 2010.

[163] T. Yuan, T. Feng, and Y. Xu, "Manipulation of transmission by engineered disorder in one-dimensional photonic crystals," *Optics Express*, vol. 27, p. 6483, Feb. 2019.

[164] L. S. Froufe-Pérez, M. Engel, J. J. Sáenz, and F. Scheffold, "Band gap formation and anderson localization in disordered photonic materials with structural correlations," *Proceedings of the National Academy of Sciences*, vol. 114, pp. 9570–9574, Aug. 2017.

[165] P. Lalanne, W. Yan, K. Vynck, C. Sauvan, and J.-P. Hugonin, "Light interaction with photonic and plasmonic resonances," *Laser & Photonics Reviews*, vol. 12, p. 1700113, Apr. 2018.

[166] S. Haroche and D. Kleppner, “Cavity quantum electrodynamics,” vol. 42, pp. 24–30, Jan. 1989.

[167] S. Noda, M. Fujita, and T. Asano, “Spontaneous-emission control by photonic crystals and nanocavities,” vol. 1, pp. 449–458, Aug. 2007.

[168] N. Louvion, D. Gérard, J. Mouette, F. de Fornel, C. Seassal, X. Letartre, A. Rahmani, and S. Callard, “Local observation and spectroscopy of optical modes in an active photonic-crystal microcavity,” vol. 94, p. 113907, Mar. 2005.

[169] P. Kramper, M. Kafesaki, C. M. Soukoulis, A. Birner, F. Müller, U. Gösele, R. B. Wehrspohn, J. Mlynek, and V. Sandoghdar, “Near-field visualization of light confinement in a photonic crystal microresonator,” vol. 29, p. 174, Jan. 2004.

[170] A. F. Koenderink, M. Kafesaki, B. C. Buchler, and V. Sandoghdar, “Controlling the resonance of a photonic crystal microcavity by a near-field probe,” vol. 95, p. 153904, Oct. 2005.

[171] E. Tiguntseva, A. Chebykin, A. Ishteev, R. Haroldson, B. Balachandran, E. Ushakova, F. Komissarenko, H. Wang, V. Milichko, A. Tsypkin, D. Zuev, W. Hu, S. Makarov, and A. Zakhidov, “Resonant silicon nanoparticles for enhancement of light absorption and photoluminescence from hybrid perovskite films and metasurfaces,” vol. 9, no. 34, pp. 12486–12493, 2017.

[172] S. V. Makarov, V. Milichko, E. V. Ushakova, M. Omelyanovich, A. C. Pasaran, R. Haroldson, B. Balachandran, H. Wang, W. Hu, Y. S. Kivshar, and A. A. Zakhidov, “Multifold emission enhancement in nanoimprinted hybrid perovskite metasurfaces,” vol. 4, pp. 728–735, Mar. 2017.

[173] E. Y. Tiguntseva, G. P. Zograf, F. E. Komissarenko, D. A. Zuev, A. A. Zakhidov, S. V. Makarov, and Y. S. Kivshar, “Light-emitting halide perovskite nanoantennas,” vol. 18, pp. 1185–1190, Jan. 2018.

[174] E. Y. Tiguntseva, D. G. Baranov, A. P. Pushkarev, B. Munkhbat, F. Komissarenko, M. Franckevičius, A. A. Zakhidov, T. Shegai, Y. S. Kivshar, and S. V. Makarov, “Tunable hybrid fano resonances in halide perovskite nanoparticles,” vol. 18, pp. 5522–5529, aug 2018.